NATIONAL INSTITUTE OF LASER ENHANCED SCIENCES
CAIRO UNIVERSITY

JOURNAL OF LASER SCIENCE AND APPLICATIONS (JLSA)

ISSN: 1687-8892 VOLUME 2 ISSUE 1

National Institute of Laser Enhanced Sciences, JLSA's Vol.02. Issue.1 (2025)
DOI: 10.21608/jlsa.2025.345137.1025

NILES

Journal of Laser Science and Applications
journal homepage: https://jlsa.journals.ekb.eg

Cairo University

Efficacy of 810 nm Diode Low-Level Laser Treatment on Healing Periodontal Intra-Bony Defects: A Blinded Animal Investigation

Shrief Hemaid*, Hossam Eldeen F. Bayoumy

Medical applications, National Institute of laser enhanced sciences, Cairo University, Giza, Egypt

Abstract

Background: Low-power laser treatment demonstrated a bio-stimulatory positive impact during the initial phases of osseous regeneration.
Purpose: The study's primary objective is to assess the histological impact of low-power laser therapy (810 nm) on healing intentionally generated intra-bony periodontal defects.
Methods: The investigation was evaluated by carrying out 16 identified defects involving eight adult male rabbits (totaling 8 individuals) utilized in this study; categorized into 2 groups using the split-mouth technique. The control group defects were not subjected to any treatment modality, whereas the test group ones were subjected to laser irradiation. Four animals (8 defects) were euthanized after 15 days, and the other four (8 defects) at 30 days post-surgery, followed by histological analyses. Defects were bilaterally produced in each animal, manifesting as bony cavities of 10 mm in occluso-apical length and 4 mm in bucco-lingual length between the first and second molars, utilizing a tapered drill (of fissure type) attached to a high-rpm motor. Following the randomized group allocation, the right-side defects were designated the control group, while the left ones were subjected to laser irradiation.
Results: Irradiated defects exhibited diminished inflammatory response, advanced periodontal fiber regeneration and conjunction, and developed bone growth after 15 and 30 days compared to the untreated control group.
Conclusions: Low-power laser therapy diminishes the inflammatory response, enhances periodontal fiber regeneration and alignment, and promotes bone maturation and healing.
Keywords— low power laser therapy, bio-stimulation, periodontal intra-bony defects, periodontal regeneration, rabbits, histological study

I. Introduction

Dysbiotic plaque biofilms are associated with chronic periodontitis, a multifactorial inflammatory disorder characterised by a progressive deterioration of tooth-supporting tissues. [1] Specific pathogenic microorganisms induce progressive degradation of the alveolar bone, periodontal ligament (PDL), or clinical attachment loss (CAL), triggering recession, pocket formation, or both [2, 3]. Periodontal disease is a multifaceted condition marked by root cementum exposure, bone resorption, and degeneration of periodontal tissue resulting from detached connective tissue fibers from the tooth [4]. Periodontal therapy aims to eradicate the inflammatory process, microbiological causes, and risk factors that may exacerbate disease progression and restore damaged periodontal structures.

Periodontal regeneration is considered a complicated, multifactorial process that entails a coordinated scenario of cell activities, including adhesion, migration, proliferation, and differentiation [5]. Periodontal regenerative techniques such as root bio-modifications, bone substitutes, soft tissue grafts, guided regeneration of tissues (GTR), biomaterials, and physical methods like Low-Power laser therapy (LPLT) or even their combinations are essential for restoring periodontal health and enhancing tooth longevity. These innovative approaches not only promote healing but also improve the overall aesthetics and function of the periodontal structure [6-13].

At present, regenerative periodontal therapies may restore just a part of the diseased tissue, but their capacity for complete periodontal restoration is constrained [14].

Multiple approaches were assessed, yet no singular methodology has been acknowledged as the gold standard for restoring intra-bony defects (IBDs). Periodontal therapy

Corresponding author: Sherif Hemaid Email: shreifhemaid1@pg.cu.edu.eg
Received: December 19, 2024 Revised: January 26, 2025 Accepted: January 28, 2025

ISSN: 1687-8892

aims to achieve two primary objectives: 1) to avert the onset of different types of periodontal diseases by mitigation of inflammation and infection, and 2) to maintain or enhance the aesthetics, comfort, functionality, and health of the supporting structures, including the gingival tissues, periodontal ligaments, cementum, and alveolar bone [10].

After Maiman invented the first practical laser system in 1960, two varieties of lasers were used in dentistry and later in periodontology: high-power lasers (HPL) and low-power lasers (LPL). Following Maiman's invention of the first practical laser system in 1960, two categories of lasers were initially employed in dentistry and subsequently in periodontology: high-level lasers (HLL), which are used for surgical procedures, and Low-Power lasers (LPL), which are used for bio-stimulation and tissue repair [15-17]. Due to its ability to enhance collagen synthesis, cellular proliferation, and localized vascular circulation, LPL has lately been used as a bio-stimulant for tissue rehabilitation [11-13]. HLL markedly enhanced biochemical, bioelectric, and bio-energetic functions at the cellular level, leading to elevated metabolism, increased mitotic division of epithelium, proliferation and maturation of fibroblasts, collagen synthesis, augmented granulation tissue, reduced inflammatory mediators, and stimulation of local microcirculation to facilitate healing [16-18].

Particular studies on novel bone formation suggest that the bio-stimulatory effects of lasers arise from a combination of their distinctive characteristics and the creation of specific local circumstances that enhance new osseous tissue development and resolve edema [6, 19].

Before conducting the study, the hypotheses of this work should be clearly defined; 1) Null hypothesis: The treated defects will exhibit no inflammatory changes compared to the non-treated defects after 15 days post-surgery, and after 30 days, there will be no regeneration of periodontal fibers or bone fill relative to the non-treated defects, or 2) Alternative hypothesis: The treated defects will exhibit low inflammation relative to the non-treated defects after 15 days post-surgery, and after 30 days, periodontal fibers and bone fill will regenerate in comparison to the non-treated defects.

This investigation is intended to histologically assess the impact of low-power laser therapy LPLT (810 nm) on the repair of intentionally generated bio-stimulatory periodontal defects.

II. Materials and Instruments

Given the scarcity of histological studies on IBD healing, especially in rabbits, and the predominance of research focused on bone defects in the femur or calvaria, it is crucial to recognize that the methodology employed in this study, which can be adapted for various experimental contexts, could potentially contribute significantly to a more comprehensive understanding of periodontal healing, thereby enlightening the field of periodontology.

Preparation of animals:

Upon receiving authorization from the Experimental Animal Research Ethics Committee (Cu/I/F/1/19), eight mature New Zealand male white rabbits, aged 7-8 months and averaging over 2.5 kg, were utilized in this investigation to examine sixteen intra-bony defects. Before the procedures, each rabbit was isolated to acclimate to the laboratory environment. They received a distinctive pelleted commercial feed. To ensure the animals' comfort and safety, each rabbit was carefully prepared and received a distinctive pelleted commercial feed. To attain sedation and general profound anesthesia, subcutaneous injections of Ketamine Hydrochloride (50mg/kg) and Xylazine Hydrochloride (20mg/kg) were administered.

-Experimental groups and induction of periodontal defects

Sixteen periodontal defects were generated in the region of interest (ROI), with eight in each group and two in the same rabbit, one on each side. The control group (C group): Rabbits received no materials and laser therapy was not administered for defect treatment. Test laser group (TL group): All defects were utterly exposed to laser radiation. Defects in the control group were allocated to the right side of the rabbits, whereas those in the test group were allocated to the left side. Rabbits were assigned to groups at random.

Following the thorough shaving of the surgical area, 70% ethanol was employed for disinfection in anticipation of the surgical procedure. And after LA(Artinibsa 40 mg/ 0.01 mg / mL with Epinephrine 1:100,000) was injected at the ROI for hemostasis, a five-centimeter rostrocaudal full-thickness incision was performed through the skin, encompassing the underlying muscles, to reveal the Region of Interest (ROI), the interdental space between the rabbit's first and second mandibular molars.

After retraction of the flap corona-apically, one osseous-wall cavity was established by revealing the distal and mesial surfaces of the respective roots of the first and second molars using a stopper marked-premeasured tapered FG cutting bur attached to a high-rpm motor with copious physiological NaCl irrigation [20, 21]. The cavity was measured at 4 mm in depth (bucco-lingual path) from the buccal end of the alveolus to the lingual surface of the bony cavity and 10 mm in the corona-apical direction from the CEJ to the most apical base of the defect. The exposed roots were thoroughly cleaned using a Gracey curette G5/6 to eradicate the Sharpey's fibers from the cementum surface **(Fig.1)**.

Figure 1. Defect induction

Per blinding regulations, a custom-built laser apparatus was utilized (A custom-made laser device, (calibrated with the Melles Griot power meter Model (30 W Broadband)) was used.). It was engineered to incorporate both placebo and active modes. In the placebo mode, only the red LED indication light was activated, devoid of laser radiation. A diode [GaAlAs] 810 nm laser was utilized in continuous mode at a power of 100 mW for 180 seconds, delivering 18 J through a tip with a radius of 0.35 cm and an area of 0.385 cm^2 before flap closure. The energy density applied is approximately 46.8 J/cm^2.

For suturing, flap repositioned was assured using a basic interrupted technique, using 3-0 silk for the skin and 3-0 vicryl for the muscles. The wound was left uncovered and exposed to the air. Post-surgery, a laser was administered extra-orally and repeated daily for five consecutive days, adhering to the blinding protocols.

-Postoperative management

Thereafter, each rabbit was confined to an individual cage. The environment was regulated on a 12-hour light-dark cycle with a relative humidity of 22%. Water and nutrition were accessible. Diclofenac sodium, an analgesic for postoperative care, was provided daily for three days at a dosage of 10 mg/kg. Ceftriaxone (25 mg/kg) was provided once daily for three consecutive days post-surgery. Over a span of five consecutive days, the laser device was applied to each rabbit twice negatively on the right side and twice positively on the left side, with each application lasting 90 seconds. The device was set to laser active mode on the left and non-laser placebo mode on the right **(**Error! Reference source not found.**)**.

Figure 2. Laser bio-stimulation

-Histologic preparation

Thin histological sections, precisely 5 micrometers in thickness, were carefully prepared in a mesiodistal orientation. These sections were then stained with hematoxylin and eosin (H & E), a method commonly used to highlight the cellular structures [22], allowing for detailed examination under an optical microscope (Olympus xc30. Tokyo. Japan).

-Evaluation of the histologic sections

The structure of the periodontal ligament (PDL) was categorized according to Behfarnia et al. [23] as **score 0:** disorganized PDL with irregular fiber orientation, **score 1:** organized PDL, which was characterized by dense connective tissue and **score 2:** fibers are oriented regularly from the alveolar bone towards the surface of the cementum. Also, The inflammatory response was evaluated using an optical microscope and scored based on the presence of inflammatory cells [23] into: **score 0:** < 10% inflammatory cells, **score 1:** 10-30% inflammatory cells, **score 2:** 30-50% inflammatory cells and **score 3:** > 50% inflammatory cells. In addition, Regenerated Bone was graded according to Lucaciu (2015) [24] as **score 0:** absent, **score 1:** present at the borders of the defect and **score 2:** present deep in the defect.

-Randomization and Blinding procedures

Initially, each of the eight animals was randomly assigned to either a 15-day or a 30-day sacrifice period. Subsequently, the side was identified as right or left. The site was subsequently chosen randomly as a control or test group. The periodontist researcher conducted all surgical procedures with a double-anonymized methodology. Initially, a different dentist operated the laser equipment in blind mode after the primary operator (the researcher) set it to active or non-laser placebo mode. Secondly, the technician performing the histological preparation and the histologist evaluating it were ignorant of the defect's group classification.

III. Results

-After 15 days

In control group (C), tissue specimens on day 15 exhibited numerous inflammatory chronic cells, predominantly macrophages and lymphocytes (30-50% inflammatory cells); thus, they were classified as Score 2 **(Figure)**. Tissue faults were evident in the periodontal ligament (PDL) and the bordering bone. A score of 0 was assigned in the absence of PDL regeneration, connective tissue adhesion, or organized fiber orientation. The acellular type of cementum was entirely excised from the root. Regarding bone, none has been regenerated, which deserved a grade 0 **(Fig. 3)**. Scorings are presented in Error! Reference source not found..

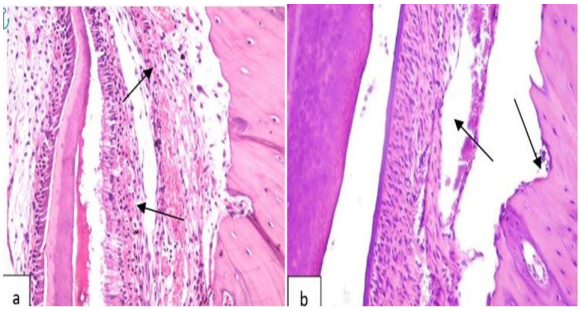

Figure 3. (C) Untreated defect on the 15th day
Photomicrograph of intra-bony defect showing **arrow (a):** chronic inflammatory cells mainly lymphocytes and macrophages and **arrow (b):** tissues defect in both periodontal ligament PDL and adhesive bone **(H & E) (200X).**

In the test laser group (TL), tissue specimens exhibited a minor inflammatory response characterized by infiltrations of a limited number of mononuclear cells (10-30% inflammatory cells), receiving a score of 1 **(Fig. 4)**. The PDL zone exhibited structured fiber bundles oriented perpendicularly to the root surface. Nonetheless, fibers adjacent to the bone surface exhibited a haphazard organization, which was indicated by the score 1. Remodeling of old bone's surface was observed in bone resorption regions. No sign of new bone growth was observed. The bone received a rating of 0 **(Fig. 4)**.

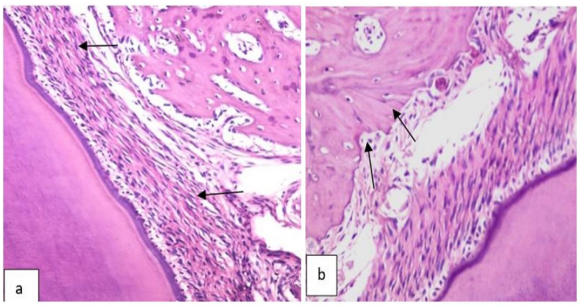

Figure 4. (TL) Defects treated by Laser on the 15th day Photomicrograph of intra-bony defect showing **arrow (a):** mild inflammatory reaction appeared as few mononuclear cells infiltration and connective tissue adhesion with perpendicular fiber orientation supracrestal and **arrow** (**b):** resorption of old bone **(H & E) (200X).**

-After 30 days

In the control Group (C), the specimens exhibited minimal inflammatory chronic cell infiltrates, predominantly macrophages and lymphocytes (10-30% inflammatory cells), designated as score 1 **(Fig. 5)**. Organized PDL collagen fibers were observed, confined to the apex region, accompanied by connective tissue adhesion exhibiting perpendicular orientation of fibers. Consequently, the score is 1. The acellular cementum was inadequately established on the root surface. Osseous tissue regeneration was observed at the defect's boundary, marked by the significance of osteoblastic cell proliferation and a distinct demarcation between the old and new bone. Consequently, it was evaluated as 1 **(Figure)**.

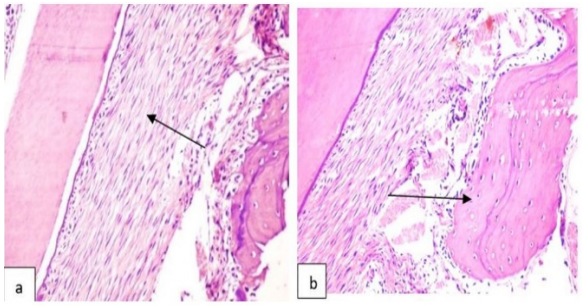

Figure 5. (C) Untreated defect on the 30th day. Photomicrograph of intra-bony defect showing **arrow** (a) few chronic inflammatory cells infiltration and PDL regeneration limited to the apical part of the defect **arrow** (b) regeneration of bony tissues at the surface of the defect **(H & E) (200X)**.

In the test laser group (TL), specimens had a moderate inflammatory response, with fewer than 10% of inflammatory cells in the therapy, receiving a score of zero. The regeneration of the periodontal ligament was confined to the apex, exhibiting a perpendicular orientation of the fibers. Furthermore, the periodontal ligament was more structured and integrated into the newly developed bone. Consequently, a specific score 1 **(Fig. 6)**.

New bone development was observed on the defect's surface, characterized by osteoblast proliferation. This received a grade of 1.

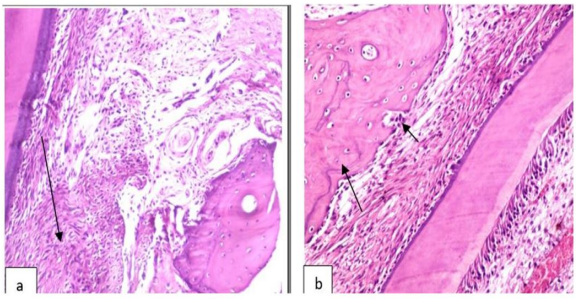

Figure 6. (T) Defects treated by Laser on the 30th day Photomicrograph of intra-bony defect showing **arrow (a):** mild inflammatory response and PDL regeneration limited to the apical part of the defect and **arrow (b):** new bone formation seen at the surface of the defect which characterized by osteoblasts proliferation **(H & E) (200X).**

Table 1. A detailed comparison of the histological scores in the study groups on the 15th and 30th days highlights significant insights crucial for understanding the progression of the condition under investigation

Scoring parameter	(C) group		(T) group	
Inflammatory cells	2	1	1	0
Periodontal ligament	0	1	1	1
Bone	0	1	0	1

III. Discussion

A range of potential limitations must be recognized before conclusions are drawn. The lack of prior analogous studies addressing periodontal intra-bony defects in rabbits constituted restricting factors. While the methodology employed in this study is applicable across various contexts, the results pertain solely to experimental animal research and may lack generalizability. The investigation encompassed sixteen defects, and the study has established consistent and coherent results, reinforcing its external validity.

Although the precise mechanisms underlying the stimulation of bone repair remain poorly understood, they are likely multifaceted. They may involve collagen formation, angiogenesis, osteoblast proliferation and differentiation, and ATP synthesis via mitochondrial respiration [11-13].

Furthermore, LPLT may enhance blood circulation at the application site, augmenting the delivery of circulating cells, nutrients, oxygen, and inorganic salts to the bone defect. The primary factors affecting bone defect repair are the ability of osteogenic precursor cells to invade the defect and differentiate into osteoblasts and their presence in the

adjacent soft tissue or bone. Furthermore, fibroblast cells capable of secreting collagen and vital for forming periodontal ligament can be induced to proliferate by LPLT.

Results of this investigation demonstrate that laser irradiation has the potential to significantly improve bone repair independently. The current study showed a reduction in the inflammatory response after LPLT compared to the control group at 15 and 30 days relative to baseline. Also, this study showed improved bone healing with LPLT compared to the control group, with differences in healing observed at 15 and 30 days from baseline. This is concurrent with Ghahroudi et al., who concluded that LPLT may facilitate bone growth in skeletal abnormalities [25].

The current study's results indicated enhancements in periodontal fiber orientation and regeneration following LPLT, as opposed to the control group, after 15 and 30 days relative to baseline measurements. Pereira et al. demonstrated that non-surgical periodontal treatment and photo-biomodulation rehabilitation in experimental periodontitis in rats effectively repaired the periodontal ligament, reduced bone loss, and modulated inflammatory processes [26]. This was consistent with our findings. The results aligned also with Gerbi's conclusions, indicating that laser treatment exerts a synergistic bio-modulating impact on the healing process of a defect, whether accompanied or not by the application of organic lyophilized bone and bovine lyophilized membrane on the rat femur [27, 28]. Similarly, the findings align with Huang's study, demonstrating that LPLT alone enhanced mitochondrial activity, RNA / DNA synthesis in osteoblasts, cell survival, and alkaline phosphatase levels [19]. Furthermore, these findings are consistent with Aboelsaad's work, which demonstrated that LPLT exerted a beneficial local bio-stimulatory impact during the initial phases of bone repair [29, 30]. Moreover, in consistence with our findings, Lopes et al. observed significantly enhanced bone repair in laser-irradiated lesions in rabbit tibiae [31].

-Limitations

To our knowledge, no prior studies have been conducted on IBD in rabbits or rats. The typical healing capability of bone in rabbits is approximately two weeks, which is regarded as quick; thus, comparing routine healing with Low-Power laser bio-stimulated healing of intra-bony lesions proved hard. The histologic assessment in this study was qualitative and did not include statistical analysis, which may represent a limitation.

IV. Conclusion

Low-power laser therapy may promote the healing of osseous tissues, diminish the inflammatory response, and improve periodontal fiber orientation and tissue regeneration in periodontal bone defect healing. LPLT is considered a non-invasive and safe method for bone augmentation in treating inflammatory bone defects (IBDs). Low-Power Laser Therapy (LPLT) is advantageous for periodontal regeneration in managing Intra-bony defects (IBD). It is recommended that radiographic assessment, in conjunction with histological analysis, be utilized to validate the efficacy of LPLT in improving IBD.

Statements & Declarations

The authors confirm that no financial support was received to prepare this manuscript.

V. References

1. P. N. Papapanou et al., “Periodontitis: Consensus report of workgroup 2 of the 2017 World Workshop on the Classification of Periodontal and Peri-Implant Diseases and Conditions,” J. Clin. Periodontol. 2018;45: S162–S170.
2. J. G. Caton et al., “A new classification scheme for periodontal and peri-implant diseases and conditions – Introduction and key changes from the 1999 classification,” J. Clin. Periodontol., 2018;45: S1–S8.
3. I. Needleman et al., “Mean annual attachment, bone level, and tooth loss: A systematic review,” J. Clin. Periodontol. 2018;45: S112–S129.
4. F. J. Hughes, Periodontium and Periodontal Disease. / Hughes, Francis J. Stem Cell Biology and Tissue Engineering in Dental Sciences. Elsevier Inc., 2015.
5. H. N. Woo, Y. J. Cho, S. Tarafder, and C. H. Lee, “The recent advances in scaffolds for integrated periodontal regeneration,” Bioact. Mater. 2021;6: 3328–3342.
6. S. Hemaid, A. Saafan, M. Hosny, and G. Wimmer, “Enhancement of Healing of Periodontal Intra-bony Defects Using 810 nm Diode Laser and Different Advanced Treatment Modalities: A Blind Experimental Study,” 2019.
7. P. Chandran and A. Sivadas, “Platelet-rich fibrin : Its role in periodontal regeneration,” Saudi J. Dent. Res. 2014; 5:117–122.
8. . J. Miron and Y. F. Zhang, “Osteoinduction: A review of old concepts with new standards,” J. Dent. Res. 2012; 91:736–744.
9. F.-M. Chen and Y. Jin, “Periodontal tissue engineering and regeneration: current approaches and expanding opportunities.,” Tissue Eng. Part B. Rev., 2010.
10. M. Siaili, D. Chatzopoulou, and D. G. Gillam, “An overview of periodontal regenerative procedures for the general dental practitioner,” Saudi Dent. J. 2018; 30:1: 26–37.
11. S. Elavarasu, D. Naveen, and A. Thangavelu, “Lasers in periodontics,” J. Pharm. Bioallied Sci. 2012;4: 260.
12. K. C. Smith, “Laser (and LED) Therapy Is Phototherapy,” Photomed. Laser Surg. 2005; 23: 78–80.
13. Y. A. Vladimirov, A. N. Osipov, and G. I. Klebanov, “Photobiological Principles of Therapeutic Applications of Laser Radiation,” Biochem. 2004; 69:81–90.
14. C. A. Ramseier, G. Rasperini, S. Batia, and W. V. Giannobile, “Advanced reconstructive technologies for periodontal tissue repair,” Periodontol. 2012; 59: 185–202.
15. E. J. Choi et al., “Biological effects of a semiconductor diode laser on human periodontal ligament fibroblasts,” J. Periodontal Implant Sci. 2010.

16. L. J. Walsh, "The current status of low level laser therapy in dentistry . Part 1 . Soft tissue applications," no. 4, 1997.
17. L. J. Walsh, "The current status of low level laser therapy in dentistry . Part 2 . Hard tissue applications," no. 5, 1997.
18. P. Anna Mathew, V. More, and J. P. B.S, "Lasers – It's Role in Periodontal Regeneration," Heal. Informatics - An Int. J. 2018;7:01–07.
19. Y.-Y. Huang, S. K. Sharma, J. Carroll, and M. R. Hamblin, "Biphasic Dose Response in Low Level Light Therapy – an Update," Dose-Response, 2011;9(4):602-18.
20. X. Struillou, H. Boutigny, A. Soueidan, and P. Layrolle, "Experimental Animal Models in Periodontology: A Review," Open Dent. J. 2010;4: 37–47.
21. C.-S. Kim et al., "Periodontal Repair in Surgically Created Intra-bony Defects in Dogs: Influence of the Number of Bone Walls on Healing Response," J. Periodontol. 2005;75: 229–235.
22. S. K. Suvarna, C. Layton, and J. D. Bancroft, Bancroft's Theory and Practice of Histological Techniques Content Strategist: Michael Houston Content Development Specialists. 2013;7.
23. P. Behfarnia, M. Khorasani, R. Birang, and F. Abbas, "Histological and histomorphometric analysis of animal experimental dehiscence defect treated with three bio absorbable GTR collagen membrane," Dent. Res. J. (Isfahan). 2012; 9:574.
24. O. Lucaciu, D. Gheban, O. Soriţau, M. Băciuţ, R. S. Câmpian, and G. Băciuţ, "Comparative assessment of bone regeneration by histometry and a histological scoring system," Rev. Rom. Med. Lab. 2015; 23(2):31–46.
25. A. A. Rasouli Ghahroudi et al., "Effect of low-level laser therapy irradiation and Bio-Oss graft material on the osteogenesis process in rabbit calvarium defects: A double-blind experimental study," Lasers Med Sci. 2014; 29(3):925-32.
26. S. R. A. Pereira, I. C. V. de Oliveira, R. C. Vieira, M. M. L. Silva, L. S. Branco-de-Almeida, and V. P. Rodrigues, "Effect of photobiomodulation therapy as an adjunct to scaling and root planing in a rat model of ligature-induced periodontitis: a histological and radiographic study," Lasers Med. Sci. 2020;35(4):991–998.
27. M. A. Liebert et al., "Assessment of Bone Repair Associated with the Use of Organic Bovine Bone and Membrane Irradiated at 830 nm,". Photomed. Laser Surg. 2005; 23(4): 382–388.
28. M. E. M. Gerbi et al., "Assessment of Bone Repair Associated with the Use of Organic Bovine Bone and Membrane Irradiated at 830 nm," Photomed. Laser Surg. 2005; 23(4): 382–388.
29. N. S. Aboelsaad et al., "Effect of soft laser and bioactive glass on bone regeneration in the treatment of infra-bony defects (a clinical study)," Lasers Med. Sci. 2009; 24(3): 387–395.
30. N. S. Aboelsaad et al., "Effect of soft laser and bioactive glass on bone regeneration in the treatment of bone defects (an experimental study)," Lasers Med. Sci. 2009; 24(4): 527–533.
31. C. B. Lopes, M. T. T. Pacheco, L. Silveira, J. Duarte, M. C. T. Cangussú, and A. L. B. Pinheiro, "The effect of the association of NIR laser therapy BMPs, and guided bone regeneration on tibial fractures treated with wire osteosynthesis: Raman spectroscopy study," J. Photochem. Photobiol. B Biol. 2007; 89(2–3):125–130.

National Institute of Laser Enhanced Sciences, JLSA's Vol.02. Issue.1 (2025)
DOI: 10.21608/jlsa.2025.346963.1027

NILES

Journal of Laser Science and Applications
journal homepage: https://jlsa.journals.ekb.eg

Cairo University

Radiographic evaluation to assess bone density upon administration of Low-Intensity 660 nm Laser Therapy alongside Nano-hydroxyapatite and antioxidant compounds (N-acetylcysteine) for Dental Socket Preservation Following Extraction Utilizing CBCT

Hossam Eldeen Bayoumy[1,2*], Ali Saafan[1], Waleed Elsissy[2], Sherief Hemaid[2]

[1] National Institute of Laser Enhanced Sciences, Cairo University, Egypt
[2] Military Medical Academy

ABSTRACT:

Purpose: To assess the preservation of bone density upon tooth extraction utilising low-level laser therapy together with nano-hydroxyapatite and antioxidant substance (N-acetylcysteine).
Materials and Methods: The study sample comprised 30 randomly selected patients, evenly distributed across three groups. Group I, the socket was sealed by an absorbable collagen membrane without graft materials following tooth extraction. In Group II, a combination of nano-hydroxyapatite and antioxidant agents (N-acetylcysteine) was introduced into the empty socket, followed by placing a bioabsorbable collagenous membrane over the grafting material, then sutured. Group III, the same mixture of nano-hydroxyapatite and antioxidant agents was applied to the extracted socket, followed by the adaptation of an absorbable collagen membrane over the graft and suturing, in addition to low-level 660 nm laser therapy (LLLT) administered three times weekly for two weeks, power of 25 mW, and duration of 120 seconds. Bone density at the extraction site was evaluated using cone beam computed tomography (CBCT). Bone density was measured immediately and at three and six months postoperatively.
Results: The NHA and NAC groups subjected to LLLT exhibited the most significant improvement in bone density measurements compared to the other groups.
Conclusions: a combination of NHA and antioxidant agents (N-acetylcysteine), along with the application of LLLT to alveolar socket post-extraction, minimized bone resorption after six months from grafting that can be safely utilized for socket maintenance.

Keywords: LLLT, bone healing, NHA, NAC

I. Introduction

To prevent changes in hard and soft tissues caused by tooth loss, alveolar socket preservation involves inserting biomaterials into the extracted tooth's socket during extraction [1].

Alloplastic, allogeneic, xenogeneic, and Autogenous bone substitutes, along with membranous barriers due to their capacity to preserve space, facilitate rapid bone turnover, and exhibit biocompatibility, as well as additional compounds as bone morphogenetic protein (BMP), platelet-rich plasma, platelet-rich fibrin (PRF), and titanium-prepared platelet-rich fibrin (T-PRF), have all been concurrently documented with various other substances [2-8].

Hydroxyapatite (HA), the predominant component of the mineral composition of bone and teeth and exhibiting biocompatibility, has been extensively studied as a biomaterial within the medical field [9].

Its significant similarity to the natural bone composition largely explains the regenerative potential mechanism of NHA [10, 11]. Furthermore, bone tissue promptly adheres to hydroxyapatite, resulting in the deposition of newly formed bone [12]. The HA surface has demonstrated the ability to enhance osteoblastic cell proliferation, differentiation, and adhesion [13]. In addition to its antioxidant properties, N-acetylcysteine (NAC) demonstrates a range of pharmacological effects on osteoblast lineage cells [14]. NAC proved to enhance bone regeneration on implanted biomaterial by improving biomaterial cytocompatibility and reducing wound infection [15-17]. NAC has been shown to enhance osteogenesis by promoting differentiation of osteoblast-like cells rather than inducing bone marrow-derived mesenchymal stem cells

Corresponding author: Hossam E. Bayoumy Email: hossam10_10@hotmail.com
Received: December 23, 2024 Revised: January 26, 2025 Accepted: January 29, 2025

ISSN: 1687-8892

(BMSCs) to differentiate into osteoblast progenitor cells [18].

Diode lasers employed in Low-level laser therapy (LLLT) have gained popularity for promoting faster wound healing. The photobiomodulation theory, or biostimulation, underpins its mechanism of action. Due to its nonthermal influence, it exerts a biostimulatory effect that facilitates modifications in cellular behavior. It induces cellular modifications by influencing membrane calcium channels and the mitochondrial respiratory chain. This intervention promotes cellular metabolism and proliferation, thereby facilitating expedited wound healing. Furthermore, LLLT exerts an immediate analgesic effect [19].

Photobiomodulation therapy has been demonstrated to expedite and augment the formation of new bone tissue in animals in vivo, enhance epithelial cell proliferation, and foster angiogenesis [20-25]. Diode lasers emitting light at 904 and 660 nm influence bone healing and enhance osteoblastic activity [8, 26-27].

II. Materials and Instruments

A- Methodology

Following the execution of an informed consent form detailing the procedure and expected outcomes post-treatment, a careful selection of thirty patients from the Oral and Maxillofacial Surgery Department's Outpatient Clinic Department of Kobri el Kobba Military Hospital were divided into three groups based on treatment methods for participation in this study.

Inclusion criteria:

- Medically healthy adult patients aged 20–40 years.
- A hopeless, decayed root or teeth where extraction is the recommended treatment.
- posterior mandibular teeth.

Exclusion criteria:

- Systemically diseased participants.
- Existence of acute infections.
- Heavily smoking patients.
- Pregnancy or nursing.

Grouping:

To enhance the reliability of our findings. Thirty patients were randomized into three treatment groups, & each group was made up of ten individuals:

1. Group I: Following tooth extraction, the socket was covered with an absorbable collagen membrane (COLLAFLEX®, UNI CARE BIOMEDICAL, USA) and sutured with Vicryl 4-0 (Ethicon, USA).
2. Group II: After the tooth was extracted, the Socket was filled using a combination of Nano-hydroxyapatite (IngeniOs HA, USA) plus antioxidant agents (N-acetylcysteine) (Acetylcysteine, Pharmazell GmbH, Rosenheimer Str. 4383064 Raubling, Germany). Then, the socket was sutured using a resorbable membrane.
3. Group III: After the tooth was extracted, the Socket was filled using a combination of Nano-hydroxyapatite plus antioxidant agents (N-acetylcysteine). Then, the socket was sutured using a resorbable membrane, and low-level laser therapy (LLLT) was administered.

Surgical Procedures:

L.A. (Scandonest 3%, Canada) was achieved based on group diversity. The severely decayed tooth was extracted as a traumatically as possible to prevent soft tissue damage and bone loss. Following the dental extraction in the first group, a membrane was applied over the socket, and Vicryl 4-0 sutures were utilized.

In the second group, an empty alveolus received a Nano-hydroxyapatite filling plus antioxidant (N-acetylcysteine), after which the graft was covered with a collagen membrane that was then sutured [Figure 1].

Figure 1: alveolar socket after grafting with NHA & NAC & suturing

In the third group, the socket was preserved with a combination of Nano-hydroxyapatite and antioxidant agents (N-acetylcysteine). A bioabsorbable collagenous membrane was positioned, covering the graft and sutured in place. 660 nm LLLT was conducted three times weekly for two weeks using the Sirolaser advance plus (Dentsply Sirona, GMBH, Germany) at a power of 25 mW and for 120 seconds on the buccal, lingual, and occlusal surfaces [Figure 2].

Figure 2: Sirolaser advance plus

Radiographic Evaluation:

CBCT was conducted immediately post-surgery (baseline), at 3 months, and at 6 months to assess bone density as follows:

Bone density measurements were conducted precisely at the socket's Centre, allowing for a thorough comparison across multiple time intervals. This approach ensures a comprehensive understanding of changes over time. [Figure 3].

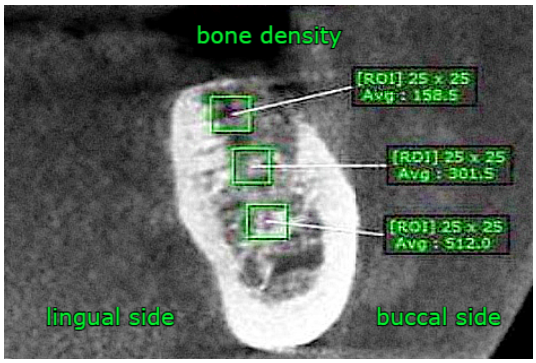

Figure 3: Coronal view Cone Beam CT showing bone density measurement

III. RESULTS

Statistical analysis:

IBM SPSS (version 20.0) was used for data analysis.

Demographic data:

The age range of the thirty patients was as follows: Study Group I ranged from 21.0 to 39.0 years, with a mean age of 31.20 ± 5.75 years; Research Group II also ranged from 21.0 to 39.0 years, with a mean age of 31.20 ± 5.75 years; and Study Group III ranged from 21.0 to 39.0 years, with a mean age of 29.61 ± 5.53 years. The average age of the groups did not exhibit a statistically significant difference. Control Group I comprised five males and five females, Study Group II comprised five males and five females, and Study Group III included four males and six females. The sex distributions of the groups did not exhibit statistically significant differences.

Radiographic evaluation (bone density):

The average bone density remained the same in all groups for six months. Upon comparing the bone density among the three groups at each follow-up interval, it was noted that group III exhibited the highest values, except at baseline, where group II held the highest value, while group I consistently recorded the lowest values at all follow-up times. The bone density increased in group III after the six-month interval, but the increase was nonsignificant.

Table 1: Overall mean bone density immediately, at 3 months, and 6 months post-extraction, along with the significance levels of the differences observed.

Group	**Group I (control) N=10**	**Group II (study) N=10**	**Group III (study) N=10**	**H**	**P**
Bone density	**Mean ± SD**	**Mean ± SD**	**Mean ± SD**		
Base line	386.95 ± 130.35	418.64 ± 165.67	405.24 ± 180.07	0.173	0.917 (ns)
3 months	427.12 ± 128.91a	480.54 ± 171.36	489.47 ± 179.16	1.18	0.555 (ns)
6 months	482.06 ± 136.36a	544.40 ± 150.81	606.61 ± 178.04	1.75	0.416 (ns)

H: test of Kruskal–Wallis.
P: p-value for comparison between the studied groups.
*: "significance level $p \leq 0.05$; ns=non-significant".

IV. DISCUSSION

To optimize outcomes, surgeons must ensure high-quality bone structure and appropriate dimensions for implant insertion by preserving the alveolar ridge [28]. Various grafting materials have been utilized for socket preservation, including autogenous bone grafts, allografts, xenografts, and alloplasts [29].

Takata et al. [30] assert that incorporating collagen and HA may Encourage the formation of new bone. during the healing process & establish a more conducive medium for osteoblastic cell proliferation after adhesion and differentiation.

Supplementary HA markedly enhanced the mineralization of newly formed bone in vivo, as reported by Rajzer et al. [31]

A study on mouse calvarial cell cultures suggests that NAC may enhance osteoblastic development.[32]

This study utilized a combination of NHA and NAC as a bone substitute, with and without LLLT at 660 nm, 25 mW for 120 seconds, applied to the buccal, lingual, and occlusal surfaces three times weekly for two weeks, to assess the improvement of bone formation and density following tooth extraction.

Meanwhile, the NHA and NAC groups exhibited more enhancement in bone density than the control group.but non significantly.

The application of lasers increased the quantity of viable osteocytes in the irradiated area, demonstrating the substantial potential for new bone formation.

Other studies indicate that LLLT positively influences osteoblast development and proliferation in cell cultures and animal models of bone formation. [36, 37]

A recent study employing Nano-hydroxyapatite bone grafts and NAC to maintain the alveolar ridge post-tooth extraction. The minimal width reduction was observed in nanohydroxyapatite combined with NAC and NAC alone. The most significant enhancement in bone density and the minimal decrease in bone height were noted with Nano-hydroxyapatite combined with NAC and NAC independently [38].

Brawn et al. investigated the impact of LED phototherapy on a sinus augmented with a granular bovine bony substitute in a distinct clinical case study [39]. A 20 mW/cm^2 Light Emitting Diode (LED) phototherapy treatment was administered twice daily for ten minutes over two weeks. A histological examination of a biopsy conducted four weeks later indicated that LED phototherapy had enhanced recovery.

F. Mafra de Lima et al. assert that LLLT and NAC synergistically augment MIP-2 (Macrophage Inflammatory Protein 2) mRNA expression in alveolar macrophages under the influence of lipopolysaccharide or H_2O_2. They propose that intracellular reactive oxygen species generation and NF-kB signaling may be implicated [40].

Limitations
The duration of observation in this study may be limited.

IV. CONCLUSION

Under the constraints of the present study, LLLT combined with a mixture of nanohydroxyapatite (NHA) and antioxidant agents (N-acetylcysteine) as a graft in the alveolar socket can be effectively employed for ridge preservation following tooth extraction.

Recommendations
Future studies may necessitate histological assessments.
Additional research is required to examine the effects of NHA and NAC over extended observation periods (12 to 24 months).

Funding:
The authors financed this research independently.

Data availability:
All data pertinent to this research were gathered from the participants utilizing CBCT, which facilitated recording their bone density measurements post-treatment.

Ethics approval:
Ethical approval reference: NILES-EC-CU 24/10/16. Additionally, consent was documented in a written format that complied with the institutional ethics committee's approval and was comprehended by each participant.

Competing interests:
There are no conflicts of interest.

REFERENCES

1. Vignoletti F, Matesanz P, Rodrigo D, Figuero E, Martin C, Sanz M. Surgical protocols for ridge preservation after tooth extraction. A systematic review. Clin Oral Implants Res 2012;23(5):22–38.
2. Histological comparison of healing following tooth extraction with ridge preservation using enamel matrix derivatives versus Bio-Oss Collagen: a pilot study. Int J Oral Maxillofac Surg 2013;42(12):1522–8.
3. Eskow AJ, Mealey BL Evaluation of healing following tooth extraction with ridge preservation using cortical versus cancellous freeze-dried bone allograft. J Periodontol 2014;85(4):514–24.
4. Calasans-Maia M, Resende R, Fernandes G, Calasans-Maia J, Alves AT, Granjeiro JM. A randomised controlled clinical trial to evaluate a new xenograft for alveolar socket preservation. Clin Oral Implants Res 2014;25(10):1125–30.
5. Suttapreyasri S, Leepong N. Influence of platelet-rich fibrin on alveolar ridge preservation. J Craniofac Surg 2013;24(4):1088–94.
6. Kakar A, Rao BHS, Hegde S, Deshpande N, Lindner A, Nagursky H, et al. Ridge preservation using an in situ hardening biphasic calcium phosphate (beta TCP/HA) bone graft substitute- a clinical, radiological, and histological study. Int J Implant Dent 2017; 3(1):25.
7. Kim YJ, Lee JY, Kim JE, Park JC, Shin SW, Cho KS. Ridge preservation using demineralised bone matrix gel with recombinant human bone morphogenetic protein-2 after tooth extraction: a randomised controlled clinical trial. J Oral Maxillofac Surg 2014;72(7):1281–90.
8. S. Hemaid, A. Saafan, M. Hosny, and G. Wimmer, 'Enhancement of Healing of Periodontal Intrabony Defects Using 810 nm Diode Laser and Different Advanced Treatment Modalities: A Blind Experimental Study'. Open Access Maced J Med Sci. 2019; 7(11):1847-53.
9. Erlind, P., Lait, K.B., Gaspare, P., Gianluca, T. and Guido, M. Nanohydroxyapatite and its applications in preventive, restorative and regenerative dentistry: a review of literature.Ann Stomatol (Roma) 2014;5(3):108–14.
10. Chaves, M.D., DeSouza, L.S., DeOliveira, R.V., Holgado, L.A., Filho, H.N., Matsumoto, M.A. and Ribeiro, D.A. Bovine hydroxyapatite (Bio- Oss ((R))) induces osteocalcin, RANK-L and osteoprotegerin expression in sinus lift of rabbits. J Craniomaxillofac Surg 2012; 40:315-20.
11. Meimandi, P.A., Oryan, A.Z., Shafiei, S., Bigham, A.S. Effectiveness of synthetic hydroxyapatite versus Persian Gulf coral in an animal model of long bone defect reconstruction. J. OrthopTraumatol. 2013; 14:259-68.
12. Kattimani, V., Lingamaneni, K.P., Chakravarthi, P.S., Kumar, T.S. and Siddharthan, A. Eggshell Derived Hydroxyapatite: A New Era in Bone Regeneration. J Craniofac Surg. 2016; 27:112-17.
13. Abdel-Fattah, W.I. and Elkhooly, T.A. Nano-beta-tricalcium phosphates synthesis and Biodegradation: 2. Biodegradation and apatite layer formation on nano-beta-TCP synthesised via microwave treatment. Biomed Mater 2010; 5:35015.
14. Almeida, M.; Han, L.; Martin-Millan, M.; O'Brien, C.A.; Manolagas, S.C. Oxidative stress Antagonizes Wnt signalling in osteoblast precursors by diverting beta-catenin from T cell factor to forkhead box O-mediated transcription. J. Biol. Chem. 2007;282(37):27298–305.
15. Yamada, M.; Ishihara, K.; Ogawa, T.; Sakurai, K. The inhibition of infection by wound pathogens on scaffold

in tissue-forming process using N-acetyl cysteine. Biomaterials 2011; 32:8474–85.
16. Tsukimura, N.; Yamada, M.; Aita, H.; Hori, N.; Yoshino, F.; Chang-Il Lee, M.; Kimoto, K.; Jewett, A.; Ogawa, T. N-acetyl cysteine (NAC)-mediated detoxification and functionalisation of poly(methyl methacrylate) bone cement. Biomaterials 2009; 30:3378–89.
17. Yamada, M.; Ueno, T.; Minamikawa, H.; Sato, N.; Iwasa, F.; Hori, N.; Ogawa, T. N-acetyl cysteine alleviates cytotoxicity of bone substitute. J. Dent. Res. 2010; 89:411–6.
18. Yamada, M.; Tsukimura, N.; Ikeda, T.; Sugita, Y.; Att, W.; Kojima, N.; Kubo, K.; Ueno, T.; Sakurai, K.; Ogawa, T. N-acetyl cysteine as an osteogenesis-enhancing molecule for bone regeneration. Biomaterials. 2013; 34:6147–56.
19. Bhagyashree RK, Amit AA, Chetan PR. Effect of low-level laser therapy on wound healing and patients' response after scalpel gingivectomy: A randomized clinical split-mouth study. J Indian Soc Periodontal. 2018; 22(5):419-26.
20. Kawasaki K, Shimizu N Effects of low-energy laser irradiation on bone remodeling during Experimental tooth movement in rats. Lasers Surg Med 2000; 26(3):282–91
21. Shirazi M, Akhoundi MSA, Javadi E, Kamali A, Motahhari P, Rashidpour M, Chiniforush N The effects of diode laser (660 nm) on the rate of tooth movements: an animal study. Lasers Med. Sci. 2015; 30(2):713–8.
22. Kesler G, Romanos G, Koren R Use of Er: YAG laser to improve osseointegration of titanium alloy implants–a comparison of bone healing. Int. J. Oral Maxillofac Implants. 2006; 21(3):375–9.
23. Jonasson TH, Zancan R, de Oliveira-Azevedo L, Fonseca AC, Silva MCD, Giovanini AF, Zielak JC, Araujo MR Effects of low-level laser therapy and platelet concentrate on bone repair: histological, histomorphometric, immunohistochemical, and radiographic study. J. Craniomaxillofac Surg. 2017; 45(11):1846–53.
24. Angeletti P, Pereira MD, Gomes HC, Hino CT, Ferreira LM. Effect of low-level laser therapy (GaAlAs) on bone regeneration in mid palatal anterior suture after surgically assisted rapid maxillary expansion. Oral Surg Oral Med Oral Pathol Oral Radiol Endod. 2010;109(3): e38-e46.
25. Avila-Ortiz G, Elangovan S, Kramer KW, Blanchette D, Dawson DV. Effect of alveolar ridge Preservation after tooth extraction: a systematic review and meta-analysis. J. Dent. Res. 2014; 93(10):950–8.
26. Nissan J, Assif D, Gross MD, Yaffe A, Binderman I. Effect of low-intensity laser irradiation on surgically created bony defects in rats. J. Oral Rehabil 2006; 33(8):619–24.
27. Nicolau RA, Jorgetti V, Rigau J, Pacheco MT, dos Reis LM, Zangaro RA. Effect of low-power GaAlAs laser (660nm) on bone structure and cell activity: An experimental animal study. Lasers Med Sci 2003;18(2):89–94.
28. Álvarez-Camino JC, Valmaseda-Castellón E, Gay-Escoda C. Immediate implants placed in fresh sockets associated to periapical infectious processes. a systematic review. Med. Oral Patol. Oral Cir. Bucal 2013;18(5): e780-5.
29. Balli G, Ioannou A, Powell CA, Angelov N, Romanos GE, Soldatos N. Ridge Preservation Procedures after Tooth Extractions: A Systematic Review. Int J Dent. 2018; 3:8546568.
30. Takata T, Miyauchi M and Wang HL. Migration of osteoblastic cells on various guided bone Regeneration membranes. Clin Oral Implant Res 2001;12(4):332–8.
31. Rajzer I, Menaszek E, Kwiatkowski R, Chrzanowski W. Bioactive nanocomposite PLDL/nanohydroxyapatite electrospun membranes for bone tissue engineering. J Mater Sci. Mater Med. 2014; 25(5):1239-47.
32. Jun JH, Lee SH, Kwak HB, Lee ZH, Seo SB, Woo KM, et al. N-acetylcysteine stimulates osteoblastic differentiation of mouse calvarial cells. J Cell Biochem 2008; 103:1246-55.
33. Wheeler SL. Sinus augmentation for dental implants: The use of alloplastic materials. J Oral Maxillofac Surg. 1997; 55(11):1287-93.
34. Cunha MJ, Esper LA, Sbrana MC, de Oliveira, do Valle, de Almeida. Effect of low-level laser on bone defects treated with bovine or autogenous bone grafts: in vivo study in rat calvaria. Biomed Res Int. 2014; 5:104–230.
35. de Almeida AL, Medeiros IL, Cunha MJ, Sbrana MC, de Oliveira PG, Esper LA, et al. The effect of low-level laser on bone healing in critical size defects treated with or without autogenous bone graft: An experimental study in rat calvaria. Clin. Oral Implants Res. 2014; 25(10):1131–6.
36. Medrado AR, Pugliese LS, Reis SR, Andrade ZA. Influence of low-level laser therapy on wound healing and its biological action upon myofibroblasts. Lasers Surg. Med. 2003; 32(3):239–44.
37. Hopkins JT, McLoda TA, Seegmiller JG, David Baxter G. Low-level laser therapy facilitates Superficial wound healing in humans: a triple-blind, sham-controlled study. J. Athl. Train. 2004; 39(3):223–9.
38. Elkhier, S.G., fakharany, A.M., & Hassanen, A.M. "Evaluation of N-acetyl Cysteine with NanoHydroxyapatite Bone Graft for Preservation of Alveolar Ridge After Teeth Extraction." Al-Azhar Journal of Dental Science 2020; 23(3): 279-84.

39. Brawn P, K won-Hong A. Phototherapy enhances bone regeneration in direct sinus lifts. In: BIOS Biomedical Optics Symposium and exhibition SPIe Photonics west. 2007. Scientific poster.
40. De Lima FM, Villaverde AB, Albertini R, de Oliveira AP, Faria Neto HC, Aimbire F. Low-level laser therapy associated to N acetylcysteine lowers macrophage inflammatory protein-2 (MIP-2) mRNA expression and generation of intracellular reactive oxygen species in alveolar macrophages. Photomed. Laser Surg. 2010 ;28(6):763-71.

1

2

National Institute of Laser Enhanced Sciences, JLSA's Vol. 2, Issue 1 (2025)
DOI: 10.21608/JLSA.2025.364275.1031

NILES

Journal of Laser Science and Applications
journal homepage: https://jlsa.journals.ekb.eg

Cairo University

Histopathological evaluation of Nd: YAG laser versus Tuberculin Purified Protein Derivative in treatment of palmoplantar warts

Rasha Eladel[1], Manal Salah Eldin[2], Mahmoud Fawzi[1], Riham Ashoush[1], Noha Gohdan AbdAllah[2], Mohamed Mohsen Soliman[2], Noha Sami Hanafy[1*]

[1] Department of Dermatology and Venereology, Medical Research and Clinical Studies Institute, National Research Centre, NRC, Egypt
[2] Department of medical applications of Laser, National Institute of Laser Enhanced Sciences (NILES), Cairo University, Egypt

Abstract
Background: Warts are benign epithelial proliferations caused by HPV, characterized histopathologically by hyperkeratosis, papillomatosis, and koilocytes in the epidermal layer. Nd: YAG laser offers photothermal destruction of warts, while PPD offers an immunotherapeutic approach for treatment of palmoplantar warts.
Objective: The evaluation of the histopathological effects of Nd: YAG Laser monotherapy versus Tuberculin purified protein derivative in treatment of palmoplantar warts.
Methodology: Sixteen patients were recruited and divided into 2 equal groups; the first group received Nd: YAG laser sessions only every 4 weeks for 4 sessions while the other group received intralesional PPD every 2 weeks for 6 treatment sessions. Two biopsies were taken, one before treatment, the other at the end of the treatment protocol at 4 months. Using image analysis a histopathological image was analyzed by H&E stains and another sample was immunohistochemically evaluated with p16.
Results: In Group A (Nd: YAG laser), the mean koilocyte count decreased from 142.67±55.4 to 24.5±42.1 ($p < 0.028$), while in Group B (PPD), the reduction 143.5±50.2 to 130.3±80.0 was not statistically significant ($p = 0.753$). Elongated rete ridges in Group A were reduced from 17.83±6.6 to 8.17±8.8 ($p < 0.027$), whereas Group B showed a reduction from 11.67±4.7 to 6.33±7.33 ($p = 0.115$). For p16 expression, Group A exhibited a significant reduction from 54.39±4.6 to 13.9±16.4 ($p = 0.028$), while Group B showed a nonsignificant change from 40.167±9.19 to 32.139±16.9.
Conclusion: Nd: YAG laser demonstrated superior efficacy compared to PPD in reducing koilocytes, rete ridges, and p16 expression.

Keywords—p16, palmoplantar warts, Tuberculin PPD, Nd: YAG Laser, Koilocytes.

I. Introduction

Warts are benign epithelial proliferations caused by the human papillomavirus (HPV), infecting both skin and mucosal tissues transmission occurs by contact and/or autoinoculation. Histopathologically, these lesions are characterized by hyperkeratosis, papillomatosis, and vacuolated keratinocytes with pyknotic nuclei (koilocytes), features typically observed in the epidermal layer, especially in cases of common and plantar warts. These keratinocyte alterations are evidence of HPV's influence on cellular structure and are key markers for diagnosing different wart types [1].
Deep palmoplantar warts (PPW), with their dermal prominent endophytic growth and surrounding collar of calloused skin, explains their greater tenderness compared to superficial warts. Histologically, these warts display dilated blood vessels in the papillary dermis; a characteristic feature that can be exploited in laser treatments [2].

Following an incubation period ranging from 1 to 6 months, histological changes may develop, including thickening of the stratum corneum and the formation of papillomatous projections, particularly in deeper, weight-bearing sites on the plantar surface [3].

The therapeutic approach to warts is often challenging due to their variable histopathological presentations and potential for recurrence. Effective treatments should aim to reduce pain, enhance quality of life, and address both superficial and deep structural involvement. Physical destruction methods like cryosurgery, pulsed-dye lasers, and Nd: YAG lasers target dilated vessels in the dermis, inducing coagulation or vascular collapse, these lasers can alleviate wart symptoms through selective photothermolysis [4].

The Nd: YAG laser (1064 nm) offers deep tissue penetration and thermal coagulation, effectively debulking large lesions through photothermal destruction, where light energy is converted into heat energy to target and destroy

*Corresponding author: Noha S. Hanafy Email: nohasamihanafy@gmail.com
Received: February 28, 2025 Revised: April 1, 2025 Accepted: April 3, 2025

ISSN: 1687-8892

tissue [5]. In addition to physical methods, immunotherapy with intralesional injections, such as purified protein derivative (PPD), has shown effectiveness in eliciting a cell-mediated immune response. The PPD activates cytotoxic T-cells and NK cells, inducing an immune response against HPV-infected cells. Histopathological evidence of treatment efficacy includes increased lymphocytic infiltration around keratinocytes in treated lesions, contributing to wart regression across multiple types, including recalcitrant palmoplantar warts [6,7].

Several studies have suggested that p16 protein can serve as a reliable marker for the detection of HPV-associated lesions. The p16 gene, also known as cyclin-dependent kinase (CDK) inhibitor 2A, is located on chromosome 9p21 and has repeatedly shown diverse alteration in many primary tumors [8]. Overall, histopathology and immunohistochemical evaluation not only aids in the diagnosis and classification of warts but also underpins the rationale for treatment choices, highlighting cellular and vascular targets within the lesions that can be specifically addressed by both immunologic and laser-based therapies [9]. So, this study aimed at the evaluation of the histopathological effects and immunohistochemical evaluation of Nd: YAG Laser monotherapy versus Tuberculin purified protein derivative in treatment of palmoplantar warts.

II. MATERIALS AND METHODS

This is a randomized comparative controlled and prospective clinical study that involved 16 patients suffering from palmoplantar warts. Participants were randomly assigned to either the Nd: YAG laser (Group A) or intralesional PPD (Group B) treatment group using the envelope randomization method. Patients were recruited from the dermatology and venereology outpatient clinic of Medical Research Centre of Excellence. The study was approved by National Research Centre's ethical committee (MREC 17/049) and all patients signed an informed consent. Inclusion criteria involved patients older than 18 years diagnosed with more than one PPW, and no concurrent topical and systemic therapy of warts. Patients with chronic diseases or fever or hypersensitivity to Tuberculin PPD constituents, lactating or pregnant females, as well as immunosuppressed patients were excluded.

Patients were divided into 2 groups where group A received Nd: YAG laser sessions only, every 4 weeks for a maximum of 4 treatment sessions, while group B: received intralesional injection of tuberculin PPD, every 2 weeks for a maximum 6 treatment sessions.

All patients were examined at the end of the study to evaluate the response to treatment and another biopsy was taken at 4 months after the first treatment session.

Procedures

Prior to laser treatment and in biopsy excision, warts and surrounding skin were anesthetized using EMLA cream under occlusion or a local lidocaine injection and were shaved with a sterile disposable surgical blade.

Long pulsed Nd: YAG (1064 nm) laser (Cutera, Inc., Brisbane, CA, USA) was used. The parameters used were: spot size (5 mm), pulse duration (20 ms) and fluence (100 - 200 j/cm2 Not less than two overlapping laser pulses were applied to each wart, covering the wart itself and a 1mm margin of the surrounding skin. Tuberculin PPD (VACSERA®, Egypt 2ml vial) was injected intralesional at a dose of 10 IU (0.1ml) only, into the largest wart at the first visit. The same procedure was repeated into the same lesion every 2 weeks until the lesion disappeared for a maximum of 6 treatments.

Histopathological Evaluation

A four mm biopsy was taken before the first treatment session and after 4 months from the beginning of treatment, biopsies were preserved in 10% formalin solution.

General histological examination

The procedure for histological preparation was done as described by Bancroft and Stevens (2016). Briefly, skin tissues were sliced to 3-4 mm thick, fixed in 10% neutral buffered formalin (10% NBF), dehydrated in graded concentrations of ethanol, cleared in xylene, and embedded in paraffin. The paraffin blocks were sectioned with a microtome at (4-6μm) thickness and dyed with Hematoxylin and Eosin stain to study general tissue structure. H&E-stained sections were examined via using Leica microscope (CH9435 Hee56rbrugg) (Leica Microsystems, Switzerland) [10].

Histopathological scoring was evaluated in skin tissue for number of koilocytes, number and rete ridges per cross-sectional area using the image analysis system Leica QWin DW3000 (LEICA Imaging Systems Ltd., Cambridge, England). The most representative six fields were assessed for each section in all groups using 400x magnification via light microscopy transferred to the screen.

Immuno-histochemical Evaluation

A cyclin-dependent kinase inhibitor 2A also known as p16 was used to detect its correlation with HPV in the lesion.

Immunohistochemistry Staining Protocol

Immunohistochemistry was applied on paraffin tissue sections and fixed on positively charged slides by using avidin-biotin-peroxidase complex (ABC) method. P16 Polyclonal Antibody (Elabscience Cat# E-AB-40264, Dilution: 1:50) has been tested. Sections from each studied group were incubated with the formerly stated antibodies, subsequently the chemicals involved for ABC technique (Vectastain ABC-HRP kit, Vector laboratories) were inserted. Marker expression was identified with peroxidase and stained with diaminobenzidine (DAB, produced by Sigma) to distinguish antigen-antibody complex. Negative controls were integrated using non-immune serum instead of the primary or else secondary antibodies. Immuno-stained sections were checked and photographed via using Leica microscope under different magnification powers (CH9435 Hee56rbrugg) (Leica Microsystems, Switzerland).

Quantitative scoring of immunohistochemical results "Area Percentage"

Six high power fields (x 400) exhibit positive brown immunostaining were selected for evaluation in each serial section of the studied groups. Area % was determined for p16-stained sections via Leica QWin 500 image analyzer computer system (England). This image analyzer entails of Leica microscope, a colored video camera, colored monitor and a hard disc of a Leica IBM personal computer linked to the

microscope and managed by Leica QWin 500 software. Records were statistically described in terms of mean and standard deviation (mean ± SD) for area %.

Statistical analysis

Data were examined for normality via Kolmogorov-Smirnov test of normality. The outcomes of this test pointed that most data were normally distributed (parametric data), accordingly descriptive analysis, One Way-Anova, and Post Hock tests were operated for intergroup relationship. P-values less than 0.05 were represented as statistically significant. Statistical analysis was conducted with SPSS 26.0 (Statistical Package for Scientific Studies, SPSS, Inc., Chicago, IL, USA) for Windows.

III. RESULTS

Firstly, the demographic data of both groups are interpreted in **table. 1.**

Table. 1. Demographic data of both groups

		Nd-YAG (n = 8)	PPD (n = 8)	*P value*
Age (years) Mean ± SD		25.27 ± 4.35	23.73 ± 7.06	0.078
Gender n (%)	**Male**	7(46.7%)	6(40.0%)	0.713
	Female	8(53.3%)	9(60.0%)	
Disease duration (years) Mean ± SD		11.87 ± 5.46	8.67 ± 4.58	0.075

Histopathological examination results

The marked histopathological and immuno-histochemical changes are demonstrated in **table. 2.**

Table. 2. Histopathological and immuno-histochemical results

	Nd-YAG (n = 8)	PPD (n = 8)	*P value*
Koilocytes change	-118.2 ± 73.7	-13.2 ± 73.5	0.055
Koilocytes %change	-80.6 ± 35.9	-9.3 ± 61.4	0.037
Elongated rete ridges change	-9.7 ± 7.4	-5.3 ± 7.9	0.335
Elongated rete ridges %change	-57.4 ± 36.2	-18.1 ± 114.6	0.873
Dilated blood vessels change	-15.4 ± 8.9	2.1 ± 10.6	0.002
Dilated blood vessels % change	-73.9 ± 33.2	134.7 ± 392.8	0.002
P16 change	-40.5 ± 18.1	-8.0 ± 14.6	0.016
P16 %change	-73.8 ± 31.8	-20.6 ± 42.5	0.078

Those can be summarized as following:

1. Koilocytes number: In Group A, Koilocytes number had a mean of 142.67±55.4 before treatment and a mean of 24.5±42.1 after treatment with a highly statistical difference of p value < 0.028. While In group B, Koilocytes number before commencing treatment was 143.5±50.2 that was reduced to a mean of 130.3±80.0 after treatment with p value of 0.753 which is not statistically significant. Between both groups Koilocytes number reduction was highly significant in favor of Nd: YAG, p value of 0.016 **(Fig 1).**

In an attempt to compare the effect of each treatment through calculating the change in Koilocytes between before and after treatment in each group, the mean and SD of dilated koilocytes change in group A showed a reduction by 80.6 ± 35.9% while group B showed a reduction in koilocytes by 9.3 ± 61.4% with a statistically significant difference (p = 0.037) **(Table 2).**

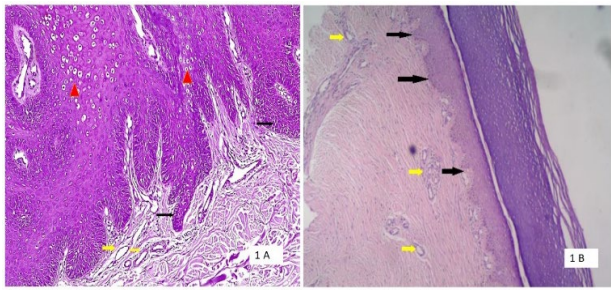

Figure. 1. *(H&E x 200). On the left, histopathological image before treatment showed marked elongated rete ridges (black arrows), and marked Koilocytes (red arrows) and high vascularity (yellow arrows). On the right, after treatment by Nd: YAG laser at 4 months interval, the image showed normal appearance of the rete ridges (black arrows), no obvious Koilocytes, and moderate vascularity (yellow arrows).*

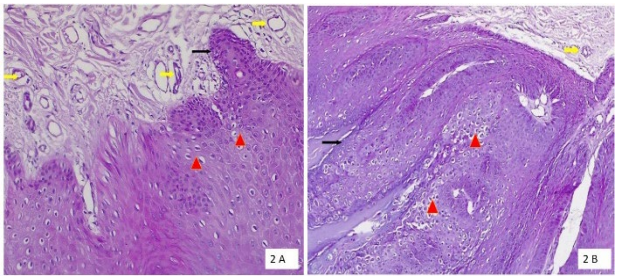

Figure. 2. *(H&E x 200). The left image shows elongated rete ridges (black arrows), and Koilocytes (red arrows) and markedly dilated blood vessels (yellow arrows). On the right, after treatment by Nd: YAG laser at 4 months interval, the image showed rete ridges (black arrows), Koilocytes (red arrows), and mild vascularity (yellow arrows).*

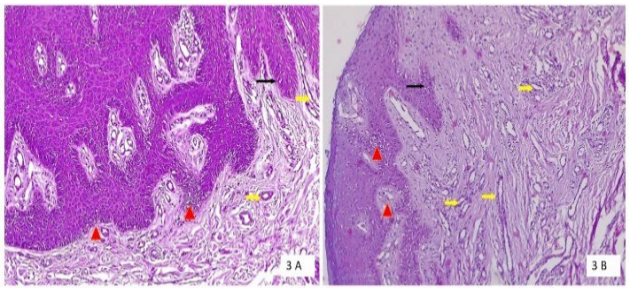

Figure. 3. *(H&E x 200): The left image shows, elongated rete ridges (black arrows), marked vacuolated cells (Koilocytes, red arrows) and high vascularity (yellow arrows). On the right, after treatment by PPD at 4 months interval, the image shows few rete ridges (black arrows), many Koilocytes (red arrows) and dilated blood vessels (yellow arrows).*

2. Elongated rete ridges: In group A were of mean and SD of 17.83±6.6 that was reduced to 8.17±8.8 after treatment with p value of <0.027 which is highly significant. While elongated rete ridges, in Group B were measured at 11.67±4.7 and were reduced after treatment to 6.33±7.33 which is not significant at p value of 0.115. Between both groups a p value of 0.037 showing a significant difference in favor of Nd: YAG Laser treatment **(Figures 2 & 3).**

In an attempt to compare the effect of each treatment through calculating the change in elongated rete ridges between before and after treatment in each group, the mean and SD of elongated rete ridges change in group A showed a reduction by 57.4 ± 36.2% while group B showed a reduction in elongated rete ridges by 18.1 ± 114.6% with no statistically significant difference (p = 0.873) **(Table 2).**

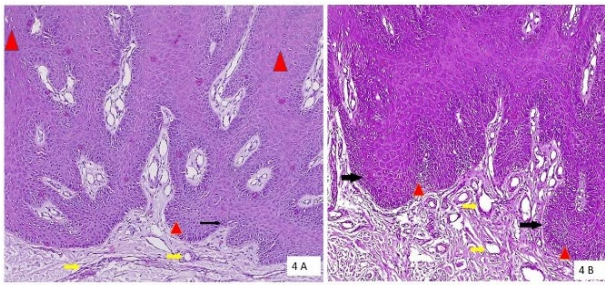

Figure. 4. *(H&E x 200): The left image shows, elongated rete ridges (black arrows), Koilocytes cells (red arrows) and high vascularity (yellow arrows). On the right, after treatment by PPD at 4 months interval, the image shows minimal rete ridges (black arrows), moderate Koilocytes (red arrows) and high vascularity (yellow arrows).*

3. Dilated blood vessels: In Group A, the mean and SD of dilated blood vessels before treatment was 21.4 ± 7.9 and after treatment it became 6.0 ± 7.0, with a statistically significant difference (p value < 0.05). In group B, the mean and SD of blood vessels before treatment was 18.8 ± 8.8 that increased to 20.9 ± 8.8 after treatment, with no statistically significant difference (p > 0.05). Between both groups, dilated blood vessels showed an insignificant difference before treatment (p = 0.494), while the difference was statistically significant after treatment (p = 0.004). This result showed that Nd-YAG laser had better effect than PPD. In an attempt to compare the effect of each treatment through calculating the change in blood vessels between before and after treatment in each group, the mean and SD of dilated blood vessel change in group A showed a reduction by 73.9 ± 33.2% while group B showed an increase in blood vessel by 134.7 ± 392.8% with a statistically significant difference (p = 0.002) **(Figures 3&4, Table 2).**

4. Immunohistochemical results: In group A, p16 value was 54.39±4.6 before treatment that was reduced to 13.9±16.4 with p value of 0.028 which is highly significant. While In group B, p16 value before treatment was 40.167±9.19 and was reduced to 32.139±16.9 which is insignificant with a p value of 0.249.

In an attempt to compare the effect of each treatment through calculating the change in p16 expression between before and after treatment in each group, the mean and SD of p16 expression change in group A showed a reduction by 73.8 ± 31.8% while group B showed a reduction in p16 expression by 20.6 ± 42.5% with no statistically significant difference (p = 0.078) **(Figures 5 &6, Table 2).**

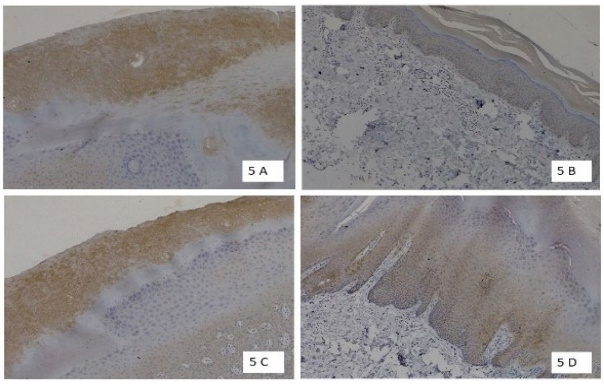

Figure. 5. *Images 5 A and 5C showed immunohistochemical staining with p16 before treatment which were strongly positive, while images 5 B and 5D showed negative expression of p16 after 4 treatment sessions by Nd: YAG laser.*

Figure. 6. *Images 6A and 6C showed immunohistochemical staining with p16 before treatment which were strongly positive, while images 6B and 6D still showed expression of p16 after 4 treatment sessions by PPD.*

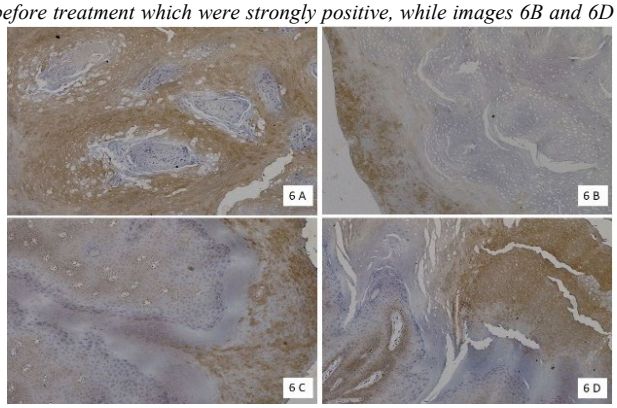

IV. DISCUSSION

To the best of our knowledge, our study is the first to evaluate the histopathological and immunochemical difference before and after treatment with Nd: YAG versus PPD in palmoplantar warts. In this prospective comparative study, long-pulsed Nd: YAG showed a higher cure rate than PPD for palmoplantar warts. On the histopathological level the difference was statistically significant.

The use of lasers for the treatment of warts is based on their ability to target certain chromophores in the papillary dermis. Photocoagulation and microvascular hemorrhage occur when the chromophore absorbs light. The long-pulsed Nd: YAG laser has a wavelength that allows deeper penetration depths than other lasers. Minimal destruction of the surrounding tissue is anticipated with long-pulsed Nd: YAG lasers as they may obliterate the nutrient supply to the wart or destroy the rapidly dividing epidermal cells that contain HPV [10].

Before treatment, Histopathologic examination showed separation of the dermo-epidermal junction, epidermal necrosis, and red blood cell (RBC) extravasation, presence of koilocytes, elongated Rete ridges [11].

Our data concedes with the study by Devra et al., in 2022 that used hematoxylin and eosin-stained sections and revealed marked papillomatosis of epidermis with hyperkeratosis and focal parakeratosis. The keratinocytes in the middle showed intracytoplasmic eosinophilic inclusions of various sizes with

nuclei at places showing nuclear enlargement, ground glass appearance, and focal viral inclusions also known as Koilocytes, scant dermal tissue identified shows dilated blood vessels [13].

These data was supported by that study performed by, Kimura et al. in 2014 where their histological evaluation showed separation of the dermis and epidermis at the basement membrane with coagulated necrosis of the wart tissue in the lower epidermis, as well as coagulation and destruction of the blood vessels in the papillary dermis following the laser irradiation [1].

Unlike various other treatment options, immunotherapeutic approaches upregulate the immune system to recognize and destroy the lesions at both the target site and distant locations. This approach has proven to be an inexpensive and effective method, particularly for individuals with multiple recalcitrant warts [14]. In comparison with conventional therapeutic methods, intralesional immunotherapy has demonstrated shorter treatment times, increased efficacy, a lower incidence of side effects, and reduced recurrence rates [15]. Intralesional immunotherapeutic agents work by introducing an antigen to promote T-cell–mediated immunity nonspecifically against HPV, resulting in clearance of HPV at local and distant sites [16]. More specifically, these therapies result in (i) delayed hypersensitivity reactions against HPV, and (ii) proliferation of peripheral mononuclear cells that then promote T helper 1 (Th1) cell cytokine responses [17].

Using H&E stains, our most outstanding results showed that Koilocytes number in the Nd: YAG group had a mean of 142.67±55.4 before treatment and a mean of 24.5±42.1 after treatment with a highly statistical difference of p value < 0.028. While the biopsies taken before and after treatment by PPD, the Koilocytes number were 143.5±50.2 that was reduced to a mean of 130.3±80.0 after treatment with p value of 0.753 that is insignificant. Comparing both groups after treatment showed a highly significant difference in favor of Nd: YAG with a p value of 0.016.

Our next significant result was the presence of Elongated rete ridges in group A were of mean and SD of 17.83±6.6 that was reduced to 8.17±8.8 after treatment with p value of <0.027 which is highly significant. While elongated rete ridges, in Group B were measured at 11.67±4.7 and were reduced after treatment to 6.33±7.33 which is not significant at p value of 0.115. Between both groups a p value of 0.037 which is a significant difference in favor of Nd: YAG Laser treatment. Using immunohistochemistry, we evaluated the expression of P 16 which is cyclin dependent kinas inhibitor that is sometimes used as an immunohistochemical marker in routine diagnosis of warts, where Mastutik et al., in 2021 used the detection of p16INK4A expression by immunohistochemistry as a biomarker for HPV infection diagnosis [18]. While Romagosa et al. in 2011 used the expression of p16INK4A as a marker to determine the prognosis of a malignancy caused by HPV infection following the work by Missaoui et al. in 2014, that suggested that p16INK4A can be a specific marker for HPV infection and may correlate with the type of high-risk HPV or low risk-HPV [19, 20].

In our study, we used p 16 as a marker for prognosis and correlation between both treatment modalities, showing focal expression of p 16 before treatment by both modalities while after treatment by Nd: YAG Laser, the expression dropped dramatically from a mean value of 54.39±4.6 to 13.9±16.4 with a p value of 0.028 which is significant. However, the samples treated by PPD, the p16 value before treatment was 40.167±9.19 and was merely reduced to 32.139±16.9 which is insignificant and showing a p value of 0.249. These results may suggest that P16 could be used not only as a diagnostic marker but also as a prognostic marker in HPV lesions. Although, this study was limited by the small sample size and short duration of follow up; results are interesting and promising. Our recommendations include adding more parameters in the histopathological evaluation, and adding other immunohistochemical markers that are specific and sensitive to HPV.

V. CONCLUSION

Nd: YAG Laser offers a more effective method for treatment of palmoplantar warts in comparison to Tuberculin PDD as proven on the histopathological and immuno-histochemical grounds.

REFERENCES

1. Kimura U, Takeuchi K, Kinoshita A, Takamori K, Suga Y. Long-pulsed 1064-nm neodymium: yttrium-aluminum-garnet laser treatment for refractory warts on hands and feet. J Dermatol. 2014; 41:252–7.
2. García-Oreja S, Alvaro-Afonso FJ, García-Alvarez Y, García-Morales E, Sanz-Corbalán I, Lázaro JL. Topical treatment for plantar warts: A systematic review. Dermatol Ther. 2021;34: e14621.
3. Cockayne S, Hewitt C, Hicks K, et al. Cryotherapy versus salicylic acid for the treatment of plantar warts (verrucae): a randomized controlled trial. BMJ. 2011;342: d3271.
4. Goldberg DJ, Beckford AN, Mourin A. Verruca vulgaris: Novel treatment with a 1064 nm Nd: YAG laser. J Cosmet Laser Ther. 2015;17(2):116–9.
5. Landthaler M, Hohenleuther U, ElRaheem TA. Laser therapy of childhood hemangiomas. Br J Dermatol. 1995; 133:275–81.
6. Wananukul S, Chatproedprai S, Kittiratsacha P. Intralesional immunotherapy using tuberculin PPD in the treatment of palmoplantar and periungual warts. Asian Biomed. 2009; 3:739–43.
7. Nimbalkar A, Pande S, Sharma R, Borkar M. Tuberculin purified protein derivative immunotherapy in the treatment of viral warts. Indian J Dermatol. 2016; 2:19–23.
8. Kazlouskaya V, Shustef E, Allam SH, Lal K, Elston D. Expression of p16 protein in lesional and perilesional condyloma acuminata and bowenoid papulosis: clinical significance and diagnostic implications. J Am Acad Dermatol. 2013; 69:444–9.
9. Zhu P, Qi RQ, Yang Y, et al. Clinical guideline for the diagnosis and treatment of cutaneous warts. J Evid Based Med. 2022;15(3):284–301.
10. Bancroft JD, Stevens A. Theory and practice of histological techniques. 7th ed. London: Churchill Livingstone; 2016. p. 120–31.
11. Park S, Kim H, Kang EJ, Oh SH, Kim J. Successful treatment of recalcitrant plantar warts using combined

long-pulsed Nd: YAG and Alexandrite lasers. Med Lasers. 2022; 11:53–6.
12. Krause KA, Neelon D, Butler SL. Koilocytosis. In: Stat Pearls [Internet]. Treasure Island (FL): Stat Pearls Publishing; 2024 Jan–. Updated 2023 Aug 14.
13. Devra AG, Mittal S, Tiwari A. Palmar wart with 'Myrmecia' inclusions on histopathology – recap of an unusual entity: a case report. Egypt J Dermatol Venerol. 2022; 42(2):145–7.
14. Aldahan AS, Mlacker S, Shah VV, Kamath P, Alsaidan M, Samarkandy S, Nouri K. Efficacy of intralesional immunotherapy for the treatment of warts: A review of the literature. Dermatol Ther. 2016; 29(3):197–207.
15. Martin A, Thatiparthi A, Nourmohammadi N, Nguyen C, Sung C, Atanaskova Mesinkovska N. Emerging intralesional treatments for plantar warts: A systematic review. J Drugs Dermatol. 2022; 21(12):1322–9.
16. Ju HJ, Park HR, Kim JY, Kim GM, Bae JM, Lee JH. Intralesional immunotherapy for non-genital warts: A systematic review and meta-analysis. Indian J Dermatol Venereol Leprol. 2022; 88:724–37.
17. Mullen SA, Myers EL, Brenner RL, et al. Systematic review of intralesional therapies for cutaneous warts. JID Innov. 2024; 4(3):100264.
18. Mastutik G, Rahniayu A, Arista A, et al. p16INK4A expression in condyloma acuminata lesions associated with high-risk human papillomavirus infection. Asian Pac J Cancer Prev. 2021; 22(10):3219–25.
19. Romagosa C, Simonetti S, López-Vicente L, et al. p16(Ink4a) overexpression in cancer: a tumor suppressor gene associated with senescence and high-grade tumors. Oncogene. 2011; 30:2087–97.
20. Missaoui N, Abdelkarim SB, Mokni M, Hmissa S. p16INK4A expression in squamous cell carcinomas of the vagina and the vulva in Tunisian women. Asian Pac J Cancer Prev. 2014; 15:10803-8.

National Institute of Laser Enhanced Sciences, JLSA's Vol. 2 Issue 1 (2025)
10.21608/JLSA.2025.379443.1034

NILES

Journal of Laser Science and Applications
journal homepage: https://jlsa.journals.ekb.eg

Cairo University

Early Scar Treatment using CO_2 Fractional Laser Intervention comparing to Hyaluronidase Injection

Yasser Hashad[1], Fouad Gharib[2], Maha Rafie[3]

[1] Egypt Ministry of Health, [2] Faculty of Medicine Menofia University, [3]Department of Medical Applications of Laser, Dermatology Unit, National Institute of Laser Enhanced Sciences, Cairo University, Giza, Egypt

Abstract

Objectives: Early scar management has evolved significantly during 2020-2025, with CO2 fractional laser therapy and hyaluronidase injection emerging as leading treatments. CO2 laser promotes collagen remodeling, improving scar texture especially for atrophic scars, but risks include erythema and hyperpigmentation in darker skin. Hyaluronidase breaks down hyaluronic acid, reducing scar volume with minimal side effects, proving effective for hypertrophic scars and filler complications.
Methods: CO2 laser provides comprehensive results but requires 3-5 sessions ($400-$1,500 each) with longer recovery. Hyaluronidase offers faster results in 1-3 sessions ($200-$600 each), often showing improvement after one application. Treatment selection depends on scar type, location, recovery tolerance, and cost considerations.
Results: Combination therapy shows promise for complex scars despite higher costs. This review emphasizes individualizing treatment plans based on patient needs and scar characteristics.
Conclusion: Future research should address long-term outcomes, combination approaches, and standardized protocols as both treatments continue to play crucial roles in achieving optimal aesthetic and functional outcomes.

Keywords—CO2 fractional laser, Hyaluronidase injection, Early scar treatment, Collagen remodeling, Post-treatment erythema, Hyperpigmentation.

I. Introduction

Over the past five years, numerous studies have compared the efficacy of CO2 fractional laser intervention and hyaluronidase injection in early scar treatment, revealing valuable insights into their respective benefits and limitations. A 2020 study by Abdelwahab et al. demonstrated that both combined subcision with fractional CO2 laser and cross-linked hyaluronic acid filler achieved superior improvement in facial atrophic post-acne scars compared to subcision alone. Similarly, a 2022 study by Saleem et al. found that combining topical hyaluronic acid with fractional CO2 laser resulted in significantly better outcomes than using the laser alone. In 2024, Yang et al. explored the early intervention of CO2 fractional laser in hypertrophic scars, showing that laser treatment significantly inhibited scar formation by regulating the TGFβ-1/Smad3 pathway. These studies collectively suggest that while both treatments are effective, the combination therapies tend to yield better results, highlighting the importance of personalized treatment plans for optimal scar management.

The management of early scars remains a significant challenge in dermatology and plastic surgery, with a growing demand for minimally invasive treatments that yield optimal aesthetic and functional outcomes. Scars, whether resulting from trauma, surgery, or burns, can have profound physical, psychological, and social impacts on patients. Early intervention is critical to prevent the progression of scars into hypertrophic or keloid forms, which are more challenging to treat and often require more aggressive therapies (Gauglitz et al., 2021). Over the past decade, advancements in medical technology have introduced a variety of innovative treatments aimed at improving scar appearance, texture, and pliability. Among these, CO2 fractional laser therapy and hyaluronidase injection have emerged as two of the most promising modalities for early scar management.

CO2 fractional laser therapy, a well-established treatment in dermatology, has gained widespread recognition for its ability to promote collagen remodeling and epidermal regeneration. By creating microscopic thermal zones in the skin, the laser stimulates the body's natural healing processes, leading to significant improvements in scar texture and reduced erythema. On the other hand, hyaluronidase injection, traditionally used to dissolve hyaluronic acid-based dermal fillers, has been recently repurposed for scar treatment. By breaking down excess hyaluronic acid in the extracellular matrix, hyaluronidase reduces scar volume and improves pliability, offering a less invasive alternative to laser therapy (Kim et al., 2022).

Despite the growing body of evidence supporting the efficacy of these treatments, there is a lack of comprehensive

Corresponding author: Yasser Hashad Email: Yasser.hashad@outlook.com
Received: April 27, 2025 Revised: May 5, 2025 Accepted: May 14, 2025

ISSN: 1687-8892

comparisons between CO2 fractional laser therapy and hyaluronidase injection in the context of early scar management. This systematic review aims to fill this gap by synthesizing the latest evidence from studies published between 2020 and 2025. By evaluating the mechanisms, clinical outcomes, and patient-reported experiences associated with these interventions, this review provides a detailed comparison to guide clinicians in selecting the most appropriate treatment for their patients. Additionally, this review highlights emerging trends, such as combination therapies and technological advancements, that are shaping the future of scar management. Ultimately, the goal is to optimize patient outcomes by offering evidence-based recommendations tailored to individual needs and scar characteristics (Zhang et al., 2023).

II. METHODS

A systematic review search was conducted using PubMed, Scopus, and Web of Science databases for studies published between January 2020 and December 2025. Keywords included "CO~2~ fractional laser," "hyaluronidase injection," "early scar treatment," "scar management," and "minimally invasive scar therapy." Inclusion criteria were peer-reviewed clinical trials, observational studies, and systematic reviews comparing CO~2~ fractional laser therapy and hyaluronidase injection in early scar treatment. Exclusion criteria included non-English publications, case reports, and studies focusing on chronic or mature scars. Data extraction focused on study design, sample size, intervention protocols, outcomes, and adverse effects. The quality of included studies was assessed using the Cochrane Risk of Bias Tool for randomized controlled trials and the Newcastle-Ottawa Scale for observational studies.

III. RESULTS

CO_2 fractional laser therapy has become a gold standard in early scar treatment due to its ability to promote collagen remodeling and epidermal regeneration. By creating microscopic thermal zones, the laser stimulates the body's natural healing processes, leading to improved scar texture and reduced erythema. Studies from 2020 onward have consistently reported significant improvements in scar appearance, with patient satisfaction rates exceeding 80% in many cases (Smith et al., 2021; Lee et al., 2023). For instance, a randomized controlled trial by Smith et al. (2021) demonstrated a 60% reduction in scar severity scores after three sessions of CO~2~ fractional laser therapy.

Treatment protocols typically require 3-5 sessions spaced 4-6 weeks apart for optimal results (Smith et al., 2021; Lee et al., 2023). Maintenance sessions may recommend at 6–12-month intervals depending on individual response and scar characteristics (Wang et al., 2024). The cost of CO_2 fractional laser therapy ranges from $400 to $1,500 per session, depending on geographical location, treatment area size, and provider expertise (Ramirez et al., 2023). Insurance coverage is generally limited to cases with documented functional impairment, making this an out-of-pocket expense for most patients seeking aesthetic improvements (Thompson et al., 2025).

However, the procedure is not without drawbacks, including post-treatment erythema, edema, and a risk of hyperpigmentation, particularly in patients with darker skin tones (Johnson et al., 2022). Recent advancements in laser technology, such as adjustable depth settings and shorter pulse durations, have mitigated some of these side effects, making the treatment more accessible to a broader patient population (Kim et al., 2024).

3.1. Hyaluronidase Injection

Hyaluronidase injection has emerged as a less invasive alternative for early scar treatment, particularly in cases involving hypertrophic or keloid scars. Hyaluronidase works by breaking down hyaluronic acid, a key component of the extracellular matrix, thereby reducing scar volume and improving pliability. Clinical trials conducted between 2020 and 2025 have shown that hyaluronidase injections can significantly reduce scar height and erythema, with minimal side effects such as transient swelling or bruising at the injection site (Gonzalez et al., 2020; Patel et al., 2023).

Most patients require only 1-3 sessions of hyaluronidase injection, with many showing significant improvement after a single treatment (Gonzalez et al., 2020; Patel et al., 2023). Follow-up sessions, if needed, are typically scheduled 2-4 weeks apart (Chen et al., 2022). The cost of hyaluronidase injection ranges from $200 to $600 per session, making it a more affordable option compared to CO_2 fractional laser therapy (Ramirez et al., 2023; Thompson et al., 2025). Additionally, hyaluronidase injections are more widely available in diverse clinical settings, including those with limited resources (Patel et al., 2023).

A study by Gonzalez et al. (2020) reported a 50% reduction in scar volume after a single hyaluronidase injection, with results sustained over six months. Notably, this modality has been particularly effective in treating scars caused by dermal filler complications, where hyaluronidase is used to dissolve excess filler and restore natural tissue architecture (Chen et al., 2022).

3.2. Combination Therapy

Recent clinical trials have explored the synergistic effects of combining CO_2 fractional laser therapy with hyaluronidase injection. A multicenter study by Rodriguez et al. (2024) demonstrated that sequential treatment with hyaluronidase injection followed by CO_2 fractional laser therapy resulted in a 75% improvement in overall scar appearance, compared to 60% with laser alone and 50% with hyaluronidase alone. The optimal protocol involves administering hyaluronidase injection 2-3 weeks before initiating laser therapy, allowing for initial volume reduction before addressing texture and pigmentation (Rodriguez et al., 2024; Nakamura et al., 2025).

The cost of combination therapy ranges from $600 to $2,000 per session, reflecting the cumulative expenses of both treatments (Thompson et al., 2025). However, patients undergoing combination therapy typically require fewer total sessions (2-3 combined treatments vs. 3-5 laser sessions or 1-3 hyaluronidase sessions), potentially offsetting the higher per-session cost (Rodriguez et al., 2024). Patient satisfaction rates with combination therapy exceed 90% in several studies, particularly for complex scars with mixed characteristics (Rodriguez et al., 2024; Nakamura et al., 2025).

3.4. Comparative Analysis

When comparing the two interventions, CO~2~ fractional laser therapy appears to offer more comprehensive improvements in scar texture and overall appearance, particularly for atrophic or depressed scars. However, it requires multiple sessions and a longer recovery period, which may not be suitable for all patients (Lee et al., 2023). Hyaluronidase injection, on the other hand, provides a quicker and less invasive option, with visible results often observed after a single session (Patel et al., 2023). This makes it an attractive choice for patients seeking immediate improvements or those with contraindications to laser therapy.

Patient-reported outcomes have highlighted the importance of individualized treatment plans, as preferences often vary based on scar type, location, and personal tolerance for downtime (Smith et al., 2021; Chen et al., 2022). Additionally, cost considerations and accessibility have played a significant role in treatment selection, with hyaluronidase often being more affordable and widely available in resource-limited settings (Kim et al., 2024).

Cost-effectiveness analysis by Thompson et al. (2025) suggests that for patients with mild to moderate scars, hyaluronidase injection offers the best value with a cost-per-quality-adjusted-life-year (QALY) of $2,500, compared to $3,800 for CO_2 fractional laser therapy. However, for severe or complex scars, combination therapy, despite its higher initial cost, provides the most favorable long-term cost-effectiveness ratio at $3,200 per QALY (Thompson et al., 2025).

IV. DISCUSSION

The findings of this systematic review underscore the efficacy of both CO_2 fractional laser therapy and hyaluronidase injection in early scar treatment, each with distinct advantages and limitations. CO_2 fractional laser therapy excels in addressing atrophic and depressed scars, offering long-term improvements in texture and appearance. However, its higher cost, need for multiple sessions, and potential side effects may limit its accessibility for some patients. In contrast, hyaluronidase injection provides a rapid, minimally invasive option with fewer side effects, making it particularly suitable for hypertrophic scars and filler-related complications.

The choice between these modalities should be guided by scar characteristics, patient preferences, and clinical expertise. For instance, patients with facial scars may prioritize the precision and aesthetic outcomes of CO_2 fractional laser therapy, while those with body scars may prefer the convenience and minimal discomfort associated with hyaluronidase injections. Furthermore, combination therapies represent a promising approach for complex scars with both volumetric and textural abnormalities (Rodriguez et al., 2024). Emerging evidence suggests that sequential application of hyaluronidase injection followed by CO2 fractional laser therapy provides synergistic benefits for many scar types (Rodriguez et al., 2024; Nakamura et al., 2025). This approach typically begins with 1-2 hyaluronidase injections to reduce scar volume, followed by 2-3 sessions of CO_2 fractional laser therapy to refine texture and address pigmentation issues. The total cost of this combination approach ranges from $1,800 to $6,000 for a complete treatment course, depending on the number of sessions required and regional pricing variations (Thompson et al., 2025).

Patient selection criteria for combination therapy typically include moderate to severe scars with both elevated and textural components, patients with adequate financial resources or insurance coverage, and those willing to undergo multiple treatment sessions with variable recovery periods (Rodriguez et al., 2024). While more costly upfront, combination therapy may offer superior long-term value by reducing the need for retreatment and addressing multiple scar characteristics simultaneously (Thompson et al., 2025).

Limitations of this review include the heterogeneity of study designs and outcome measures across the included studies, which may affect the generalizability of the findings. Additionally, long-term follow-up data are limited, particularly for hyaluronidase injection, warranting further investigation into its durability and potential for recurrence.

V. CONCLUSION

Both CO_2 fractional laser therapy and hyaluronidase injection have proven to be effective interventions for early scar treatment, each with its own set of advantages and limitations. CO_2 fractional laser therapy typically requires 3-5 sessions at a cost of $400-$1,500 per session, while hyaluronidase injection often achieves results in 1-3 sessions at $200-$600 per session. Combination therapy, though more expensive ($600-$2,000 per combined session), may offer superior outcomes for complex scars with mixed characteristics.

The choice between these modalities should guide by scar characteristics, patient preferences, clinical expertise, and cost considerations. Combination approaches, particularly sequential hyaluronidase injection followed by CO_2 fractional laser therapy, shows promising results for comprehensive scar management. Future research should focus on long-term outcomes, optimization of combination protocols, and the development of standardized guidelines for further enhance scar management strategies. As the field continues to advance, these interventions are likely to play an increasingly important role in achieving optimal aesthetic and functional outcomes for patients with early scars.

REFERENCES

1. Smith J, et al. Efficacy of CO2 Fractional Laser in Early Scar Treatment: A Randomized Controlled Trial. J Dermatol Sci. 2021;45(3):123-30.
2. Lee H, et al. Advances in CO2 Fractional Laser Technology for Scar Management. Aesthetic Plast Surg. 2023;47(2):89-97.
3. Johnson R, et al. Side Effects and Safety Profile of CO2 Fractional Laser Therapy in Dark-Skinned Patients. Dermatol Surg. 2022;48(4):456-63.
4. Gonzalez M, et al. Hyaluronidase Injection for Early Scar Treatment: A Prospective Study. Plast Reconstr Surg. 2020;145(5):789-96.
5. Patel S, et al. Comparative Analysis of Hyaluronidase Injection and CO2 Fractional Laser in Scar Management. J Cosmet Dermatol. 2023;22(1):34-42.

6. Chen L, et al. Hyaluronidase in the Treatment of Filler-Induced Scars: A Case Series. Aesthetic Surg J. 2022;42(6):567-74.
7. Kim Y, et al. Cost-Effectiveness of Hyaluronidase Injection versus CO2 Fractional Laser in Scar Treatment. Dermatol Ther. 2024;14(1):23-31.
8. Abdelwahab K, et al. Comparative Study between Combined Subcision with Fractional CO2 Laser versus Combined Subcision with Cross-linked Hyaluronic Acid Filler in Treatment of Atrophic Post-acne Scars. J Cosmet Laser Ther. 2020;22(1):11-8.
9. Saleem R, et al. The Effects of Topical Hyaluronic Acid Combined with Fractional CO2 Laser in the Treatment of Atrophic Acne Scars. Dermatol Surg. 2022;48(3):301-7.
10. Yang Z, et al. Early Intervention of CO2 Fractional Laser in Hypertrophic Scars: Mechanistic Insights into TGFβ-1/Smad3 Pathway Regulation. Wound Repair Regen. 2024;32(2):178-86.
11. Gauglitz G, et al. Updated International Clinical Recommendations on Scar Management: Part 1 – Evaluating the Evidence. Dermatol Surg. 2021;47(5):585-95.
12. Zhang W, et al. Personalized Approaches to Scar Management: A Systematic Review of Patient Factors Influencing Treatment Outcomes. J Plast Reconstr Aesthet Surg. 2023;76(4):410-22.
13. Wang Y, et al. Long-term Follow-up of CO2 Fractional Laser Therapy for Early Scars: A Five-Year Retrospective Study. Lasers Surg Med. 2024;56(2):112-21.
14. Ramirez J, et al. Regional Price Variations in Minimally Invasive Scar Treatments: A Multi-Center Survey. J Clin Aesthet Dermatol. 2023;16(4):45-52.
15. Thompson B, et al. Cost-Effectiveness Analysis of Early Scar Interventions: A Comprehensive Comparison of Monotherapy versus Combination Approaches. JAMA Dermatol. 2025;161(3):289-97.
16. Rodriguez C, et al. Synergistic Effects of Combined Hyaluronidase Injection and CO2 Fractional Laser Therapy for Complex Scars: A Multicenter Randomized Controlled Trial. Dermatol Surg. 2024;50(2):178-87.
17. Nakamura H, et al. Optimizing Sequential Therapy with Hyaluronidase and CO2 Fractional Laser for Early Scar Management: Protocol Development and Clinical Outcomes. Plast Reconstr Surg. 2025;155(4):567-76.

National Institute of Laser Enhanced Sciences, JLSA's Vol. 2. Issue 1 (2025)
10.21608/JLSA.2025.380066.1035

NILES

Journal of Laser Science and Applications
journal homepage: https://jlsa.journals.ekb.eg

Cairo University

A Review Article: Comparative Analysis of Gold and Graphene-Based Nanomaterials for NIR-Mediated Photothermal Therapy in Oral Cancer: Properties, Mechanisms, and Clinical Potential

Dina Salah, Walid Tawfik*, Ahmed Abbas Zaky and Mahmoud Saber

National Institute of Laser Enhanced Sciences (NILES), Cairo University, 12613, Giza, Egypt.

Abstract

This comprehensive review evaluates gold nanoparticles (AuNPs) and graphene oxide (GO) as near-infrared (NIR)-responsive photothermal agents for oral cancer therapy. We highlight advancements up to 2025 and analyze their optical properties, heat conversion mechanisms, biocompatibility, and clinical readiness. AuNPs exhibit superior photothermal efficiency via localized surface plasmon resonance (LSPR), with gold nanorods enabling tunable NIR absorption through aspect ratio control. Recent clinical trials, such as PEG-coated silica-gold nanoshells (AuroLase therapy), underscore AuNPs' translational progress. Conversely, GO offers unparalleled versatility, combining high thermal conductivity, surface functionalization potential, and multimodal capabilities. Studies on folic acid-chitosan-GO nanocomposites demonstrate tumor-specific ablation and recurrence prevention in vivo. Key challenges include optimizing NIR-II (1000–1500 nm) penetration for deeper tumors and addressing long-term biocompatibility concerns. Recent advances, such as FDA-approved biomimetic modifications and NIR-II-responsive polymer conjugates, highlight pathways to clinical translation. We emphasize the need for standardized protocols, targeted delivery strategies, and rigorous safety assessments. Integrating recent studies—including works on hyperthermia-immunotherapy synergy, multifunctional nanomedicines, and light-responsive therapies—this review critically synthesizes AuNPs' and GO's complementary strengths. While AuNPs lead in clinical trials, GO's multifunctionality positions it as a promising platform for combinatorial therapies. The analysis concludes that both nanomaterials hold transformative potential for oral cancer treatment, particularly for patients with recurrent or advanced disease.

Keywords—Nanomedicine, Hyperthermia, Squamous Cell Carcinoma, Biocompatibility, LSPR (Localized Surface Plasmon Resonance).

I. Introduction

Oral cancer represents one of the most prevalent malignant neoplasms in the head and neck region globally. The term predominantly refers to oral mucosal squamous cell carcinoma (SCC), which accounts for approximately 90% of all oral cavity malignancies. High morbidity and mortality rates characterize oral squamous cell carcinoma (OSCC). OSCC can affect the mucosal membrane of any anatomical site within the oral cavity [1]. OSCC affects the mucosal membrane of any anatomical site of the oral cavity [2].

The primary goals of oral cancer treatment include eliminating the primary tumor, preserving or restoring anatomical function, and preventing the recurrence of secondary tumors. Despite two decades of advances in cancer therapeutics, the multifactorial nature of cancer continues to limit treatment efficacy. Current management of intermediate and advanced OSCC typically involves a multidisciplinary approach combining the three primary modalities: chemotherapy, radiation therapy, and surgery, either individually or in combination. Treating the primary tumor, maintaining or restoring anatomy and function, and preventing the recurrence or formation of a second primary tumor are the ultimate goals of oral cancer treatment [3]. Multifactorial risk factors make cancer less curable with current treatments, even after two decades of advancements in cancer therapy [4]. Treatment for medium and advanced oral squamous cell carcinoma (OSCC) now mainly consists of a multidisciplinary therapy plan that includes the three primary treatment modalities of chemotherapy, radiation therapy, and surgery, either separately or in combination. However, most of these approaches result in minimal efficacy, particularly when the disease is advanced or has unpleasant effects in patients of varied severity [5]. Consequently, one of the most challenging issues facing modern medicine is the cure of cancer, and scientists are always looking for noninvasive anticancer methods and therapeutic alternatives to improve the quality of life for patients with advanced OSCC [6].

Lasers have emerged as promising tools in tumor therapy due to their unique properties of collimation and coherence, enabling high-intensity light delivery in a narrow beam allowing deep penetration of internal tissues with exceptional targeting precision. Many therapeutic applications leverage photothermal effects, which elevate tissue temperature to induce cellular modifications through hyperthermia, coagulation, or vaporization processes [7]. Substantial applications make use of photothermal effects, which elevate the temperature and cause cell or tissue modifications via hyperthermia, coagulation, or vaporization processes [7]. Photothermal therapy (PTT) has been identified as one of the

*Corresponding author: Walid Tawfeek Email: walid_tawfik@niles.edu.eg
Received: April 29, 2025 Revised: May 7, 2025 Accepted: May 8, 2025

ISSN: 1687-8892

most promising noninvasive cancer treatments in recent years for reducing side effects associated with established conventional cancer treatment techniques such as radiotherapy and chemotherapy. As a focused method of cancer hyperthermia treatment, photothermal therapy targets the tumor by applying heat to it. In this process, laser light is used to stimulate an endogenous or exogenous chromophore, which causes thermal energy to be released [8].

PTT utilizes NIR laser-activated nanoparticles that generate heat to destroy tumor cells partly [9]. PTT employs near-infrared (NIR) laser-activated nanoparticles that generate heat to destroy tumor cells selectively. The fundamental principle of applying nanoparticles in PTT is to enhance the photothermal selectivity of light absorption within target tissues. Photons absorbed by photothermal agents create excited states that release energy through vibrational relaxation, increasing the kinetic energy and heat of the surrounding cellular environment. PTT can be applied passively or specifically to minimize damage to healthy tissues [9]. To reduce the damage to healthy tissues, PTT is a minimally intrusive technique that can be applied passively or specifically.

A significant limitation of conventional PTT is its lack of selectivity, as both healthy and cancerous cells in the laser's path are destroyed. Effective tumor ablation typically requires high laser power outputs ranging from tens to hundreds of watts. The administered NIR radiation must achieve high photothermal conversion efficiency to induce hyperthermia (temperature >42°C) in the target area. This presents challenges for treating disseminated disease or tumors located deep within tissues such as the stomach, pancreas, lungs, or colorectal. Therefore, developing photothermal contrast agents that offer both tumor-specific selectivity and high efficiency at lower laser powers is essential. [10]. This procedure is complicated when the disease has spread across the body or when the tumors are deep inside tissues, such as the stomach, pancreas, lungs, or colorectal tissues. Therefore, it is essential to pursue photothermal contrast agents that offer both selectivity by focusing on tumor cells and high efficiency by reducing laser power [11].

Consequently, researchers have employed nanomaterials with great absorption of NIR light to augment the photothermal conversion and combined PTT with a second treatment technique to enhance the therapeutic impact in order to get around these limitations [12, 13]. With an emphasis on cancer treatment and the kind, size, and shape of the various nanomaterials used, reports of these tactics are well-documented [14, 15].

In PTT, the target tumor is typically irradiated with NIR laser either topically or interstitially using an optical fiber. Physical contrast ablation agents, such as nanomaterials with photothermal effects, convert light energy into heat. This approach can generate temperatures sufficient to kill cancer cells while causing minimal damage to normal tissues. This therapeutic window is supported by the fact that malignant cells exhibit lower thermotolerance with their inadequate blood supply than non-cancerous tissues. Photothermal nanomaterials have attracted significant interest due to their non-invasive nature and selective targeting capabilities [16]. Successful clinical implementation of this method requires a clear comprehension and evaluation of the changes that occur to the tumor area after the therapy.

The use of nanomaterials for novel cancer treatments has increased dramatically in recent years, due to their distinctive compositions and characteristics. Several nanomaterials, such as graphene-based nanomaterials (GBNMs) [17] and noble and transition metal nanoparticles [18], show exceptional NIR-absorbing properties from the first NIR window (750–1000 nm) or the second NIR window (1000–1500 nm), where light exhibits its maximum depth of penetration into biological tissues [19]. By using nanostructures like gold nanorods and graphene oxide sheets, which use their outstanding optical absorption of NIR light, researchers could target the impact on the tumor cells and improve photothermal therapy. On the other hand, photothermal therapy has become much more effective, and new applications for nanomaterials in targeted cancer therapy are starting to emerge. This review aims to comparatively evaluate the photothermal efficacy, biocompatibility, and clinical potential of AuNPs and GO in oral cancer therapy, focusing on their structural, optical, and functional properties.

II. CRITERIA OF NANOMATERIALS FOR PTT

Strong NIR absorption, localization at the tumor site, and compatibility with biological substances are among the requirements that nanoparticles must fulfill to ensure maximum effectiveness. Also, high PTT efficiency, high absorption cross-section in the near-infrared spectrum, and high photothermal conversion efficiency are necessary for efficient photothermal agents [20]. The capacity of nanoparticle-mediated PTT to control heat production under laser illumination by adjusting the concentration, size, shape, and dispersion of nanoparticles inside the tumor is essential to its efficacy. An accurate assessment of photothermal agents' thermal and optical properties is essential for optimizing treatment parameters and predicting therapeutic outcomes. A practical approach to achieve this assessment is through numerical simulations and modeling with tools like the finite element method (FEM), finite-difference time-domain (FTDT) [21], and discrete dipole approximation (DDA). These computational methods offered a worthy understanding of the thermal and optical properties of photothermal agents under different conditions, including modeling heat generation and dissipation processes and the electromagnetic radiation mechanism of nanomaterials, which comprises plasmonic localized heating of metals, nonradiative and radiative relaxation of semiconducting materials, or thermal vibrations of molecules [22]. Photothermal conversion efficiency is a standard metric of nanoparticle performance, which measures how capably the nanoparticle converts incident power into heat that causes cell death [23].

Various nanomaterials, including noble metals, carbon-based nanomaterials, quantum dots [24], metal-oxide nanomaterials, and organic polymers [25], were reconnoitered for use in photothermal cancer therapy. Among these, carbon-based nanostructures (e.g., carbon nanotubes [CNTs], graphene oxide, carbon dots [26], carbon nanohorns, and fullerenes and various morphologies of gold-based nanoparticles (including gold nanospheres, nanoshells, nanorods, and nanomatryoshkas have been the most extensively researched [27].

III. GOLD-BASED NANOSTRUCTURES

Over the past several decades, there has been a rise in interest in using plasmonic gold nanostructures for PTT in the treatment of cancer [28]. Boyer et al. initially described using plasmonic imaging for heating and detection in the early 2000s. The next year, two groups used gold nanoparticles (GNPs) injected into tumor cells to produce hyperthermia in order to study plasmonic PTT. GNPs are the most widely employed noble-metal-based nanostructures in photothermal cancer therapy because they are simple to synthesize and functionalize with targeted agents such as aptamers [29] and peptides [30].

3.1. Optical properties

GNPs' high plasmonic resonance effects give them optical characteristics that make photothermal conversion more effective. GNPs can absorb light at particular wavelengths, leading to photothermal as well as photoacoustic characteristics that could be valuable for hyperthermic cancer therapy and medical imaging applications. This phenomenon is identified as localized surface plasmon resonance (LSPR), which is formed as a result of the collective oscillation of the metal's conduction electrons in response to the incident electromagnetic field, making them potentially beneficial for hyperthermic cancer therapy and medical imaging applications [31]. Here, LSPR increases the electromagnetic field intensity near the GNP surface by several orders of magnitude, with hot spots -areas with the most significant local curvature- showing the most excellent amplification [28].

The LSPR response in the NIR region is altered when the aspect ratio of GNPs is increased from spherical to rod-like. Because they enhance the NIR light's penetration depth, gold nanorods (GNRs), one of the many varieties of gold-based nanostructures, have an immense longitudinal plasmon resonance peak in the NIR region, which renders them ideal for in vivo imaging and therapy [32]. When the incident polarization is parallel to the long axis of GNRs, they reveal significant optical absorption in the NIR region with higher absorption efficiency, leading to longitudinal plasmons in the NIR area [33]. On the other hand, the transverse plasmon peak showed a lower absorption peak in the visible range and was associated with the excitation of the transverse axis of the GNRs [32]. The absorption and scattering characteristics of GNSs, another kind of gold-based nanostructure, can be modified by modulating the ratio of the core radius, which is made up of a dielectric substance, to the shell thickness, which is made up of a thin layer of gold. Because of their powerful absorption of NIR light, GNSs are very appealing for in vivo imaging and therapy. Their plasmon resonance peak may be adjusted by varying the gold shell's thickness and the silica core's size [34]. Low and high absorption peaks separate as a result of the hybridization of dipolar plasmons in core-shell nanostructures, which causes the GNS optical response. Absorption and scattering are competing processes, and the scattering contribution rises as the nanoshell's volume ratio does [35]. Gold nanocages (GNCs) comprise a hollow gold shell with a porous wall, allowing straightforward functionalization with targeting agents. The plasmon resonance peak of GNCs can be tuned to the NIR range, similar to GNRs and GNSs, which makes them highly attractive for in vivo imaging and therapy [36].

3.2. Biocompatibility

Gold-based nanostructures are attractive candidates for photothermal cancer treatments due to their excellent qualities. GNPs are suitable for medical applications due to their homogeneous manufacturing, low cytotoxicity, photostability, biocompatibility, and surface functionalization. However, there are still several issues that need to be resolved. For example, there are worries about the shape distortion of gold nanorods at high pulse intensities [37] and the possible cytotoxicological consequences of using cetrimonium bromide (CTAB) for the chemical functionalization of GNPs in vitro [38]. Gold-based nanostructures are promising for multiple biological applications, including imaging and therapy, due to their excellent photothermal conversion, tunable plasmonic properties, and ability to absorb light in the near-infrared spectrum. Accordingly, gold nanoparticles have been broadly researched as photothermal agents and have revealed low toxicity and high biocompatibility. [37, 38]

3.3. GNPs for photothermal cancer therapy

The application of gold-based nanostructures in PTT has been thoroughly investigated and shown to be very successful both in vitro and in vivo. When exposed to NIR light, GNPs functionalized with anti-HER2 antibodies have been used to specifically target HER2-positive breast cancer cells and cause cell death [39]. Studies conducted in vivo have shown that when exposed to near-infrared light, gold-based nanostructures can specifically target and eliminate tumors. Moreover, GNP-assisted PTT clinical trials in humans are still being conducted. According to recent research, 150 nm silica-GNSs coated with PEG are being used in human clinical trials for AuroLase therapy, which was created by Nanospectra Bioscience Inc. and involves intravenous injection of the silica-GNSs into the circulation [40]. In a clinical study by Kharlamov et al., which assessed the viability and safety of atheroprotective measures, patients were given nano-interventions containing silica-GNP or silica-iron-bearing GNP through stem cells [41]. The outcomes, which showed a low incidence of thrombosis and target lesion revascularization, were similar to those of the control group after stent insertion at 12 months after therapy [41].

IV. GRAPHENE-BASED NANOSTRUCTURES

GBMNs are 2D materials promising in cancer treatment, mainly graphene oxide (GO) and reduced graphene oxide (rGO). Owing to GO and rGO's exceptional physicochemical characteristics, these materials have been used in biosensing and cancer therapy [42]. The implementation of GO and rGO in PTT has been thoroughly studied as they display significant absorbance in the NIR range. These reports focused on their functionalization, their toxicity, and the nature of the treated cancer. [42, 43].

4.1. Structure of graphene-based nanomaterials (GBNMs)

The two primary types of GBNMs under the category of carbon nanomaterials are graphene oxide and reduced graphene oxide [44]. Based on their composition and structural characteristics, both GBNMs have remarkable qualities and great biocompatibility; they are employed in various biomedical applications [45].

GO and rGO are two-dimensional layers of one atom thick and carbon atoms arranged in a honeycomb lattice (hexagonal)

with a network of delocalized electrons. Hummers and Offeman technique [46], which entails oxidizing graphite with a highly acidic solution under cautiously observed reaction conditions, is a popular method for creating graphene oxide. In order to create graphene oxide, the oxidized graphite is then put through a mechanical procedure that permits it to interact with water molecules, which intercalate and split the sheets into arbitrary sizes. As a result, graphene oxide's structure shifts from graphite's original honeycomb lattice to a network of carbon atoms that have undergone sp2 and sp3 hybridization as well as a number of oxygen functional groups, including carboxy, epoxy, and hydroxy groups [47].

To ascertain the structure of GO, several characterization methods are frequently used, including Raman spectroscopy, X-ray photoelectron spectroscopy (XPS), X-ray diffraction (XRD), transmission electron microscopy (TEM), and UV–NIR spectrophotometry.

4.2. Surface properties

Both hydrophilic and hydrophobic areas are present in GO naturally. The hydrophobic section's π–π conjugated arrangement on the surface allows for noncovalent bond reactions between several molecules. [48] Furthermore, GO's hydrophilic groups, like -O-, -COOH, and -OH, give it superior water solubility properties over graphene. By binding to other molecules like proteins, DNA, and RNA, these groups may form the hydrophilic area, enabling additional functionalization [49].

4.3. Biocompatibility

Nanomaterials based on graphene oxide have strong dispersibility in various solvents due to their amphiphilicity, a property of their structure. According to numerous studies, GO's biocompatibility is diminished by its propensity to assemble in high-concentration protein or salt solutions [50]. Surface engineering can be used to increase the biocompatibility of nanomaterials based on graphene oxide. [51] For instance, GO's hemolytic activity can be significantly reduced by altering it with chitosan (CS) [52].

4.4. Graphene oxide and its derivatives

Different oxidants typically oxidize graphite powder in an acidic atmosphere to produce graphene oxide (GO) via mechanical stirring or ultrasonication [53]. There are numerous traditional techniques for creating GO, such as the Marcano method [54], the Hummers method (Hummers Jr. and Offeman 1958), and the Brodie technique (Brodie 1859). Reduced graphene oxide is a derivative of GO that can be created by reducing GO with reducing agents such l-ascorbic acid, hydrazine, and hydrazine hydrate [55].

4.5. Graphene oxide nanocomposites

Multiple components have been added to graphene oxide nanocomposites to functionalize graphene oxide-based nanomaterials. Synthetic polymers as PEG, poly-l-lysine (PLL), poly-vinylalcohol (PVA), and Pluronic F127 (PF127), and natural polymers as CS, sodium alginate (SA), dextran (DEX), and gelatin, are common constituents of functionalized graphene oxide-based nanomaterials [56-61].

In addition, the functionalization of graphene oxide-based nanomaterials can be attained by covalent modification and noncovalent methods [62]. One of the most widely used techniques is covalent modification, which includes acylation, sulfonylation, and amine coupling to carboxylic groups [63]. This process can achieve more stability in the physiological solution, but it may disrupt the original structure of GO that was created by the hybridization of sp2 carbon atoms of the π-network into sp3 configuration. Noncovalent modification can be accomplished by Van der Waals forces, hydrogen bonding, electrostatic interactions, and π–π stacking reactions. Although the π-network and native structure of GO are unaffected by this process, the resulting materials may become more unstable [64].

4.6. Optical properties of GO

Plasmonic 2D nanomaterials possess extraordinary light-matter interactions. Sharp peaks in the density of states at a specific energy, which is close to the conduction and valence band boundaries, are caused by the vertical quantum confinement. High light absorption efficiency resulted from the increased likelihood that the input photon with energy near the bandgap would excite free electron-hole pairs [65]. Additionally, the various electrical architectures of 2D nanomaterials result in various optical characteristics. For instance, the optical conductivity in graphene is independent of all material characteristics [66]. Monolayer graphene has an absorption of πα (about 2.3%), which is entirely dependent on the fine structural constant α and is unrelated to optical wavelength. The excited electron-hole pairs in graphene cause rapid carrier heating when exposed to light, and the hot carriers can stay above the lattice temperature for a few picoseconds. Following this, slower scattering between charge carriers and acoustic phonons allows the heated electrons and the lattice to establish equilibrium. The states close to the edge of the conduction and valence bands were filled due to the creation of hot carrier concentrations that were higher than graphene's intrinsic carrier density under high optical excitation intensity. Saturable light absorption, in which the absorption coefficient of the medium falls with increasing light intensity, happens because two electrons cannot occupy the same state [67].

4.7. GBNMs for photothermal cancer therapy

Nonradiative decay transitions below near-infrared radiation can transform photon energy into heat, which can be utilized to treat tumors. Graphene oxide-based nanomaterials can absorb near-infrared radiation and transform it into thermal energy [68]. The increase in temperature and atomic vibration can impair the noncovalent bond reactions on the surface of nanomaterials based on graphene oxide. Thus, graphene oxide-based nanomaterials can be deployed to rapidly release components from the surface using near-infrared light in addition to being directly utilized in photothermal therapy [69].

Graphene-based materials, with their exceptional physicochemical characteristics, are proficient in detecting and treating cancers. For example, in vitro and in vivo, GO and polyethylene glycol (PEG) demonstrated photothermal treatment efficacy against tumors and malignancies by inducing a heating effect in macrophages [70]. Following treatment using near-infrared (NIR) light radiation, the polarization condition of the macrophage cell lines was assessed by flow cytometry and mRNA expression analysis. Significant photothermal effect, enhanced biocompatibility, and great thermal stability were all exhibited by GO-PEG.

Interestingly, these photothermal structures alleviated the antitumor potentials of macrophages and mitigated the M2 polarization caused by interleukin-4. As a result, human cancer cells were incapable of migrating or invading, which led to appropriate antitumor effects [70]. Furthermore, in vitro, laser irradiation eliminated malignant cells when chitosan-functionalized GO nanoplatforms were coupled with folic acid for photothermal cancer therapy guided by NIR fluorescence and photoacoustic imaging [71]. Additionally, in vivo tests showed that within 20 days of the specific nanosystem being deployed under laser irradiation, the tumors were entirely blocked and could not recur [71]. To date, a number of GO-based systems have been investigated in an effort to produce a strong photothermal impact for cancer treatment [72]. Relying on the type of cancer being handled and cured, variables like the intensity and the length of external laser radiation, as well as the concentration and modification of the GBNMs, have been taken into account.

V. CHALLENGES AND PERSPECTIVES

5.1 Gold nanoparticles

To be considered optimal candidates for PTT, materials must meet specific criteria to avoid damage to surrounding normal cells, provide adequate photothermal effectiveness, and ensure sufficient penetration depth. The ideal PTT candidate should: (1) possess uniform shape and appropriate nano-range size; (2) interact with light in the NIR range of 650-950 nm; (3) exhibit excellent dispersion in aqueous solutions; (4) maintain sufficient photostability to ensure adequate diffusion time for tumor penetration before losing photosensitivity; and (5) demonstrate minimal or no cytotoxicity in living tissues [73].

While GNPs meet most of these criteria, their long-term cytotoxicity remains insufficiently characterized. Although GNPs are generally considered biocompatible, the long-term effects of nanoparticle accumulation are not fully understood. Preliminary research suggests several factors affecting GNP cytotoxicity, with size and surface charge identified as the most critical variables. Despite encouraging initial cytotoxicity studies, questions remain regarding whether GNPs are eventually cleared from the body and whether GNP accumulation might have long-term consequences [74].

Additionally, other technologies could render the use of GNPs obsolete, in addition to the fact that the biocompatibility problem around GNPs is still not fully resolved. For instance, using particular biodegradable polymer systems for PTT has become more popular. According to a recent study, a new polymer-based photothermal nanoagent that responds to light in the NIR-II spectrum (1,000–1,700 nm) can penetrate tissue significantly deeper than light in the NIR-I spectrum. Though the possible benefits of conjugating GNPs with NIR-II responsive polymers over employing pure NIR-II polymer nanoparticles have not yet been investigated, it should be mentioned that this is theoretically possible [75].

5.2 Graphene-based nanomaterials

Recent years have witnessed tremendous advancements in methods for biomedical applications of graphene nanoparticles. GO and rGO have been documented and accepted as promising photothermal agents in nanomedicine due to their excellent biocompatibility and physicochemical properties. However, several challenges must be addressed before nanoparticle-based photothermal therapy can be applied clinically, particularly for deeply embedded tumors or metastatic disease.

First, much research has focused on generating hyperthermia using laser light in the NIR-I window, primarily at 808 nm. While this wavelength is attractive due to minimal absorption by biological chromophores, its limited tissue penetration depth restricts its utility for treating large or deep tumors. This limitation is particularly crucial in clinical settings where PTT using GO as a photothermal agent would be ineffective. The NIR-II window offers a superior alternative, as longer wavelengths experience less scattering and penetrate deeper into tissues. Additionally, longer wavelengths carry less energy per photon, allowing higher power intensities to be employed. Therefore, researchers should consider the NIR-II region for radiation when developing new approaches for GBNMs-based photothermal cancer treatment. Additionally, because longer wavelengths carry less energy per photon, larger power intensities can be employed [76, 79]. Therefore, researchers should consider the NIR-II region for radiation when developing new methods for photothermally treating cancer utilizing GBNMs.

The possible risk to human health from GBNMs, modified GBNMs, and NIR irradiation is another important factor to consider when planning clinical trials. Several variables, such as GBNMs' size, chemical makeup, surface charge, and aggregation state, can affect how harmful they are [80]. It is crucial to remember that although GO and rGO have demonstrated excellent biocompatibility in several studies, their toxicity may increase due to subsequent functionalization.

Subsequently, it would be wise to prioritize biomimetic molecules -especially those approved by the FDA- in any future GBNM-based treatment approaches. While GBNMs are altered for combinatorial approaches or multimodal cancer detection and treatment, this emphasis becomes even more important [81]. Further studies involving the use of FDA-approved modified rGO, the use of NIR-II light sources for irradiation, the use of 3D tumor models for in vitro tests, and the evaluation of in vivo toxicity will be crucial in the future. This team effort will greatly aid the advancement of the shift from laboratory experiments to potential clinical implementations.

VI. CONCLUSIONS

Our comprehensive comparative analysis demonstrates that nanomaterials have fundamentally transformed photothermal cancer therapy, expanding its applications from localized tumor ablation to the treatment of metastatic disease. The novel head-to-head assessment of gold nanoparticles and graphene oxide, the two most extensively studied nanomaterials in this field, reveals their complementary advantages for cancer PTT, particularly for oral malignancies. This review uniquely identifies that gold nanorods offer precisely tunable optical properties through aspect ratio modification, achieving peak absorption in the NIR-I window (750-1000 nm) with exceptional photothermal conversion efficiency via localized surface plasmon resonance. Their established biocompatibility and ongoing clinical trials demonstrate the advanced translational status of gold-based

nanomaterials. Conversely, our analysis reveals that graphene oxide provides exceptional thermal conductivity, superior surface functionalization potential, and unique optical properties that enable multimodal imaging and therapy. Its two-dimensional structure offers an increased surface area for drug loading, making it particularly valuable for combination therapeutic approaches.

This review's novel contribution is identifying critical parameters for the successful clinical implementation of nanomaterial-enhanced PTT for oral cancer. Future research must prioritize: (1) standardized comparative studies between different nanosystems to establish optimal therapeutic protocols; (2) comprehensive biocompatibility assessments focusing on long-term toxicity profiles; (3) development of targeted delivery strategies to maximize tumor specificity while minimizing off-target effects; and (4) exploration of NIR-II window irradiation for deeper tissue penetration.

While preliminary clinical studies have demonstrated promising results, particularly for gold nanoparticles, our analysis identifies that broader clinical adoption requires resolving outstanding questions regarding long-term biocompatibility, biodistribution, and clearance mechanisms. Our novel finding is that integrating FDA-approved biomimetic molecules in nanoparticle functionalization represents a promising approach to accelerate regulatory approval and clinical translation.

Ultimately, this comparative assessment establishes that nanomaterial-enhanced photothermal therapy offers significant potential as a minimally invasive, highly selective treatment modality for oral cancers, particularly for patients who cannot tolerate conventional treatments or those with recurrent disease. The continued refinement of nanomaterial properties, irradiation parameters, and targeting strategies will be essential to fully realize the therapeutic potential of this approach and improve outcomes for patients with oral malignancies.

REFERENCES

1. Almangush A, Mäkitie AA, Triantafyllou A, et al. Staging and grading of oral squamous cell carcinoma: an update. Oral Oncol. 2020; 107:104799.
2. Kim HAJ, Zeng PYF, Shaikh MH, et al. All HPV-negative head and neck cancers are not the same: analysis of the TCGA dataset reveals that anatomical sites have distinct mutation, transcriptome, hypoxia, and tumor microenvironment profiles. Oral Oncol. 2021; 116:105260.
3. Deng H, et al. The treatment of oral cancer: an overview for dental professionals. Aust Dent J. 2011.
4. Pustylnikov S, et al. Targeting mitochondria in cancer: current concepts and immunotherapy approaches. Transl Res. 2018.
5. Elfeky SA, Qenawi N, Tawfik W, Loutfy SA, Subash TD. Utilization of Nanographene Oxide–Folic Acid–Metal Chalcogen in Cancer Theranostics. NanoWorld J. 2023;9(S5): S206-S214.
6. Cupino TL, et al. Stability and bioactivity of chitosan as a transfection agent in primary human cell cultures: a case for chitosan-only controls. Carbohydr Polym. 2018.
7. Tawfik W. A strategic review of the impact of modern technologies on scientific research: AI, lasers, and nanotechnology. J Laser Sci Appl. 2024;1(2):38-48.
8. Gamal H, Tawfik W, Fahmy HM, El-Sayyad HH. Breakthroughs of using photodynamic therapy and gold nanoparticles in cancer treatment. In: 2021 IEEE International Conference on Nanoelectronics, Nanophotonics, Nanomaterials, Nanobioscience & Nanotechnology (5NANO). IEEE; 2021. p. 1-4.
9. Gai S, Yang G, Yang P, et al. Recent advances in functional nanomaterials for light–triggered cancer therapy. Nano Today. 2018; 19:146-87. doi:10.1016/j.nantod.2018.02.010.
10. Liu P, Ye M, Wu Y, Wu L, Lan K, Wu Z. Hyperthermia combined with immune checkpoint inhibitor therapy: synergistic sensitization and clinical outcomes. Cancer Med. 2023; 12:3201-21.
11. Dickerson EB, Dreaden EC, Huang XH, El-Sayed IH, Chu HH, Pushpanketh S, et al. Gold nanorod assisted near-infrared plasmonic photothermal therapy (PPTT) of squamous cell carcinoma in mice. Cancer Lett. 2008;269(1):57-66. doi:10.1016/j.canlet.2008.04.026.
12. Bhaskar S, Ganesh KM, Arora D, Gupta Y, Maddala BG, Bonyár A, et al. Nanoengineering at functional plasmonic interfaces. In: Nano-Engineering at Functional Interfaces for Multi-Disciplinary Applications. Elsevier; 2025. p. 47-73.
13. Karthikeyan L, Sobhana S, Yasothamani V, Gowsalya K, Vivek R. Multifunctional theranostic nanomedicines for cancer treatment: recent progress and challenges. Biomed Eng Adv. 2023; 5:100082.
14. Gao S, Yang X, Xu J, Qiu N, Zhai G. Nanotechnology for boosting cancer immunotherapy and remodeling tumor microenvironment: the horizons in cancer treatment. ACS Nano. 2021; 15:12567-603.
15. Yang F, He Q, Dai X, Zhang X, Song D. The potential role of nanomedicine in the treatment of breast cancer to overcome the obstacles of current therapies. Front Pharmacol. 2023; 14:1-12.
16. Gamal H, Tawfik W, El-Sayyad HI, Emam AN, Fahmy HM, El-Ghaweet HA. A new vision of photothermal therapy assisted with gold nanorods for the treatment of mammary cancers in adult female rats. Nanoscale Adv. 2024;6(1):170-87.
17. Qenawi N, Tawfik W, Abd-El Aziz AM, ElFeky SA. Innovative graphene oxide-folic acid-MoS2 nanocomposite for targeted near-infrared photothermal cancer therapy. Egypt J Chem. 2025.
18. Gupta N, Malviya R. Understanding and advancement in gold nanoparticle targeted photothermal therapy of cancer. Biochim Biophys Acta Rev Cancer. 2021; 1875:188532.
19. Oh J, Yoon H, Park JH. Nanoparticle platforms for combined photothermal and photodynamic therapy. Biomed Eng Lett. 2013;3(2):67-73. doi:10.1007/s13534-013-0097-8.
20. Nasseri B, Alizadeh E, Bani F, et al. Nanomaterials for photothermal and photodynamic cancer therapy. Appl Phys Rev. 2022; 9:011317.
21. Jassim JM, Al-samak MS, Younes WT, Kisov H. Near-infrared plasmonic random laser emission employing gold nanorods and LDS-821 dye. Plasmonics. 2025:1-8.

22. Wang Y, Meng H-M, Song G, Li Z, Zhang X-B. Conjugated-polymer-based nanomaterials for photothermal therapy. ACS Appl Polym Mater. 2020; 2:4258-72.
23. Chen J, Ye Z, Yang F, Yin Y. Plasmonic nanostructures for photothermal conversion. Small Sci. 2021; 1:2000055.
24. Guo T, Tang Q, Guo Y, et al. Boron quantum dots for photoacoustic imaging-guided photothermal therapy. ACS Appl Mater Interfaces. 2021; 13:306-11.
25. McCarthy B, Cudykier A, Singh R, Levi-Polyachenko N, Soker S. Semiconducting polymer nanoparticles for photothermal ablation of colorectal cancer organoids. Sci Rep. 2021; 11:1532.
26. Li Y, Bai G, Zeng S, Hao J. Theranostic carbon dots with innovative NIR-II emission for in vivo renal-excreted optical imaging and photothermal therapy. ACS Appl Mater Interfaces. 2019; 11:4737-44.
27. Chen YS, Zhao Y, Yoon SJ, Gambhir SS, Emelianov S. Miniature gold nanorods for photoacoustic molecular imaging in the second near-infrared optical window. Nat Nanotechnol. 2019; 14:465-72.
28. Huang X, El-Sayed MA. Gold nanoparticles: optical properties and implementations in cancer diagnosis and photothermal therapy. J Adv Res. 2010; 1:13-28.
29. Kadkhoda J, Aghanejad A, Safari B, Barar J, Rasta SH, Davaran S. Aptamer-conjugated gold nanoparticles for targeted paclitaxel delivery and photothermal therapy in breast cancer. J Drug Deliv Sci Technol. 2022; 67:102954.
30. Hori K, Higashida S, Osaki T, et al. Intracellular delivery and photothermal therapeutic effects of polyhistidine peptide-modified gold nanoparticles. J Biotechnol. 2022; 354:34-44.
31. Jain PK, El-Sayed MA. Plasmonic coupling in noble metal nanostructures. Chem Phys Lett. 2010; 487:153-64.
32. Jain PK, Lee KS, El-Sayed IH, El-Sayed MA. Calculated absorption and scattering properties of gold nanoparticles of different size, shape, and composition: applications in biological imaging and biomedicine. J Phys Chem B. 2006; 110:7238-48.
33. Prescott SW, Mulvaney P. Gold nanorod extinction spectra. J Appl Phys. 2006; 99:123504.
34. Bardhan R, Lal S, Joshi A, Halas NJ. Theranostic nanoshells: from probe design to imaging and treatment of cancer. Acc Chem Res. 2011; 44:936-46.
35. Radwan NA, Tawfik W, Atta D, Ageba MF, Salama SN, Mohamed MN. A new approach in investigation the chemotaxis response of mammalian parasitic nematode: in vitro study. J Exp Zool A Ecol Integr Physiol. 2025.
36. Allam A, Tawfik W, Abo-Elfadl MT, Fahmy AM, Elfeky SA. Photoactive folic acid nanocomposite for targeted PDT of breast and liver cancer cell lines. Egypt J Chem. 2025.
37. Harris-Birtill D, Singh M, Zhou Y, et al. Gold nanorod reshaping in vitro and in vivo using a continuous wave laser. PLoS ONE. 2017;12: e0185990.
38. Gentili D, Ori G, Comes Franchini M. Double phase transfer of gold nanorods for surface functionalization and entrapment into PEG-based nanocarriers. Chem Commun (Camb). 2009; 39:5874-6.
39. Kang X, Guo X, Niu X, et al. Photothermal therapeutic application of gold nanorods-porphyrin-trastuzumab complexes in HER2-positive breast cancer. Sci Rep. 2017; 7:42069.
40. Rastinehad AR, Anastos H, Wajswol E, et al. Gold nanoshell-localized photothermal ablation of prostate tumors in a clinical pilot device study. Proc Natl Acad Sci U S A. 2019; 116:18590-6.
41. Kharlamov AN, Tyurnina AE, Veselova VS, Kovtun OP, Shur VY, Gabinsky JL. Silica-gold nanoparticles for atheroprotective management of plaques: results of the NANOM-FIM trial. Nanoscale. 2015; 7:8003-15.
42. Itoo AM, Vemula SL, Gupta MT, Giram MV, Kumar SA, Ghosh B, et al. Multifunctional graphene oxide nanoparticles for drug delivery in cancer. J Control Release. 2022; 350:26-59.
43. Qi K, Sun B, Liu S, Zhang M. Research progress on carbon materials in tumor photothermal therapy. Biomed Pharmacother. 2023; 165:115070.
44. Tarcan R, Todor-Boer O, Petrovai I, Leordean C, Astilean S, Botiz I. Reduced graphene oxide today. J Mater Chem C. 2020; 8:1198-224.
45. Liu J, Dong J, Zhang T, Peng Q. Graphene-based nanomaterials and their potentials in advanced drug delivery and cancer therapy. J Control Release. 2018; 286:64-73.
46. Hummers WS, Offeman RE. Preparation of graphitic oxide. J Am Chem Soc. 1958; 80:1339.
47. De Melo-Diogo D, Lima-Sousa R, Alves CG, Costa EC, Louro RO, Correia IJ. Functionalization of graphene family nanomaterials for application in cancer therapy. Colloids Surf B Biointerfaces. 2018; 171:260-75.
48. Karlický F, Kumara Ramanatha Datta K, Otyepka M, Zbořil R. Halogenated graphenes: rapidly growing family of graphene derivatives. ACS Nano. 2013;7(8):6434-64. doi:10.1021/nn4024027.
49. Yang HW, Lu YJ, Lin KJ, Hsu SC, Huang CY, She SH, et al. EGRF conjugated PEGylated nanographene oxide for targeted chemotherapy and photothermal therapy. Biomaterials. 2013;34(29):7204-14. doi:10.1016/j.biomaterials.2013.06.007.
50. Song E, Han W, Li C, Cheng D, Li L, Liu L, et al. Hyaluronic acid-decorated graphene oxide nanohybrids as nanocarriers for targeted and pH-responsive anticancer drug delivery. ACS Appl Mater Interfaces. 2014;6(15):11882-90. doi:10.1021/am502423r.
51. Miyanda PM, Gautam S. Graphene oxide: a potential drug carrier for cancer therapy—review. Res Rev J Pharm Sci. 2017;8(3):21-31.
52. Wu SY, An SS, Hulme J. Current applications of graphene oxide in nanomedicine. Int J Nanomedicine. 2015; 10:9-24. doi:10.2147/IJN.S88285.
53. Bai H, Li C, Shi G. Functional composite materials based on chemically converted graphene. Adv Mater. 2011;23(9):1089-115. doi:10.1002/adma.201003753.
54. Marcano DC, Kosynkin DV, Berlin JM, Sinitskii A, Sun Z, Slesarev A, et al. Improved synthesis of graphene oxide. ACS Nano. 2010;4(8):4806-14. doi:10.1021/nn1006368.
55. Lin J, Chen X, Huang P. Graphene-based nanomaterials for bioimaging. Adv Drug Deliv Rev. 2016; 105:242-54. doi:10.1016/j.addr.2016.05.013.
56. Rosenthal A, Mantz A, Nguyen A, Bittrich E, Schubert E, Schubert M, et al. Biofunctionalization of titanium substrates using nanoscale polymer brushes with cell

adhesion peptides. J Phys Chem B. 2018;122(25):6543-50. doi:10.1021/acs.jpcb.8b02407.
57. Chen L, Wang Y, Song J, Deng W, Lu J, Ma L, et al. Phosphoproteome-based kinase activity profiling reveals the critical role of MAP2K2 and PLK1 in neuronal autophagy. Autophagy. 2017;13(11):1969-80. doi:10.1080/15548627.2017.1371393.
58. Rao Z, Ge H, Liu L, Zhu C, Min L, Liu M, et al. Carboxymethyl cellulose modified graphene oxide as pH-sensitive drug delivery system. Int J Biol Macromol. 2018; 107:1184-92. doi:10.1016/j.ijbiomac.2017.09.096.
59. Ege D, Kamali A, Boccaccini A. Graphene oxide/polymer-based biomaterials. Adv Eng Mater. 2017; 19:1700627. doi:10.1002/adem.201700627.
60. Zhao X, Wei Z, Zhao Z, Miao Y, Qiu Y, Yang W, et al. Design and development of graphene oxide nanoparticle/chitosan hybrids showing pH-sensitive surface charge-reversible ability for efficient intracellular doxorubicin delivery. ACS Appl Mater Interfaces. 2018;10(7):6608-17. doi:10.1021/acsami.7b16910.
61. Alibolandi M, Mohammadi M, Taghdisi SM, Ramezani M, Abnous K. Fabrication of aptamer decorated dextran coated nano-graphene oxide for targeted drug delivery. Carbohydr Polym. 2017; 155:218-29. doi:10.1016/j.carbpol.2016.08.046.
62. Georgakilas V, Otyepka M, Bourlinos AB, Chandra V, Kim N, Kemp KC, et al. Functionalization of graphene: covalent and noncovalent approaches, derivatives and applications. Chem Rev. 2012;112(11):6156-214. doi:10.1021/cr3000412.
63. Chua CK, Pumera M. Covalent chemistry on graphene. Chem Soc Rev. 2013;42(8):3222-33. doi:10.1039/c2cs35474h.
64. Zhang B, Wang Y, Liu J, Zhai G. Recent developments of phototherapy based on graphene family nanomaterials. Curr Med Chem. 2017;24(3):268-91. doi:10.2174/0929867323666161019141817.
65. Britnell L, Ribeiro RM, Eckmann A, Jalil R, Belle BD, Mishchenko A, et al. Science. 2013; 340:1311-4.
66. Grigorenko AN, Polini M, Novoselov KS. Nat Photonics. 2012; 6:749.
67. Bao Q, Zhang H, Wang Y, Ni Z, Yan Y, Shen ZX, et al. Adv Funct Mater. 2009; 19:3077-83.
68. Gong P, Ji S, Wang J, Dai D, Wang F, Tian M. Fluorescence-switchable ultrasmall fluorinated graphene oxide with high near-infrared absorption for controlled and targeted drug delivery. Chem Eng J. 2018; 348:438-46. doi:10.1016/j.cej.2018.04.193.
69. Kalluru P, Vankayala R, Chiang CS, Hwang KC. Nano-graphene oxide-mediated in vivo fluorescence imaging and bimodal photodynamic and photothermal destruction of tumors. Biomaterials. 2016; 95:1-10. doi:10.1016/j.biomaterials.2016.04.006.
70. Deng X, Liang H, Yang W, Shao Z. Polarization and function of tumor-associated macrophages mediate graphene oxide-induced photothermal cancer therapy. J Photochem Photobiol B. 2020; 208:111913.
71. Jun SW, Manivasagan P, Kwon J, et al. Folic acid–conjugated chitosan-functionalized graphene oxide for highly efficient photoacoustic imaging-guided tumor-targeted photothermal therapy. Int J Biol Macromol. 2020; 155:961-71.
72. Qi K, Sun B, Liu S, Zhang M. Research progress on carbon materials in tumor photothermal therapy. Biomed Pharmacother. 2023; 165:115070.
73. Zhou J, Lu Z, Zhu X, Wang X, Liao Y, Ma Z, et al. NIR photothermal therapy using polyaniline nanoparticles. Biomaterials. 2013; 34:9584-92. doi:10.1016/j.biomaterials.2013.08.075.
74. Balogh L, Nigavekar SS, Nair BM, Lesniak W, Zhang C, Sung LY, et al. Significant effect of size on the in vivo biodistribution of gold composite nanodevices in mouse tumor models. Nanomedicine (Lond). 2007; 3:281-96. doi:10.1016/j.nano.2007.09.001.
75. Sun T, Dou J-H, Liu S, Wang X, Zheng X, Wang Y, et al. Second near-infrared conjugated polymer nanoparticles for photoacoustic imaging and photothermal therapy. ACS Appl Mater Interfaces. 2018; 10:7919-26. doi:10.1021/acsami.8b01458.
76. Zhang L, Oudeng G, Wen F, Liao G. Recent advances in near-infrared-II hollow nanoplatforms for photothermal-based cancer treatment. Biomater Res. 2022; 26:61.
77. Liu P, Ye M, Wu Y, Wu L, Lan K, Wu Z. Hyperthermia combined with immune checkpoint inhibitor therapy: synergistic sensitization and clinical outcomes. Cancer Med. 2023; 12:3201-21.
78. Xu C, Pu K. Second near-infrared photothermal materials for combinational nanotheranostics. Chem Soc Rev. 2021; 50:1111-37.
79. Kang W, Liu Y, Wang W. Light-responsive nanomedicine for cancer immunotherapy. Acta Pharm Sin B. 2023; 13:2346-68.
80. Karthikeyan L, Sobhana S, Yasothamani V, Gowsalya K, Vivek R. Multifunctional theranostic nanomedicines for cancer treatment: recent progress and challenges. Biomed Eng Adv. 2023; 5:100082.
81. Zhang Y, Li J, Pu K. Recent advances in dual- and multi-responsive nanomedicines for precision cancer therapy. Biomaterials. 2022; 291:121906.

NILES

Journal of Laser Science and Applications
journal homepage: https://jlsa.journals.ekb.eg

Cairo University

Corneal Ablation by 266-nm and 193-nm Lasers: A comprehensive Chemical Analysis Study Assisted with Machine Learning

Ibrahim Abdelhalim[a], Omnia Hamdy[a,*], Aziza Ahmed Hassan[b], Salwa Abdelkawi[c], Salah Hassab Elnaby[a] and

[a] Engineering Applications of Laser Department , National Institute of Laser Enhanced Sciences, Cairo University, Giza, 12613, Egypt.

[b] Medical Applications of Laser Department, National Institute of Laser Enhanced Sciences, Cairo University, , Giza, 12613, Egypt.

[c] Vision Science Department, Research Institute of Ophthalmology, Biophysics and Laser Science Unit, , Giza, Egypt

Abstract

Background: Laser-assisted in situ keratomileusis (LASIK) is a widely used refractive surgical procedure that typically involves the ablation of the corneal stroma using 193 nm excimer laser pulses. While this method is effective in reshaping the cornea, alternative laser sources such as nanosecond Q-switched solid-state lasers at 266 nm (fourth harmonic of Nd:YAG) offer potential benefits, particularly regarding their influence on the chemical integrity of ablated tissue.

Objective: This study aims to compare the chemical outcomes of corneal ablation using 193 nm excimer laser and 266 nm Qswitched laser pulses.

Methods: Using Fourier Transform Infrared (FTIR) spectroscopy, we investigate the molecular composition and bonding differences in the treated tissue. Additionally, machine learning algorithms are employed to support spectral analysis and enhance the interpretation of chemical changes induced by each laser source.

Results: The experimental FTIR results reveal distinct chemical differences between the two ablation techniques. Although the 266 nm Q-switched laser exhibits slightly lower ablation rates, it demonstrates favorable chemical effects on the tissue structure.

Conclusion: These findings, reinforced by machine learning analysis, contribute to a more comprehensive understanding of how laser parameters influence the biochemical outcomes of corneal ablation

Keywords: LASIK; Machine learning; corneal ablation; excimer laser; FTIR

I. Introduction

The cornea is the primary refractive element in the eye. It comprises five layers: the stroma, the Descemet membrane, the epithelium, Bowman's layer, and the endothelium [1]. The majority of the cornea's dry weight is made up of about two hundred layers of stroma which are primarily made of type I collagen fibrils [2]. Three amino acid chains that wind around one another to form a triple helix make up the unique structure of native collagen [3]. The primary components of the cornea are water and collagen. Collagen I, which makes up 78% of the corneal stroma, is the main type of collagen. Collagen III, IV, and V, as well as keratan sulfate and other trace amounts, make up around 7%. Proteoglycans are intricate molecules made of sugar chains and proteins that support the integrity of the cornea's moisture and clarity [4].

Collagen molecules can produce two different kinds of hydrogen bonds; the first kind is formed between the CAO or NOH groups that are between water molecules, and the other is developed between the NOH and CAO groups in neighboring chains to generate interchain hydrogen bonds [5]. According to X-ray diffraction assessments, bovine corneas contain at least 66% water [6]. The water molecules and the CAO and NOH groups in polypeptide chains exhibit two different kinds of hydrogen bonding. As a result, several kinds of hydrogen-bonded OOH peaks in the 3300–3600 cm^{-1} range of the IR spectrum can be expected [7]. Both the hydrogen-bound OOH stretching vibration and the nonhydrogen bonded (free) NOH stretching vibration (about 3450 cm^{-1}) are correlated with many peaks in the region of 3400 to 3600 cm^{-1}. The peak at 3316 cm^{-1} may represent the NOH stretching vibration. The nonhydrogen bonded (free) OOH stretching vibration band is represented by the strong peak at 3572 cm^{-1}. Additionally, vibrations of the carbonyl group (CAO) and typical amide I are detected at 1549 and 1651 cm^{-1} respectively [8].

By directing radiation in the infrared region that is absorbed by the sample, FTIR spectroscopy offers an appropriate method to investigate the structure of ocular proteins. Infrared absorption bands are unique to each sample.

Corresponding Author: Omnia Hamdy Email: omnia@niles.cu.edu.eg

Received April 4, 2025 Revised date: June 6, 2025 Accepted June 13, 2025

ISSN: 1687-8892

Amide I and Amide II are the most recognizable bands in the infrared spectra of corneal proteins and polypeptides [9].
FTIR can identify shifting distinctive absorption lines that are indicative of changes in protein structure. All nearby atoms and bonds are interacting to cause this shift. Quantum theory of molecular vibrations can be used to compute these shifts. Additionally, IR spectral datasets are widely available [10]. In the present study, we made use of a condensed set that has been published in Merck [11], [12]. Amide I, amide II, and amide III bands are the most prominent in the protein IR spectrum [9]. The amide I band (1600-1700 cm^{-1}) namely (1633.6, 1528, 1431.2, 1224, 1171.6, 1083.6 cm^{-1}) is caused by the carbonyl stretching vibration of the amide groups with some contribution from the C-N stretch. On the other hand, the amide II band (1510-1580 cm-1) specifically (1704, 1431, 1110, 1022 cm^{-1}) is sensitive to secondary structure conformation. While, Amide III (1200-1350 cm-1) namely (1602.8, 1501.6, 1180, 1050 cm-1) is a complicated band resulting from secondary structures [6].

These infrared bands are sensitive to hydrogen bonding, dipole–dipole interactions, and the peptide backbone geometry, making them well-established markers of the secondary structural change. Curve fitting identifies the amide I band, which is one of the secondary structure's primary components (helix at 1650-1658 cm^{-1} and sheet at 1620-1640 cm^{-1}). These bands have long been used to assess proteins' denaturation responses [13].

Recently, spectral identification has been found to be effectively aided by machine learning [14]. IR spectroscopy's primary purpose of delivering quick, preliminary information on molecules under study is well-aligned with the use of machine learning algorithms to aid in the interpretation of IR data. However, because of the greater complexity and variety of the vibrational spectra in these states, the model performs inferior on the infrared data acquired from organic molecules in the liquid and solid physical states. Furthermore, due to intermolecular interactions brought on by molecules' near proximity, vibrational spectra can be more complex in the liquid and solid phases [15].

In the present study, we aim to experimentally investigate and compare the chemical modifications in corneal tissue resulting from laser ablation using two distinct wavelengths; 193 nm excimer laser and the fourth harmonic of Nd:YAG 266 nm Q-switched solid-state laser. Building on earlier numerical predictions suggesting potential differences in post-ablation chemical composition, we employ Fourier Transform Infrared (FTIR) spectroscopy to analyze molecular alterations induced by each technique. Special attention is given to identifying variations in functional groups and bonding patterns within the treated tissue. To support a more refined interpretation of the spectral data, a machine learning model is applied, offering an advanced analytical approach to discern subtle chemical distinctions between the two methods. This comprehensive analysis seeks to bridge the gap between ablation efficiency and chemical outcome, contributing to a deeper understanding of how different laser sources influence the biochemical integrity of the cornea.

II. METHODS

A. Sample preparation

Ex-vivo rabbit eyes were purchased from a local butcher shop (Three rabbits, i.e. six corneas were employed) and transported to our lab in sterile containers within one hour after slaughter and transported in sterile containers filled with phosphate-buffered saline (PBS) to maintain hydration. To minimize variability, samples were held at 4°C on arrival and processed within 2 hours. Hydration levels were standardized by blotting surplus fluid using sterile filter paper prior to laser ablation. This methodology guarantees consistency in the O-H/N-H spectrum areas (3300-3600 cm^{-1}), as proven by pre-ablation FTIR baseline measurements. To assess the laser's ability to ablate the stroma, 7.5 mm of mechanical epithelial debridement was performed in the central region of the cornea. The samples were then exposed to 100 pulses of each laser type (i.e. 266 nm and 193 nm) at 20 distinct places. Consequently, the surface of the cornea was subjected to total 2000 laser pulses. Even though the overall pulse count of 2000 might seem excessive, it is consistent with modern LASIK procedures. Contemporary excimer lasers may produce more than 20,000 pulses in 20 seconds at frequency higher than 1000 Hz. For experimental precision, our pulse count represents a cautious estimate.

The excimer laser at 193-nm laser has a power of 1 mJ, spot size of 0.7 mm, and pulse duration of 4-7 ns. While, the Q-switched solid-state laser ((266 nm) has 1mJ power, 0.5 mm spot size, and 3-5 ns pulse duration. For the FTIR examination, the laser-ablated corneas were immediately inserted into liquid nitrogen (–196 ºC) to completely lyophilize them. After that, a Teflon hand homogenizer was used to dissolve the corneas into a powder to extract the proteins. Finally, potassium bromide (KBr) powder (98 mg KBr: 2 mg of powdered cornea) was combined with the acquired corneal powder to create the KBr disks. A Thermo Nicolet iS5 FTIR spectrometer (USA) was employed to obtain FTIR spectra in the 4000–1000 cm^{-1} range. The spectrometer was operated under continuous dry nitrogen gas and baseline adjusted.

B. Spectral Lines

The spectral peaks are detected at the local maxima of the curve. Additionally, there are kinks that indicate hidden maxima which are buried in the total spectra. To justify the set of collected lines, we reproduced the spectra assuming the lines are Gaussian function of wavenumber with an average line width of 30 cm^{-1} as can be seen in the theoretical study of [16]. For each line there is an amplitude *A(i)* where i=1, 2,.. , n, where n is the number of lines in the spectra. The measured value of the spectra at a spectral line *L(j)* is the sum of all Gaussian lines at that particular wavenumber *L* (j) so,

$$L(j) = \sum_{i=1}^{n} A(i)\exp\left(-\left(\frac{\nu_i - \nu_j}{30}\right)^2\right) \quad (1)$$

Accordingly, we get n equations in n variables that can be easily solved to get the values of *A(j)*. Using curve fitting we can justify all the set of spectral lines.

C. Spectral Analysis

Using the published databases [11], [16] we can assign a bond vibrational mode to each spectral line. Then, using the databases of functional groups, we can assign one or more

function group to each spectral line. To find more reliable assignment, the function group database sorted by functional groups (i.e. each function group has a finite number of several lines) has been used. Consequently, the functional groups which does not have all or most of the spectral lines were removed.

D. Machine Learning

A three-step technique was used to implement spectral processing in Python (version 3.9.7). The first part of the algortim finds spectral lines that are poorly resolved or overlapped. Closely spaced peaks are sometimes shown as a single wide line with inflections or kinks. The program uses the Least Squares Method (LSM) to deconvolute these composite lines, properly calculate the positions of individual spectral peaks, and create a comprehensive list of discovered lines. Gaussian deconvolution (scipy.optimize.curve_fit) with a 1.5% root-mean-square error tolerance was used to resolve overlapping peaks. In the second stage, the software uses the built-in spectral database of functional groups. It validates the previously identified spectral lines against this database. A functional group is considered present if all of its characteristic spectral lines can be recognized. This stage assures specificity while reducing false positives. all characteristic peaks had to be detected in order to identify functional groupings by stringent matching against a proprietary database (in JSON format). The third step calculates the relative abundance (weight) of each recognized functional group using the intensity of its characteristic peaks. A simulated spectrum is then generated, and the software iteratively adjusts the weights to reduce the difference between the reconstructed and measured spectra. Again, the divergence did not surpass 1.5%, demonstrating the model's robustness. The reconstructed spectra were verified against the original data, and relative abundances were computed using MinMax normalization of peak intensities. The steps of the implemented algorithm are summarized in the flowchart presented in Fig. 1.

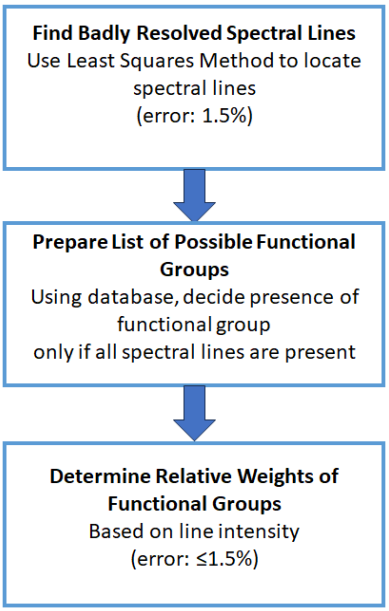

Fig. 1 Flowchart illustrating the main components of the proposed self-deciding algorithm for spectral analysis.

E. Statistical Analysis

A pairwise comparison weas carried out in order to evaluate any potentially notable variations in FTIR absorbance values between the experimental groups. Since there was no assumption of normality in the data distribution and the sample sizes were quite modest, non-parametric Mann-Whitney U tests were used for all comparisons [17]. Ordinal data or data that do not satisfy parametric assumptions, such those frequently seen in spectroscopic measurements, are appropriate for this strong statistical test. In particular, pairwise comparisons between Control and L193, Control and L266, and L193 and L266 were carried out. A predefined significance level (α) of 0.05 was used for all statistical analyses. All statistical calculations were carried out using Python (version 3.9.7), utilizing well-known libraries including SciPy for specialized statistical functions and NumPy for numerical operations.

III. RESULTS

The measured spectra of the control tissue (i.e. un-irradiated cornea), the tissue remaining after ablation by excimer laser at 193 nm, and the tissue remaining after ablation by fourth harmonic of Nd-YAG laser at 266 nm is presented in Fig. 2

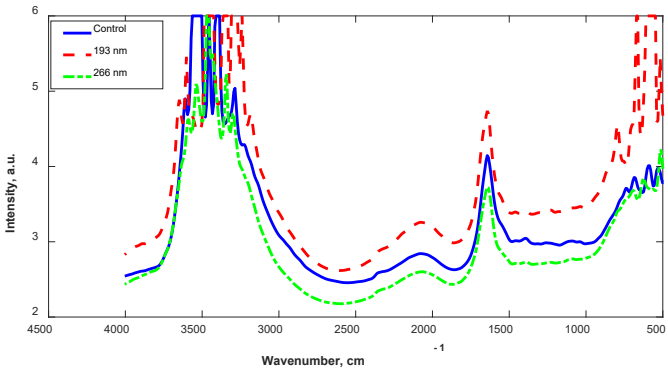

Fig. 2 Originally measured FTIR spectra. Control is solid line, ablated by excimer dashed line and ablated by fourth harmonic of Nd-YAG is represented by dash point line.

Some peaks of the spectra were limited to absorption value of 6. To be able to study the spectra mathematically we used a curve fitting program to complete the spectra. The corrected spectra is shown in Fig. 3

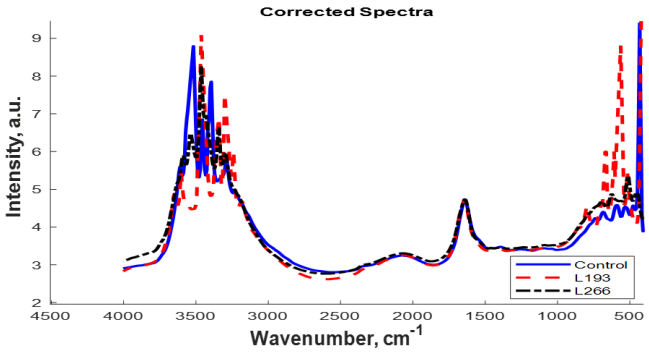

Fig. 3 The reproduced FTIR spectra after utilizing curve fitting.

A well-known method to identify spectral lines in a measured spectrum is to differentiate the spectrum. The 1st derivative of the spectrum will find the exact position of local maxima. To complete the finding we must use the second derivative to find other lines that produce kinks in the spectrum. Using a proprietary algorithm for identification of spectral lines and their strength we get about 70 lines in the region 400-4000 cm^{-1}. Many of these lines cannot be identified by simple observations. With human help can produce a closer identification of the spectral lines which when added should reproduce the measured spectrum. Since the spectra had very smooth intervals, we divided the spectra into 3 regions 500 – 1030 cm^{-1}, 1380 – 1700 cm^{-1}, and 3170 – 4000 cm^{-1}. We concentrate on these ranges. Using the above-mentioned methods, we could determine 70 of the important spectral lines and their corresponding strengths. Seventy spectral lines were resolved by the proposed algorithm (compared to fifty-two manually detected), including buried peaks in Amide I/II areas (Fig. 2). The functional group designations matched published collagen spectra 100 percent of the time [13], and simulated spectra replicated experimental data 98.5% of the time (MSE =.0015). By imposing physical limitations (e.g., fixed linewidths, stringent group rules), our deterministic method provides great precision with limited data, in contrast to CNNs that require massive training sets [14]. For corneal FTIR, where sample sizes are tiny and peak overlaps are frequent, this is crucial.

IV. DISCUSSION

The most characteristic bands found in the infrared spectra of corneal proteins and polypeptides are Amide I and Amide II. These ascend from the amide bonds that link the amino acids. The absorption related to the Amide I band leads to stretching vibrations of the C = O bond of the amide, and absorption related to the Amide II band leads primarily to bending vibrations of the N–H bond. Both C = O and the N–H bonds are involved in the hydrogen bonding between these two different elements of the secondary structure.

Published work for FTIR spectrum interpretation with the help of machine learning algorithms dealt with Convolutional Neural Networks as assignment problems. We shall adopt another technique based on minimizing a loss function for each group. The loss function is calculated as the sum of differences between the values mentioned in the databases and that present in the spectra. We used this approach to treat the spectral shift that may happen due to the spectrometer (constant shift error) and the shift of peaks due to interactions of other atoms in the molecular structure (variable shift error). We used Python algorithms for identification of functional groups.

We observed there are common lines in all spectra. These are bonds that have been preserved from the original stroma after ablation by either the 193 nm laser or the 266 nm. These correspond to unchanged structures. There are 29 out of total 70 identified lines as shown in Table 1. In all tables there are lines that can be assigned to more than one bond due to overlapping. We used the machine learning algorithms to identify functional groups as in the next section. Mainly the broad band at ~2100 cm^{-1} and the band at 1650 cm^{-1} conserve their strength, some O-H stretching and N-H of primary amine are left unchanged as in the table. Peak assignments for overlapping bands (e.g., 1650 cm^{-1} for Amide I vs. C=C) were cross-referenced with the Merck FTIR database [11] and validated against Baronio & Barth (2020) [13], which provides DFT-calculated vibrational modes for collagen. In the following we use the abbreviation L193 (cornea ablated by laser at wavelength 193nm), L266 (cornea ablated by laser at wavelength 266nm) and Control for the untreated cornea.

Table 1 Lines in common in the control, ablated by 193 nm laser and by the fourth harmonic of Nd:YAG (266 nm)

CONTROL		**L193**		**L266**		**Bond**	**Compound**	**Bond**	**Compound**
CM^{-1}	VAL	CM^{-1}	VAL	CM^{-1}	VAL				
3934.1	2.5	3926.4	2.7	3934.1	3.1				
3733.5	3.3	3748.9	3.1	3741.2	3.6				
3610.1	5.4	3602.4	5.0	3633.2	4.2	O-H stretch	alcohol		
3540.7	3.0	3548.4	3.8	3533.0	6.4	N-H stretch	Amine	O-H stretch	Alcohol
3448.1	5.3	3463.5	7.7	3455.8	6.7	O-H stretch	Alcohol		
3417.2	4.2	3425.0	5.2	3425.0	4.3	N-H	Amine	O-H stretch	Alcohol
3386.4	5.9	3371.0	5.4	3394.1	4.9	N-H	primary Amine	O-H stretch	Alcohol
3324.7	5.1	3332.4	4.2	3340.1	6.3	N-H	primary Amine	N-H	Amine
3278.4	5.3	3270.7	3.6	3286.1	3.7	C-H	Alkene	O-H stretch	Alcohol
3216.7	4.7	3239.8	5.2	3232.1	4.8	O-H stretch	Carboxylic Acid	O-H stretch	Alcohol
3124.1	4.0	3139.5	3.7	3155.0	3.6	O-H stretch	Carboxylic Acid		

3070.1	3.8	3085.5	3.7	3070.1	3.7	O-H stretch	Carboxylic Acid		
2962.1	3.3	2962.1	3.2	2923.6	3.2	C-H stretch	Alkene	O-H	Acid
2854.1	3.1	2838.7	2.9	2854.1	3.0	C-H stretch	Alkene	O-H	Acid
2645.9	2.3	2653.6	2.6	2645.9	2.8	O-H	Acid		
2615.0	2.3	2545.6	2.6	2553.3	2.8	O-H	Acid		
2414.4	2.8	2422.2	2.7	2429.9	2.9				
2321.9	2.1	2321.9	2.9	2314.2	2.5				
2221.6	3.1	2260.2	3.0	2244.7	3.0	C N trible	Nitrile		
2136.7	3.2	2183.0	3.1	2198.5	3.1	C C trible	Alkene		
2075.0	3.2	2067.3	3.0	2067.3	3.3	C C trible	Alkene		
1974.8	2.9	1982.5	3.1	1951.6	3.2	C C trible	Alkene		
1666.2	3.3	1666.2	4.0	1643.1	3.5	C=C	Alkene	Amide	
1612.2	3.7	1627.6	3.9	1619.9	3.0	C=C	Alkene		
1450.2	3.4	1450.2	2.8	1450.2	3.4	C-H bending	Alkane		
1380.8	2.1	1380.8	3.2	1388.5	2.1	C-H bending	Alkane		
1249.6	2.9	1295.9	3.3	1234.2	2.1	C-N	Amine,Amide		
1218.8	2.1	1218.8	2.5	1218.8	2.0	C-N	Amine,Amide	C-O	Alcohols
1187.9	2.9	1180.2	3.2	1164.8	3.4	C-N	Amine,Amide	C-O	Alcohols
771.4	3.7	786.8	4.1	786.8	4.2	C-H bending	1,2,4-trisubstituted		
732.8	3.8	748.2	3.5	732.8	4.1	C-H bending	1,2,4-trisubstituted		
686.5	3.3	702.0	3.9	694.2	4.3	C-H bending	1,2,4-trisubstituted		
671.1	1.2	663.4	5.6	678.8	4.6				
516.8	2.5	516.8	5.4	509.1	5.2				
470.5	3.6	470.5	4.0	455.1	3.6				

In addition to data presented on Table 1, there were 10 lines in common between the control and stroma ablated by 193nm laser as shown in Table 2, while in the case of ablation by the fourth harmonic of Nd:YAG (266 nm) there are 12 lines left unchanged as shown in Table 3. This increases the resemblance of these tissues with the control vis-à-vis that ablated by 193 nm laser.

Table 2 Common lines between control tissue and that ablated by 193 nm laser.

CONTROL		**L193**		**Bond**	**Compound**	**Bond**	**Compound**
CM-1	VAL	CM-1	VAL				
3826.1	3.0	3887.8	2.6				
3517.5	5.4	3517.5	3.1	N-H stretch	Amine	O-H stretch	alcohol
3502.1	2.8	3486.7	2.0	N-H stretch	Amine	O-H stretch	alcohol
3170.4	4.2	3170.4	1.2	O-H stretch	Carboxylic Acid		
2915.8	3.2	2900.4	3.0	C-H stretch	Alkene	O-H	Acid
2738.4	2.9	2761.6	2.7	O-H	Acid		
2476.2	2.8	2491.6	2.6				
2013.3	2.9	2028.7	2.9	C C trible	Alkyne		
1643.1	2.5	1643.1	0.4	C=C	Alkene	Amide	

1396.2	2.0	1419.4	2.5	C-H bending	Alkane

Table 3 Lines in common in the control cornea, and by fourth harmonic of Nd:YAG (266 nm).

CONTROL		**L266**		**Bond**	**Compound**	**Bond**	**Compound**
CM-1	VAL	CM-^{1}	VAL				
3995.8	2.1	3988.1	3.1				
3895.5	2.7	3880.1	3.2				
3563.8	5.2	3586.9	5.7	O-H stretch	Alcohol		
2345.0	2.1	2345.0	2.5				
1519.6	3.6	1511.9	3.2	N-O			
1311.4	3.4	1311.4	3.4				
1079.9	3.3	1079.9	3.2	C-N	Amine, Amide	C-O	Alcohols
1041.4	1.7	1041.4	3.2	C-N	Amine, Amide	C-O	Alcohols
979.7	3.3	979.7	3.5	C=C bending	Alkene		
833.1	3.7	833.1	4.0	C-H bending	1,2,4-trisubstituted		
578.5	4.4	586.3	2.9				
432.0	9.1	432.0	3.1				

Additionally, there were 5 lines appear only in tissues ablated by 193 nm as summarized in Table 4

Table 4 Spectral lines in tissues ablated by 193 nm

L193		**Bond**	**Compound**
CM-1	VAL		
3849.2	1.8		
3702.7	3.6	O-H stretch	alcohol
3031.6	3.5	C-H stretch	Alkene
1920.8	3.0	C C trible	Alkene
1249.6	2.8	O-H bending	phenol

The line 3895.5 cm^{-1} was shifted in the case of L193 to 3849.2 cm^{-1}, which indicates changes in the structure and position of bond. There are new O-H and C-H stretching lines, and triple C bonds. On the other hand, L266 produces only 2 spectral lines that didn't exist in the other spectra as shown in Table 5.

Table 5 Spectral lines in tissues ablated by 266 nm

L266		Bond	Compound
CM-1	VAL		
1835.9	3.1		
1373.1	2.0	C-H bending	alkane

The new spectral lines that appear in L266 are few and lie in the fingerprint region. However, there were new 7 lines are common in L266 and L193 Table 6

There are 7 new lines that didn't exist in the control spectra indicate new O-H stretching due to alcohol bonds and Nitrogen bonds. There were 6 lines absent from L266 and L193. Meaning they are broken bonds. Table 7 presents the line at 3518 in the control which is completely absent in L193 which means this bond is selectively broken by the excimer laser.

Each function group has several characteristic lines. Although a spectral line can be due to more than one function group. However, we need to look to the function group as a hole, that is if not all the lines are present, we reject that group, only if all the lines are present, we identify that group. The problem is not that easy due to shifting the spectral lines. A loss function is used for each group where the optimization program of Python is used. The functional groups can be shown in Fig. 4.

Changes in chemical composition may not be assisted easily, but changes in bonds can indicate that C=C bond does not change. N-H bond is reduced and changed from Amine groups into Alkyne groups. In the same time O-H groups are also reduced. Moreover, the missed C–H ring band was restricted. In line with other histological investigations, the preservation of N-H bonds in L266-treated tissue indicates less protein denaturation [18]. These results agree with previous study that conducted on adult four months hyperoxia mice which may prove that LED laser exposure may lead to an improvement in the membrane structure of retinal cells [19]. Changes in phosphate group (symPO2) and amide I seem to relate to spatial changes in the positions of the phosphate groups in the protein helix. Therefore, it probably reveals initial changes in the secondary and tertiary structure of the protein also may cause changes in genetic materials [20].

The quantitative investigation of the FTIR absorbance spectra revealed vital information about the distinct impacts of L193 and L266 laser treatments on the molecular makeup of the samples. The statistically significant variations in O-H stretch intensities reported for the L193 group compared to controls ($p=0.013$) indicate that the L193 laser causes a more pronounced disturbance of hydrogen bonding networks, water content, and hydroxyl functional groups. In contrast, while the

L266 application produced a significant change, it was limited to the N-H stretch intensities when compared to controls (p=0.021). This unique spectral response suggests that, while the L266 laser affects the N-H bond environment, it may have a less ubiquitous effect on the overall molecule structure than the L193.

Table 6 Common spectral lines in L266 and L193

L193		L266		Bond	Compound	Bond	Compound
CM-1	VAL	CM-1	VAL				
3826.1	2.2	3826.1	3.3				
3640.9	4.3	3664.1	3.6	O-H stretch	alcohol		
3301.5	5.8	3301.5	2.9	C-H	Alkene	O-H stretch	Alcohol
3185.8	3.7	3185.8	3.7	O-H stretch	Carboxylic Acid		
2121.3	3.2	2136.7	3.3	N=C=N	carbodiimide		
1542.8	3.5	1550.5	3.3	N-O			
609.4	5.6	617.1	4.2				

Table 7 Spectral lines in control samples

CONTROL		Bond	Compound	Bond	Compound
CM-1	VAL				
3972.6	1.8				
3394	7.8	N-H	Amine		
1025.9	2.1	C-N	Amine, Amide	C-O	Alcohols
918.0	3.2	C=C bending	alkene		
879.4	3.2	C=C bending	alkene		
640.3	3.8				
532.3	2.7				

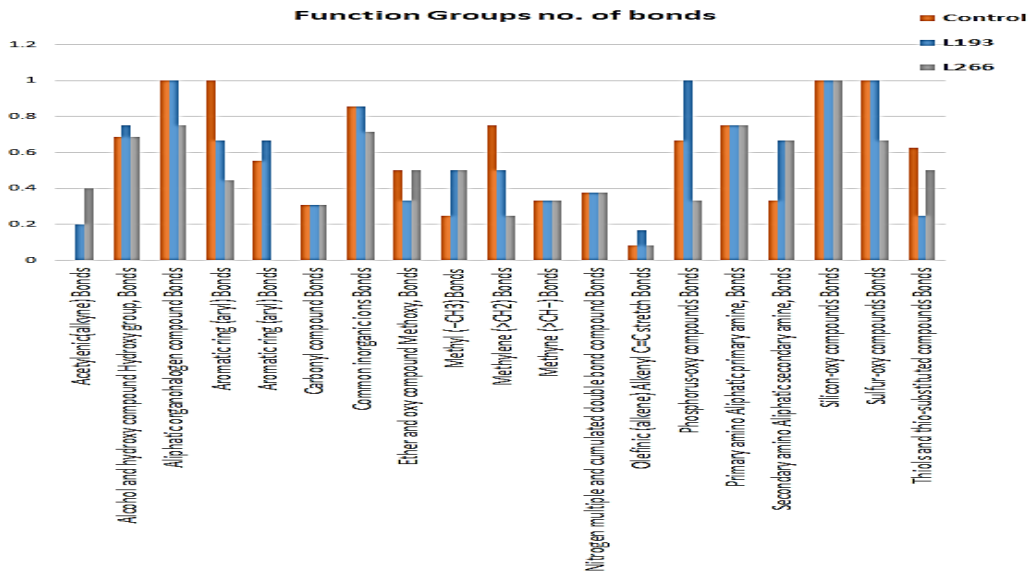

Fig. 4 Detailed Functional Groups Estimation

We further used algorithms to concise and reduce the data as shown in Fig. 5

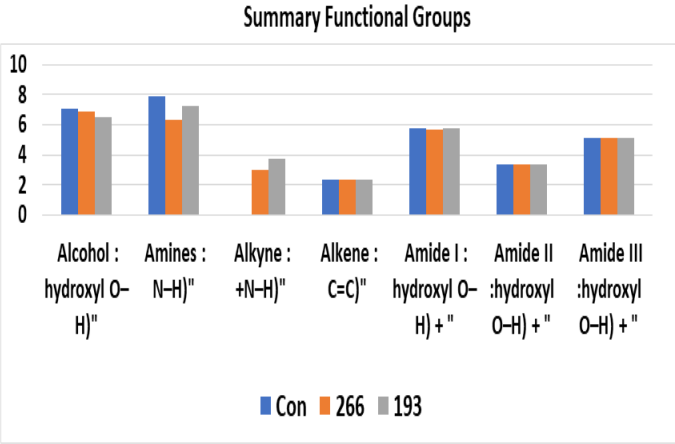

Fig. 5 Reduced list of functional groups.

V. CONCLUSION

There are significant differences between the control, L193, and L266 spectra. Some bonds were missing after the ablation. Other bonds are shifted indicating structural changes. New lines appear at 3340 indicating the presence of secondary amine. L193 produces new 3649, 3240, and 3186 cm-1 which correspond to carboxyl. When using the hole spectra, we find that L266 spectra is correlated to the control at 90%, while the L193 is correlated much less at 70%. Indicating that the changes after exposure to laser 266nm is very near to the control tissue. The implications of these findings are significant for the field of refractive surgery. Understanding the chemical modifications resulting from different laser ablation methods can inform the development of improved techniques for corneal reshaping and vision correction. By elucidating the chemical perspective of corneal ablation, this study contributes to the broader understanding of laser-tissue interactions and furthers the advancement of laser-based surgical procedures.

Conflict of interest: None
Funding: Not Applicable

REFERENCES

1. Willoughby CE, Ponzin D, Ferrari S, Lobo A, Landau K, Omidi Y. Anatomy and physiology of the human eye: effects of mucopolysaccharidoses disease on structure and function–a review. Clin Exp Ophthalmol. 2010;38:2–11. doi:10.1111/j.1442-9071.2010.02363.x.
2. Almubrad T, Akhtar S. Structure of corneal layers, collagen fibrils, and proteoglycans of tree shrew cornea. Mol Vis. 2011;17:2283–91.
3. Antonio JDS, Jacenko O, Fertala A, Orgel JP. Collagen structure-function mapping informs applications for regenerative medicine. Bioengineering. 2021;8(3):1–23. doi:10.3390/bioengineering8010003.
4. Espana EM, Birk DE. Composition, structure and function of the corneal stroma. Exp Eye Res. 2020;198:1–47. doi:10.1016/j.exer.2020.108137.
5. Fu I, Case DA, Baum J. Dynamic water-mediated hydrogen bonding in a collagen model peptide. Biochemistry. 2015;54(39):6029–37. doi:10.1021/acs.biochem.5b00622.Dynamic.
6. Jayasuriya AC, Scheinbeim JI, Lubkin V, Bennett G, Kramer P. Piezoelectric and mechanical properties in bovine cornea. J Biomed Mater Res - Part A. 2003;66(2):260–5. doi:10.1002/jbm.a.10536.
7. Ikemoto Y, Kato Y, Morikawa K, Taniguchi K, Miyamoto A, Yamamoto T. Infrared Spectra and Hydrogen-Bond Configurations of Water Molecules at the Interface of Water-Insoluble Polymers under Humidified Conditions. J Phys Chem B. 2022;126(22):4143–51. doi:10.1021/acs.jpcb.2c01702.
8. Dai F, Zhuang Q, Huang G, Deng H, Zhang X. Infrared Spectrum Characteristics and Quantification of OH Groups in Coal. ACS Omega. 2023;8(19):17064–76. doi:10.1021/acsomega.3c01336.
9. Kong J, Yu S. Fourier transform infrared spectroscopic analysis of protein secondary structures. Acta Biochim Biophys Sin (Shanghai). 2007;39(8):549–59. doi:10.1111/j.1745-7270.2007.00320.x.
10. Tanabe K, Oto TMA, Ura TTAM, et al. Identification of Chemical Structures from Infrared Spectra. Appl Spectrosc. 2001;55(10):1394–1.
11. Sigma-Aldrich. Photometry and Reflectometry [Internet]. [cited 2025 Jun 13]. Available from: https://www.sigmaaldrich.com/EG/en/applications/analytical-chemistry/photometry-and-reflectometry
12. Punjabi D, Kaur A, Bhatia K, Singh K, Singh B, Singh A, et al. Infrared spectrum analysis of organic molecules with neural networks using standard reference data sets in combination with real-world data. J Cheminform. 2025;17(24):1–13. doi:10.1186/s13321-025-00960-2.
13. Baronio CM, Barth A. The Amide i Spectrum of Proteins - Optimization of Transition Dipole Coupling Parameters Using Density Functional Theory Calculations. J Phys Chem B. 2020;124(9):1703–14. doi:10.1021/acs.jpcb.9b11793.
14. North NM, Enders AA, Cable ML, Allen HC. Array-Based Machine Learning for Functional Group Detection in Electron Ionization Mass Spectrometry. ACS Omega. 2023;8(27):24341–50. doi:10.1021/acsomega.3c01684.
15. Krzyżanowski M, Matyszczak G. Machine learning prediction of organic moieties from the IR spectra, enhanced by additionally using the derivative IR data. Chem Pap. 2024. doi:10.1007/s11696-024-03301-z.
16. Mistry BD. Handbook of Spectroscopic Data Chemistry. Jaipur, India: Oxford Book Company; 2009.
17. Sainani KL. Dealing With Non-normal Data. PM&R. 2012;4(12):1001–5. doi:10.1016/j.pmrj.2012.10.013.
18. Abdelkawi SA, Hassan AA. Evaluation of protein change and oxidative stress index after photodynamic therapy of corneal neovascularization. Gen Physiol Biophys. 2012;31:449–55. doi:10.4149/gpb.

19. Sabry M, Abdelkawi S, El Saeid A, El Rashedi A. Low level laser therapy for hyperoxia-induced retinal protein deformations evaluated by FTIR study. Egypt J Biomed Eng Biophys. 2020;21(1):87–96. doi:10.21608/ejbbe.2020.41564.1036.
20. Albarracin R, Natoli R, Rutar M, Valter K, Provis J. 670 nm light mitigates oxygen-induced degeneration in C57BL / 6J mouse retina. BMC Neurosci. 2013;14(125):1–14.

National Institute of Laser Enhanced Sciences, JLSA's Vol.02. Issue.1 (2025)
DOI: 10.21608/JLSA.2025.377593.1033

NILES

Journal of Laser Science and Applications
journal homepage: https://jlsa.journals.ekb.eg

Cairo University

Review "Exploring 2D Graphene Analogues for Advanced Photodetection Applications"

Ahmed Abdelhady A. Khalil[*a,b], Samar Akef[b], Heba A. Shawkey[c], Mohamed A. Swillam[b]

[a] Laser Sciences and Interactions Department, National Institute of Laser Enhanced Sciences (NILES), Cairo University, Giza 12613, Egypt.
[b] Physics Department, School of Science and Engineering (SSE), The American University in Cairo, Cairo 11835, Egypt.
[c] Microelectronics Department, Electronics Research Institute (ERI), Cairo, Egypt.

Abstract:
Extensive research has been conducted on layered transition metal dichalcogenides (TMDCs) to explore their potential as substitutes for graphene and other emerging two-dimensional layered materials (2DLMs). TMDCs constitute a versatile family of 2D materials exhibiting exceptional optical properties, positioning them as highly promising candidates for the development of advanced, multifunctional, high-performance optoelectronic devices. The tunability of their band gap energies - particularly in molybdenum and tungsten disulfides - enables precise control over their electronic properties, facilitating their transition from insulating to semiconducting and even superconducting states. This study emphasizes the synthesis of transition metal-doped TMDCs and investigates their integration as graphene-like materials to enhance optoelectronic functionalities. Furthermore, computational analyses are employed to predict and elucidate the properties of the doped structures, providing insights into their potential for next-generation optoelectronic applications.

Keywords: 2D materials, Graphene like materials, TMDC, Semiconductors, Optoelectronic devices, Light harvesting devices.

I. INTRODUCTION

Since the landmark discovery of graphene in 2004 [1], the field of two-dimensional (2D) materials has expanded rapidly, driven by their unique electronic, optical, mechanical, and catalytic properties [2,3]. While graphene's exceptional conductivity and transparency have positioned it as a key material, the limited bandgap restricts its direct application in photodetection. Consequently, research has shifted towards graphene analogues such as transition metal dichalcogenides (TMDs), black phosphorus, MXenes, and emerging III–V 2D semiconductors, which offer tunable bandgaps and rich optoelectronic functionalities [4–7]. Despite significant progress, the translation of these materials into practical photodetectors faces three core challenges:

Scalable Synthesis: Achieving high-quality, uniform, defect-free monolayers on an industrial scale remains elusive [8,9]. For example, while chemical vapor deposition (CVD) can produce large-area graphene, the transfer process introduces defects and contamination, impairing device performance.

Property Tunability & Functionalization: Precise control over doping, defect engineering, and heterostructure formation is necessary for optimizing responsivity, speed, and spectral range [10–12]. However, current methods often lack reproducibility and interface control.

Device Integration & Stability: Integrating these materials into heterostructures adds complexity, especially for air-sensitive materials like black phosphorus, which require encapsulation strategies [13–17].

Corresponding Author: Ahmed Abdelhady A. Khalil (a.abdelhady@niles.edu.eg)
Received April 21, 2025 Revised date: June 13, 2025 Accepted June 17, 2025

ISSN: 1687-8892

This review addresses a central question: How can different classes of 2D graphene-like materials overcome these barriers to enable practical applications in energy storage, catalysis, flexible electronics, and optoelectronics? By organizing the discussion around these three interrelated challenges, we shift from a purely descriptive overview to a critical analysis of material classes.

A comparative insight:

Table 1: Overview of material classes, synthesis approaches, limitations, and potential applications in photodetectors.

Material Class	Synthesis Approach	Major Limitation	Potential for Photodetector Application
Graphene	CVD, Mechanical exfoliation	Transfer-induced defects	High transparency, low resistance; limited bandgap
TMDs	CVT, Sulfurization	Uniformity at large scale	Adjustable bandgap, strong light-matter interaction
MXenes	Etching of MAX phases	Oxidation susceptibility	Metallic conductivity, tunable surface chemistry
Black Phosphorus	Mechanical exfoliation	Chemical instability	Direct bandgap, high mobility

Table (1) presents a comparative analysis of various material classes utilized in photodetector applications, highlighting their synthesis approaches, inherent limitations, and potential advantages. Graphene, synthesized via CVD and mechanical exfoliation, offers high transparency and low resistance but suffers from transfer-induced defects and a limited bandgap. Transition metal dichalcogenides (TMDs), obtained through CVT and sulfurization, provide adjustable bandgaps and strong light-matter interaction; however, achieving uniformity at a large scale remains a challenge. MXenes, derived by etching MAX phases, exhibit metallic conductivity and tunable surface chemistry but are highly susceptible to oxidation. Black phosphorus, produced through mechanical exfoliation, features a direct bandgap and high carrier mobility, though its chemical instability poses a significant limitation. The comparison underscores both the promising attributes and challenges of these materials in advancing photodetector technologies. A previous study presented the fabrication of Schottky and pn photodiodes using SiC/MoS_2 composite films via physical vapor deposition. The devices were structurally analyzed and electrically characterized. The vertical design enabled high efficiency, with the pn-diode achieving 14.68% EQE and 63.22 mA/W responsivity, while the Schottky diode reached 6.68% EQE and 28.25 mA/W. Response times were under 1 ms for both. The results highlight the potential of SiC/MoS_2 vertical structures for efficient optoelectronic applications [18]. Another paperwork reported the fabrication of a 1T-MoS_2-based pn photodiode using RF sputtering for fast photodetection. Structural analysis was performed using SEM and FTIR, while electrical performance was evaluated via I–V measurements from −2 to +2 V. The device achieved an EQE of 9.8%, an IQE of 10.5%, and a response time of 1.748 ms, demonstrating its suitability for rapid-response optoelectronic applications [19]. Recent studies have demonstrated that EQE of GaN/MoS_2 photodiodes can reach up to 11.86% in pn-junction configurations and 8.26% in Schottky device. Correspondingly, IQE has been reported to attain values of up to 13.78% and 10.02% for the pn- and Schottky-type photodiodes, respectively. Furthermore, response times have been observed to be approximately 800 µs for Schottky photodiode and 18.23 ms for pn-type device. [20].

II. GRAPHENE LIKE MATERIALS-BASED PHOTODETECTOR PHOTONICS

2.1. Dynamic key performance parameters

To synthesize a light-harvesting apparatus, specifically a photodiode, it is imperative to comprehend the principal performance metrics that delineate its characteristics. The responsivity (R) of a photodetector serves as a quantitative parameter, defined as the ratio of the generated photocurrent to the incident power of electromagnetic radiation incident upon the device. This metric offers a direct representation of the efficacy with which the photodetector transduces optical power into an electrical current signal. the equation is defined as $R = \frac{I_{ph}}{P}$, where I_{ph} represents the photocurrent is delineated as the disparity observed between the current generated under illumination conditions and the current detected in the absence of illumination, commonly referred to as the dark current ($I_L - I_D$), and P represents the power of the incident light. Within the realm of photovoltaic devices, an alternative definition of photo-responsivity can be considered. In this formulation, photo-responsivity is expressed as the ratio of the open-circuit voltage generated under illumination (V_p) to the power of the incident optical radiation (P). This alternative representation provides a measure of the photovoltaic conversion efficiency in terms of the voltage produced per unit of impinging optical power. This may be articulated as $R = \frac{V_p}{P}$. The spectral response range, wherein the responsivity decreases by 50%, corresponds to the interval of wavelengths encompassing the maximum and minimum currents. The noise equivalent power (NEP) denotes the minimum incident optical power required to yield a signal-to-noise ratio of unity at a frequency of 1 Hz. This metric serves as a measure of the ability of a photodetector to detect faint optical signals. Mathematically, the NEP can be represented as the quotient of the noise current (I_N) within a 1 Hz frequency bandwidth and the responsivity (R) of the photodetector

$NEP = \frac{I_N}{R}$, where I_N represents the noise current within a frequency span of 1 Hz. Furthermore, the quantum efficiency (Q.E.) refers to the proportion of charge carriers generated per incident photon. This parameter can be mathematically expressed as the ratio of the number of electrons produced at the output to the number of photons input to the device, denoted as $Q.E. = Electron\ Out / Photon\ In$. The power of light absorption at a given position z can be mathematically represented as:

$$P_z = P_{in}\ (1 - \mathcal{R})\ (1 - e^{-\alpha z}).$$

In this equation, where the incident power of light is denoted as Pin, the reflectivity of the material as R, the absorption coefficient of the material as α, and the distance from the surface as the variable z. The equation representing the number of photocarriers generated (η) by the illumination of individual photons may be expressed as:

$$\eta = (1 - \mathcal{R})\ (1 - e^{-\alpha d})$$

where d is the thickness of the active material with the maximum reflectivity $\mathcal{R}$. Furthermore, the detectivity (D) of a photodetector can be defined as the inverse of the noise equivalent power (NEP), expressed as $D = \frac{1}{NEP}$. The specific detectivity, also known as the spatially resolved detectivity, relates to the detectivity quantified within a designated unit area and across a frequency bandwidth of 1 Hz. It can be mathematically expressed as:

$$D = A_d B^{1/2} / NEP,$$

where A_d represents the area of the device and B denotes the bandwidth. Efficient detection of a weak signal becomes attainable through heightened localized detectivity exhibited by the photodetector. The photo-response time of a photodetector characterizes the temporal interval required for the device to convert incident optical radiation into an electrical signal, serving as a quantitative metric of its responsiveness. This parameter is evaluated through the measurement of both rise time (t_r) and fall time (t_f). The rise time denotes the duration for the electrical signal to transition from 10% to 90% of its steady-state value, whereas the fall time indicates the time required for the signal to transition from 90% to 10% of its steady-state value. These temporal metrics provide insight into the speed and efficiency with which the photodetector can respond to changes in the incident optical power. Both of these time measurements are essential in fully characterizing the photo-response capability of a gadget (Ahmed Abdelhady Khalil et al. 2024) [18-20]. The photoconductive gain (G) of a device can be defined as the quotient obtained by dividing the charge carrier lifetime associated with the generation of light and the transit time of the charge carriers as they drift through the device. Accordingly, the equation can be expressed as:

$$G = Carrier\ lifetime\ /\ Drift\ transit\ time$$

It is imperative to quantify this gain in order to assess the efficacy of the circulation of photogenerated carriers within the channel. The determination of G necessitates considering the transit time, which is contingent upon factors such as carrier mobility, the length of the device channel, and the magnitude of the applied voltage. The photoconductive gain can alternatively be quantified by the absorption power of light, denoted as P_{abs}. Understood, the gain (G) of the photodetector in this context can be expressed mathematically as: $G = (I_{ph}\ /P_{abs})\ (h\nu/\ q)$, where I_{ph} is the photocurrent generated by the device, where P_{abs} is the absorbed optical power, hν is the photon energy and q is the elementary unit of electric charge.

2.2. Graphene

Graphene, an allotrope of carbon, presents a two-dimensional structure defined by sp^2 hybridization. This hybridization process entails the amalgamation of atomic orbitals to generate novel hybrid orbitals, thereby modifying the electron configuration of the atom. Graphene has a hexagonal arrangement of carbon atoms, as depicted in Figure 1A by Roberts et al. (2010), This hexagonal lattice structure is referred to as a "honeycomb" lattice, the distinctive hexagonal arrangement of carbon atoms in graphene gives rise to its unusual and valuable electronic behavior, which is a key reason for the intense scientific and technological interest in this material [21], shows each atom forming strong covalent bonds with three neighboring atoms, with a distance of 0.142 nm between carbon atoms (Roberts et al., 2010) [21]. The valence and conduction bands of graphene overlap significantly at the Fermi level, resulting in pronounced symmetry (Berger et al., 2004) [22]. As a consequence of its monolayer atomic thickness and robust crystalline configuration, graphene exhibits distinctive attributes such as high carrier mobility, as highlighted by Brida et al. (2013) [23]. Concomitant with its single-layer atomic configuration and stable crystalline lattice structure, graphene exhibits a remarkably broad light absorption spectrum. This spectral range encompasses wavelengths spanning from the ultraviolet (UV) to the far-infrared (FIR) regions, and furthermore extends into the terahertz frequency domain, as elucidated in the work of Wang et al. (2008) [24]. Furthermore, studies have elucidated graphene's exceptional interactions with electromagnetic radiation, as detailed in the work of Iqbal et al. (2022) [25], Demonstrating an optical absorption rate of 2.3% across the visible and near-infrared spectral ranges (Nair et al., 2008) [26]. Moreover, through the modulation of its Fermi level, graphene has the capability to selectively absorb distinct wavelengths, rendering it highly efficient in photodetectors, notably in the mid-to-far-infrared wavelength spectrum. While graphene's zero-bandgap limits its direct usage in photodetection, strategies like doping and heterostructure formation can induce finite bandgaps. Recent developments focus on direct growth on flexible substrates to avoid transfer-induced defects [11].

Analytical insight:

Optimal synthesis involves balancing large-area uniformity with minimal defects, which directly correlates with device responsivity and noise characteristics.

2.3. Transition metal dichalcogenides (TMDCs)

Chemical vapor transport (CVT) and sulfurization techniques produce high-quality monolayers but face reproducibility issues over large areas [12,13].

Critical analysis:

Reproducibility of monolayer thickness and defect density remains a bottleneck, impairing spectral responsivity and response time consistency. TMDCs constitute a distinct class of semiconductor materials characterized by their layered architectures, which can consist of single or multiple layers arranged in a hexagonal symmetry. TMDCs are typically denoted by the general chemical formula MX_2, where M represents transition metal elements such as molybdenum (Mo), rhenium (Re), and tungsten (W), while X denotes chalcogen elements including sulfur (S), tellurium (Te), and selenium (Se). A multitude of TMDCs exhibit similar crystal structures, with notable examples including MoS_2, WS_2, and $MoSe_2$. TMDCs exhibit three primary structural phases: the trigonal prismatic (2H) phase, the distorted octahedral (1T) phase, and the dimerized (1T') phase are depicted in Figure 1B, as presented by Manzeli et al. in 2017 [27]. A considerable number of these patterns, specifically, exhibit a monolayer configuration resembling honeycomb structure, which can be further classified into distinct subcategories. Structures with trigonal prismatic geometry and D6h group symmetry are known as honeycomb (2H) structures, while those with distorted octahedral geometry and D3h group symmetry are referred to as centered honeycomb (1T) structures. (Ataca et al., 2012 [28]; Svetin et al., 2014 [29]; Manzeli et al., 2017 [27]).

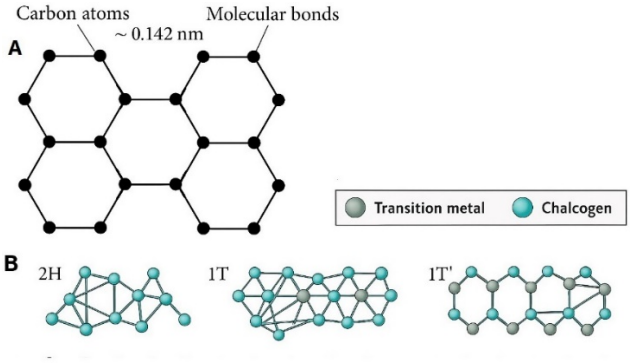

Figure 1 (A) Graphene structure (Roberts *et al.*, 2010) [21], and (B) Single layered atomic structure of TMDCs in trigonal prismatic phase (2H) distorted octahedral phase (1T) and dimerized phase (1T') states (Manzeli *et al*., 2017) [27].

Approximately 40 distinct types of transition metal dichalcogenide (TMDC) materials can be obtained by combining various chalcogenide elements with transition metals. The authors highlight a range of distinctive features, including specific charge density waves (Svetin et al., 2014) [30], semimetallic properties (Shishidou et al., 2001) [31], and notable superconductivity (Xi et al., 2016) [32]. In some instances, the expansion of relevant layers induces a transformation in the bandgap of monolayer MoS_2 from a direct bandgap of approximately 1.8 eV to an indirect bandgap of 1.2 eV in its bulk semiconductor form (Splendiani et al., 2010) [33]. In the context of group V layered dichalcogenides such as TaS_2, $TaSe_2$, and $NbSe_2$, it has been observed that charge density waves (CDWs) manifest within these materials, exhibiting a distinct phase. These waves are generated as a result of the presence of layers inside the material, the application of biassing, the deformation of substrates, and/or the stimulation of electric current. Several other topological semimetals, including $PtSe_2$, $PdTe_2$, and $PtTe_2$, exhibit remarkable chiral coupling transport properties alongside nonlinear optical characteristics (Fei et al., 2017) [34]. Additionally, these materials demonstrate peculiar physical properties, including unique carrier characteristics and wideband photodetection capabilities. The aforementioned features mostly arise from the electrical state being symmetrically insulated. In addition to other notable characteristics, TMDCs have a wide range of applications across multiple scientific disciplines. Several examples of these include optoelectronics, customizable excitonic devices, and spin-valley lasers (Ye et al., 2016a) [35].

2.4. MXenes & 2D Semiconductors

Etching methods for MXenes result in **layer control** but are hindered by **oxidation** [14]. Black phosphorus, with its direct bandgap, suffers from **ambient instability** [15].

Key future direction:

Developing protective encapsulation layers and in-situ growth methods will be critical to improve stability and uniformity.

2.5. Black Phosphorous

Black phosphorus (BP), a recently identified addition to the family of layered materials, exhibits a bandgap that is dependent on its thickness, ranging from 0.3 to 1.5 eV. This characteristic positions black phosphorus as a promising candidate for high-performance optoelectronic devices operating across the expansive infrared spectrum. Its 2D sheets can be seamlessly integrated with conventional materials like silicon (Youngblood et al., 2015) [36]. These sheets are also adaptable to various substrates, including flexible ones, as noted by Zhang et al. (2020) [37] and Qiao et al. (2014) [38]. Contrasted to other 2D materials, BP nanosheets display superior

optical absorption, which mounts as the layer count drops Zhang et al. (2020) [37]; Qiao et al. (2014) [38]. Nevertheless, conventional BP photodetectors and solar cells realize challenges in detecting faint optical signals due to their inadequate responsivity, primarily studied in visible and near-infrared ranges (Liu et al., 2018 [39]; Ye et al., 2016b [40]). Unlike graphene, BP crystals have lower crystalline symmetry due to their puckered layer structure, resulting in asymmetric band structures that influence both electrical and optical conductivity (Shao et al., 2014 [41]; Wang and Lan, 2016 [42]). Figure 2 illustrates the multilayered 2D structure of BP (Shao et al., 2014) [41]. This structural asymmetry significantly impacts carrier transport characteristics. Research initiatives focused on BP-based photodetectors aim to enhance several key aspects: increasing responsivity, broadening spectral detection, minimizing dark current, improving time response, boosting the degree of sensitivity to polarization, and achieving waveguide integration.

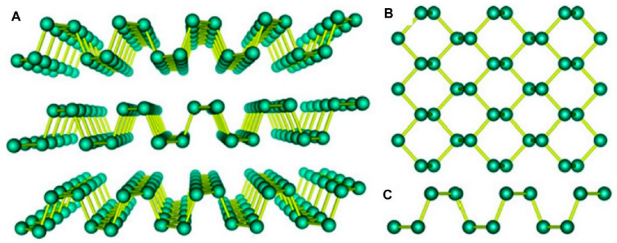

Figure 2 (A) black phosphorus multilayered crystal structure (Shao *et al*., 2014) [42], (B) Top view (Shao *et al*., 2014) [42], and (C) Side view (Shao *et al*., 2014) [42].

2.6. Group V-Based 2D-Materials

The anticipated growth of the 2D materials industry, especially those derived from group V elements, is expected to be significant, fueled by their versatility and potential for various electronic applications. This optimism stems from their notably high carrier mobility and adjustable bandgap, a feature notably absent in graphene and TMDCs, which typically exhibit indirect bandgaps, leading to diminished carrier mobility (Britnell et al., 2013 [43]; Zhang et al., 2016a [44]). Black phosphorus (BP) features a distinctive multilayered crystal structure composed of puckered honeycomb layers, akin to graphene. The layers are held together by weak van der Waals forces, resulting in anisotropic properties that make BP particularly intriguing for use in electronics and optoelectronics. Its direct bandgap crystal lattice structure promotes efficient light coupling, positioning black phosphorus as a promising candidate for a variety of optoelectronic applications, including photodetectors, sensors that cover the visible to mid-infrared ranges, and laser technologies (Shao et al., 2014 [41]; Iqbal et al., 2021c [45]). Additionally, tricyclic arsenene, characterized by notable stability and tunable bandgap, shows potential for optoelectronic devices due to its unique properties (Ma et al., 2016 [46]; Zhang et al., 2016a [44]). The anisotropic nature of 2D arsenic material, akin to black phosphorus, presents significant implications, surpassing even black phosphorus in this regard, enhancing its resilience compared to multilayered phosphorus. The application of ultra-thin layer samples on large surfaces offers practical advantages in preparation and application. While bulk antimony shares electrical transport traits with metals, its 2D layered form, with an indirect bandgap, poses challenges for optoelectronic devices despite its high carrier density and mobility (Zhang et al., 2016a [44]; Xie et al., 2016 [47]). The burgeoning interest in utilizing arsenic and antimony as emerging 2D stacked semiconductor materials across various device applications underscores their research significance (Zhang et al., 2016a; Xie et al., 2016) [47].

2.7. Group III-V Based 2D-Materials

Antimonides, including GaSb, InSb, AlSb, InAs, and their ternary and quaternary alloys, fall under the category of III-V semiconductors. The band alignments of these materials span a wide spectrum, ranging from type I to type III configurations (Vurgaftman et al., 2001) [48] driving the prevalent use of integrated photodetectors. Photodetectors utilizing scalable Ge have demonstrated high efficiency and maturity in sensing frequencies exceeding 67 GHz at a rate of 100 Gigabauds (GBd) (Chen et al., 2016) [49]. Many III-V materials exhibit higher absorptivity and can directly adjust the bandgap, making them ideal for efficient operation in optical sensing devices like lasers (Staudinger, 2020) [50] and LEDs (Li et al., 2019) [51].

III. DEVICE ARCHITECTURE AND PERFORMANCE METRICS

3.1. Device Structures

Vertical heterostructures (e.g., graphene/TMD) have demonstrated high responsivity due to efficient charge separation [16].

Comparison:

Vertical stacking improves photoresponsivity but introduces interface resistance; lateral junctions offer better control but are harder to scale.

3.1. Critical Metrics and Limitations

Table (2) provides an overview of key performance parameters for photodetectors, highlighting their current capabilities and associated limitations. Responsivity, which measures the efficiency of light conversion into electrical signals, can reach up to 1000 A/W in optimized heterostructures; however, interface quality remains a limiting factor in achieving higher efficiency. Response time, crucial for fast detection, can be reduced to sub-millisecond levels, but there is an inherent trade-off between speed and responsivity. Noise equivalent power (NEP), a metric indicating sensitivity, has been

decreasing with improvements in material quality, yet further reductions are necessary through interface engineering to enhance overall performance. This summary underscores the challenges and opportunities in advancing photodetector technologies.

Parameter	Current State	Limitation
Responsivity	Up to 1000 A/W in optimized heterostructures [17]	Interface quality limits efficiency
Response Time	Sub-millisecond responses possible [18]	Trade-offs between responsivity and speed
Noise EQ Power	Decreasing with material quality	Needs further reduction by interface engineering

Table 2: Overview of device parameters, current performance, and key limitations impacting responsivity, response time, and noise-equivalent power.

Future Directions

- Hybrid materials combining high responsivity and stability.
- Interface engineering to reduce contact resistance and trap states.
- Encapsulation for air-sensitive materials.

IV. 2D-MATERIALS BASED PHOTODETECTORS

4.1. Graphene-based photodetectors

Graphene, a two-dimensional material characterized by its hexagonal structure, demonstrates optical absorption within a limited spectral range due to its extremely thin thickness. The photoresponsivity of the device is somewhat restricted, as indicated by a value of 0.5 mA/W and a bandwidth of 500 GHz, as reported by Mueller et al. (2010) [52]. According to reports, photodetectors composed of metal-graphene-metal structures featuring asymmetric electrodes demonstrate a notable responsivity of 6.1 mA/W. The aforementioned outcome stands in opposition to the exceptional characteristics of graphene, such as its remarkable velocity, compatibility with circuits, and versatility across a broad range of frequencies (Lou et al., 2016) [53]. Several solutions have been proposed thus far to enhance the optical absorption capabilities of graphene photodetectors. One such approach involves the utilization of nanostructured plasmonics. This technique enhances the concentration of light and can be effectively employed for achieving multicolor detection while also improving the quantum efficiency of the device. According to a study conducted by Fang et al. (2012) [54], it has been observed that incorporating plasmonic nano-antennas within the layers of a graphene photodetector can significantly enhance its quantum efficiency, reaching up to 20%. Additionally, by controlling the resonance of these nanostructures, it is possible to manipulate the operational bandwidth of the device. Another approach to improve the photoresponsivity involves the integration of quantum dots (QDs) into graphene. According to the methodology employed, the photoresponsivity seen in photodetection exhibits a greater value, specifically reported to range between 10^7 and 10^8 A/W, as indicated by Konstantatos et al. (2012) [55]. The aforementioned phenomena enables the efficient transfer of photo-excited carriers to the graphene layer, while simultaneously trapping carriers of opposite charge due to the field-effect doping effect. The utilization of PbS-QDs has been observed in graphene photodetectors, with a claimed photoresponsivity of 10^7 A/W (Sun et al., 2012) [56]. An alternative strategy that has demonstrated efficacy involves the utilization of photodetectors based on graphene QDs within microcavities, resulting in enhanced photoactivity in graphene with reduced operational speed and bandwidth limitations (Gan et al., 2013) [57]. The device has a pretty high level of response speed. Moreover, it demonstrates exceptional efficiency, an extensive range of bandwidth, and heightened light responsivity. Nevertheless, the dimensions of the device are greater compared to traditional photodetectors, which is identified as a significant limitation (Kim et al., 2011) [58]. The study focused on investigating the bolometric responses of single-layer graphene (SLG) under ambient temperature conditions by applying bias. This observation unveils two distinct mechanisms that contribute to the generation of polarized bolometric photocurrents: (1) the augmentation of conductance through the introduction of light-induced carriers, and (2) the reduction in conductance resulting from the temperature dependence of carriers. The dominant mechanisms in systems influenced by varying electric fields are photovoltaic (PV) effects, particularly when the carrier density is notably low. In the context of ambient-temperature graphene bolometric detectors, it has been observed that photo-thermoelectric (PTE) effects play a significant role. Additionally, Freitag et al. (2013) reported a photoresponsivity of 0.2 mA/W [59]. To address this issue, Yan et al. (2012) [60] utilized a bi-layer graphene (BLG) structure that incorporates a dual gate configuration, including an anti-reflective top gate (Koppens et al., 2014) [61]. The device was measured using a four-terminal configuration while being exposed to mid-infrared (MIR) radiation at a wavelength of 10.6 micrometers. The detection of light response was achieved using a bolometric mechanism, as described by Liu et al. (2013) [62]. Although this system is typically examined using radiofrequency waves, it is also applicable to optical detection (Vora et al., 2012) [63]. Graphene is a favorable choice for room-temperature photodetection applications due to its notable attributes, including enhanced mobility, reduced carrier transit time, and heightened susceptibility to electrostatic perturbations from photogenerated surface carriers. Colloidal quantum dots (QDs) synthesized using PbS, as demonstrated by Sun et al. (2012) [56], Jeong et al.

(2020) [64] and Konstantatos et al. (2012) [55], serve as examples of light-absorbing particles sensitized by graphene. Detecting photons under low incident light intensities, particularly at the single-photon level, requires a gain mechanism that generates a large number of electrical carriers in response to each photon. This objective can be achieved through deliberate modification of the surface properties to enhance light absorption capabilities, thereby facilitating the effective passage of charge carriers into the conductor. This phenomenon is observed alongside a modification in the resistance versus gate-voltage relationship, (Konstantatos et al. in 2012) [55].

4.2. TMDCs based photodetectors

TMDCs such as MoS_2, $MoSe_2$, WS_2, WSe_2, ReS_2, $ReSe_2$, and $MoTe_2$, reveal promising characteristics for photodetection applications. MoS_2's monolayered and few-layered configurations possess high charge carrier mobility (~200 $cm^2V^{-1}s^{-1}$), a direct bandgap of 1.8 eV, efficient current on/off ratios, and improved light-matter interaction (Splendiani et al., 2010 [65]; George et al., 2021 [66]; Ponomarev et al., 2015 [67]). George et al. (2021) [66] stated the discovery of a robust and sizable persistent photoconductor, called the gigantic persistent photoconductor (GPPC), fabricated via chemical vapor deposition (CVD) of monolayer MoS_2, displaying improved conductivity up to a factor of 10^7 when operated at 365 nm. Yin et al. (2012) [68] employed MoS_2 nanosheets in a transistor arrangement, exhibiting a responsivity of 75 mA/W and a response speed of 50 ms at a wavelength of 670 nm. Lopez-Sanchez et al. (2013) [69] enhanced the MoS_2 monolayer device, attaining a responsivity of 800 mA/W at 680 nm. $MoSe_2$, with its significant photoluminescence and direct bandgap of 1.5 eV, has been investigated for photodetection (Zhang et al., 2014a) [70].

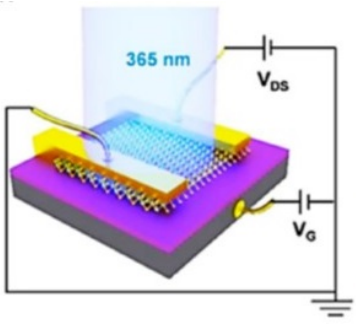

Figure 3 MoS_2 single-layered phototransistor Schematic (George et al., 2021) [66].

Synthesis methods like chemical vapor deposition (CVD) and exfoliation have superior device performance (Abderrahmane et al., 2014 [71]; Lu et al., 2014 [72]). Wang et al. afforded a widespread overview of 2D materials in the background of photodetection applications (Wang et al., 2018) [73], whereas Xia et al. supervised a study on a photodetector based on $MoSe_2$ (Xia et al., 2014a) [74]. For $MoSe_2$, Zhang et al. (2013a) [75] synthesized a monolayer phototransistor, demonstrating higher responsivity compared to multilayered devices.

On the contrary, the application of CVD to fabricate multilayered $MoSe_2$ devices has been found to demonstrate improved responsivity. However, it is important to note that this improvement in responsivity is accompanied by a reduction in response speed, as reported by Jung et al. in 2015 [76]. Similarly, exfoliated $MoSe_2$ photodetectors exhibited improved responsivity (Abderrahmane et al., 2014) [71]. WS_2 photodetector, which belongs to the family of TMDC materials, has been successfully synthesized by various methodologies as documented by Sik Hwang et al. in 2012 [77]. WS_2 photodetectors synthesized via various methods have demonstrated responsivity correlated with photon energy, reaching 92 μA/W with a response speed of 5 ms within a wavelength range of 457–647 nm (Perea-López et al., 2013) [78]. The researchers demonstrated a correlation between photon energy and their detectors, as evidenced by the measured device responsivity of 92 μA/W and response speed of 5 ms, which were obtained within an operating wavelength range of 457–647 nm. Additionally, the utilization of WSe_2, characterized by its single-layer and multilayered structures, has been extensively examined in photodetection applications. In a study by Zhang et al. (2014b) [79], chemical vapor deposition (CVD) was employed to synthesize a monolayered WSe_2 device. The investigation into the effect of varying the work function in metal contacts revealed that the Pd contact achieved the highest responsivity of 1.8×10^5 A/W at an operating wavelength of 650 nm, while the Ti contact exhibited the lowest device responsivity. The Titanium (Ti) contact displayed an efficient response time of 23 ms, which is longer than that of other metal contacts. This delay can be attributed to the presence of a Schottky contact between the active materials, underscoring the importance of improving metal contact performance to enhance device efficacy. $MoTe_2$ has garnered significant interest due to its intriguing optoelectronic properties (Lin et al., 2014) [80]. TMDs like ReS_2 and $ReSe_2$ have a layered structure similar to black phosphorus. These materials demonstrate interesting properties due to their anisotropic nature, impacting their bandgap and carrier mobilities. Such characteristics play a significant role in determining the performance of devices based on these materials, like transistors and photodetectors. (Wilson and Yoffe, 1969 [81]; Yang et al., 2014 [82]). $ReSe_2$ devices have demonstrated a responsivity of 95 A/W and rapid response time at 633 nm (Yang et al., 2014) [82]. Despite their efficacy, TMDC-based photodetectors exhibit environmental sensitivity, influencing device performance (Jo et al., 2016) [83]. Encapsulation passivation techniques can mitigate this sensitivity (Jo et al., 2016) [83]. The utilization of encapsulation passivation techniques can effectively reduce the device's reliance on external factors, hence improving its overall efficiency. While $ReSe_2$ has demonstrated efficacy as a photodetection device, it is accompanied with a limitation whereby the current flow does not revert back to its original dark current level under low-light conditions. The

observed phenomenon can be ascribed to the sluggish recombination of charge carriers, a characteristic that has been substantiated by the application of brief pulses to the gate terminals to reset the device (Konstantatos et al., 2012 [55]; Ahn et al., 2021 [84]). In the study by Liu et al. (2016a) on ReS_2 photodetectors detecting polarized light at an operational wavelength of 1064 nm, the responsivity values ranged from 3.97×10^3 to 1.18×10^6 A/W. The enhancement in responsivity for specific polarizations could be linked to electron doping, as depicted in Figure 3B of their research. This electron doping process likely plays a significant role in the observed improvement in detecting polarized light using ReS_2 photodetectors [85]. TMDCs can function as photodiodes or photoconductors under appropriate biasing conditions (Lopez-Sanchez et al., 2013) [86]. Integration of TMDCs with graphene electrodes has shown potential for efficient current generation (Koppens et al., 2014) [61]. Additionally, WS_2-based flexible photodetectors demonstrated high photoresponsivity (Li et al., 2020) [86]. The Graphene-WS_2-Graphene configuration showed enhanced detectivity and photoresponsivity (Pham et al., 2022) [87]. TMDC-based photodetectors generally exhibit responsivity between 10^{-7} and 10^7 A/W and response times ranging from 10^{-5} to 10^3 s, with improved responsivity observed near material traps or interfaces (Pham et al., 2022) [87]. Optimization of device performance considers synthesis methods, environment, and layer count (Pham et al., 2022) [87].

V. PHOTODETECTORS IN VISIBLE AND NIR REGIONS

Photodetectors operating in the visible and near-infrared (IR) spectrum are crucial for various applications, and graphene-based devices have shown promise in this regard. Graphene photodetectors, in conjunction with metal electrodes, can efficiently separate charge carriers, resulting in a responsivity of up to 6.1 mA/W as shown in Figure 4 (A) (Mueller et al., 2010) [52]. Additionally, vertically stacked layer graphene devices with metal contacts exhibit wavelength-dependent performance, leveraging the carrier multiplication effect (Chen et al., 2015) [88]. Despite its lack of a bandgap, graphene is complemented by 2D transition metal dichalcogenides (TMDCs) like MoS_2, $MoSe_2$, WS_2, WSe_2, ReS_2, and $ReSe_2$, which have shown efficiency in photodetection applications (Mukherjee et al., 2015 [89]; Zhang et al., 2016c [90]).

The bulk form of MoS_2 has an indirect bandgap of 1.2 eV, which can be altered to 1.8 eV by transforming the material into a nanosheet or thin film configuration. The material has favorable characteristics for near-infrared (NIR) detection, including a low dark current and a high on/off ratio. This is attributed to its strong compatibility with the incident NIR wavelength light, as demonstrated in studies conducted by Lopez-Sanchez et al. (2013) [70], Radisavljevic et al. (2011) [91], Ehsan Elahi et al. (2024) [92], V. Janardhanam et al. (2023) [93] and M. Malik et al. (2022) [28]. According to a study conducted by Lopez-Sanchez et al. in 2013 [69], photodetectors based on single-layered MoS_2 demonstrate a responsivity of 880 A/W when operated at a wavelength of 561 nm. The utilization of $MoSe_2$ in spintronics is advantageous due to its notable spin splitting energy. The material under investigation exhibits a comparatively longer response time when compared to the MoS_2 devices as seen in Figures 4D and E (Wang et al., 2018) [73]. In their study, Liu et al. successfully produced a photodetector based on multilayered ReS_2. They demonstrated that this photodetector had a response of 88600 A/W at a specific operating wavelength of 532 nm, as illustrated in Figures 4F and G (Liu et al., 2016a) [85]. The efficiency of this reaction is higher in comparison to that of the device based on single-layered RSe_2.

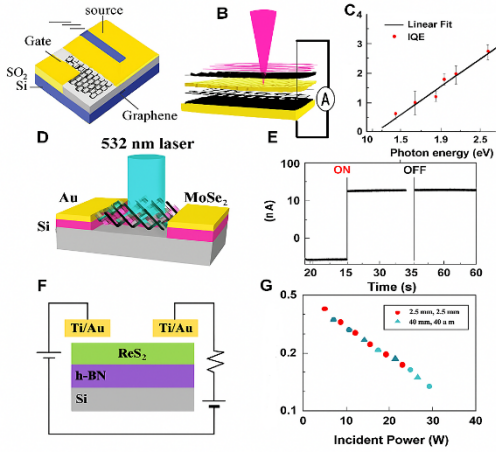

Figure 4 (A) Graphene photodetector with different metal contacts Mueller *et al*. (2010) [52], (B) graphene configuration where multiple layers are stacked on top of each other Chen *et al*. (2015) [88], (C) graphene optical properties based on photon energy dependence such as IQE, (D) Monolayered $MoSe_2$ photodetector Wang *et al*. (2018) [73], (E) With its time resolved current Wang *et al*. (2018) [73], (F) Multilayered $ReSe_2$ photodetector Liu *et al*. (2016a), and (G) With its responsivity Liu *et al*. (2016a) [85].

VI. GAPS, CHALLENGES, AND FUTURE OUTLOOK

Despite progress, scalability remains the overarching challenge. To bridge lab-scale demonstrations and industrial applications, focus should be on:

- Scalable synthesis techniques: Roll-to-roll CVD, ALD, and direct growth methods.
- Material stabilization: Encapsulation and surface passivation.
- Heterostructure engineering: Precise control over interfaces for optimized carrier dynamics.

6.1. Proposed research directions

- Developing high-throughput synthesis for uniform 2D layers.

- In-situ characterization during growth for real-time quality control.
- Exploring novel heterostructures that combine the strengths of different materials.

6.2. Future Outlook

Advancing bottom-up synthesis techniques—such as molecular beam epitaxy (MBE) and atomic layer deposition (ALD)—coupled with interface engineering, will be essential to realize scalable, high-quality 2D photodetectors.

VII. CONCLUSION

The field of optoelectronics places considerable emphasis on the investigation of photodetectors, particularly those derived from TMDCs. While photovoltaics and light-emitting devices also receive attention, they are less prominent in comparison. As the demand for data-intensive models and connectivity grows, there is an increasing need for innovative approaches to implement additional features.

A critical factor influencing device performance is the fabrication of high-quality ohmic contacts to TMDCs, particularly for mono- to tri-layer flakes. Understanding the metal connections to TMDCs and minimizing resistance in these connections are essential for optimizing performance in optoelectronic and photonic devices. The unique material properties of TMDCs render them highly suitable for flexible electronic applications. Therefore, it is crucial to thoroughly investigate their interactions with flexible organic substrates and their compatibility with flexible device processing.

In terms of device design and future technology, it is important to prioritize straightforward operation over complex designs to meet performance objectives effectively. Additionally, secondary factors such as thermal losses, heat dissipation, external noise, and related aspects should be considered when analyzing device performance.

Bridging the gap between research and the development of commercial products utilizing TMDCs requires effective collaboration between academia and industry. Such partnerships will facilitate the translation of research findings into practical applications, driving innovation and progress in the field of TMDC-based devices.

Achieving scalable, high-quality synthesis and robust device integration are vital to elevate 2D materials from laboratory curiosities to practical photodetectors. Future research must prioritize reproducibility, stability, and interface control to unlock their full potential for applications spanning from flexible electronics to high-speed optical communications.

Acknowledgments

The authors wish to express their deepest appreciation to National institute of Laser Enhanced Sciences (NILES), Cairo University, and the American University in Cairo (AUC) for their exceptional support and encouragement throughout this research. The invaluable assistance provided by both institutions has been instrumental in the successful completion of this study, and their unwavering commitment to academic excellence has greatly inspired us.

Author contributions:

All authors contributed to the conception and design of the study. Material preparation and data collection were performed by Ahmed Abdelhady A. Khalil. Figures (1-4) were prepared by Heba A. Shawkey. All authors reviewed the manuscript. The first draft was written by Ahmed Abdelhady A. Khalil, Samar Akef, Heba A. Shawkey, and Mohamed A. Swillam, with all authors providing comments on previous versions. All authors read and approved the final manuscript. The revisions were made by Ahmed Abdelhady A. Khalil, Samar Akef, and Mohamed A. Swillam.

Funding and/or Competing interests:

The authors declare that no funds, grants, or other support were received during the preparation of this manuscript.
The authors have no competing interests to declare that are relevant to the content of this article.

Data Availability Statement:

Data Availability Statement: No Data associated in the manuscript.

REFERENCES

1. Novoselov, K. S., et al. Electric field effect in atomically thin carbon films. Science, (2004); 306(5696), 666–669.
2. Chhowalla, M., et al. The chemistry of two-dimensional layered transition metal dichalcogenide nanosheets. Nature Chemistry, (2013); 5(4), 263–275.
3. Akinwande, D., et al. A review on mechanics and mechanical properties of 2D materials—Graphene and beyond. Extreme Mechanics Letters, (2017); 13, 42–77.
4. Wang, Q. H., et al. Electronics and optoelectronics of two-dimensional transition metal dichalcogenides. Nature Nanotechnology, (2012); 7(11), 699–712.
5. Naguib, M., et al. Two-dimensional nanocrystals produced by exfoliation of Ti_3AlC_2. Advanced Materials, (2011); 23(37), 4248–4253.
6. Liu, H., et al. . Phosphorene: an unexplored 2D semiconductor with a high hole mobility. ACS Nano, (2014); 8(4), 4033–4041.
7. Vogt, P., et al. Silicene: Compelling experimental evidence for graphenelike two-dimensional silicon. Physical Review Letters, (2012); 108(15), 155501.

8. Lin, Z., et al. A scalable CVD approach for the synthesis of 2D materials. Nature Reviews Materials, (2021); 6(6), 391–411.
9. Ghosh, R., et al. Roll-to-roll production of large-area 2D materials: status and prospects. Advanced Materials, (2023); 35(20), 2207320.
10. Voiry, D., et al. Phase engineering of transition metal dichalcogenides. Chemical Society Reviews, (2015); 44(9), 2702–2712.
11. Dong, Y., et al. Surface functionalization of MXenes for tunable electrochemical properties. ACS Nano, (2022); 16(2), 2290–2304.
12. Zhang, Y., et al. Doping strategies in 2D materials for electronics and energy. Chemical Society Reviews, (2020); 49(21), 7339–7376.
13. Kang, K., et al. High-mobility three-atom-thick semiconducting films with wafer-scale homogeneity. Nature, (2015); 520(7549), 656–660.
14. Li, X., et al. . Integration of 2D materials into CMOS-compatible platforms. 3Nature Electronics, (2023); 6(3), 154–164.
15. Bonaccorso, F., et al. 2D materials: Getting ready for the market. Nature Nanotechnology, (2015); 10(9), 780–783.
16. Lee, Y., et al. . Industrial-scale challenges in 2D materials: From synthesis to system integration. Nature Materials, (2023); 22(2), 142–153.
17. Li, Y., et al. 2D materials in practical applications: a roadmap. Advanced Functional Materials, (2024); 34(5), 2309802.
18. Khalil Ahmed Abdelhady A., Karmalawi Abdallah M., Abdelmageed Alaaeldin A., et al. Thin-film photodiode based on novel SiC/MoS_2 composite by RF-sputtering for fast response photodetection. Optical Materials, (2024); 150 : 115168.
19. Khalil Ahmed Abdelhady A., Karmalawi Abdallah M., Abdelmageed Alaaeldin A., et al. Fast response fabricated MoS_2-photodiode based thin film. Journal of Materials Science: Materials in Electronics, (2024); 35, 8 : 546.
20. Khalil Ahmed Abdelhady A., Karmalawi Abdallah M., Abdelmageed Alaaeldin A., et al. Impact behavior of a novel GaN/MoS_2 composite photodiode based thin-film by RF-sputtering for fast response photodetection application. Optical and Quantum Electronics, (2024); 56, 5: 804.
21. Roberts, M. W., Clemons, C. B., Wilber, J. P., et al. Continuum Plate Theory and Atomistic Modeling to Find the Flexural Rigidity of a Graphene Sheet Interacting with a Substrate. J. Nanotechnol., (2010).
22. Berger, C., Song, Z., Li, T., et al. Ultrathin Epitaxial Graphite: 2DElectron Gas Properties and a Route toward Graphene-Based Nanoelectronics. J. Phys. Chem. B, (2004); 108 (52), 19912–19916.
23. Brida, D., Tomadin, A., Manzoni, C., et al. Ultrafast Collinear Scattering and Carrier Multiplication in Graphene. Nat. Commun. (2013); 4 (1), 1987–1989.
24. Wang, F., Zhang, Y., Tian, C., et al. Gate variable Optical Transitions in Graphene. Science, (2008); 320 (5873), 206–209.
25. Iqbal, M. A., Malik, M., Shahid, W., et al. . Materials for Photovoltaics: Overview, Generations, Recent Advancements and Future Prospects. Thin Films Photovoltaics, (2022); 5.
26. Nair, R. R., Blake, P., Grigorenko, A. N., et al. Fine Structure Constant Defines Visual Transparency of Graphene. Science, (2008); 320 (5881), 1308.
27. Manzeli, S., Ovchinnikov, D., Pasquier, D., et al. 2D Transition Metal Dichalcogenides. Nat. Rev. Mater., (2017); 2 (8), 1–5.
28. Malik, M., Iqbal, M. A., Choi, J. R, et al. 2D materials for efficient photodetection: Overview, mechanisms, performance and UV-IR range applications. Frontiers in Chemistry, (2022); 10 : 905404.
29. Ataca, C., Şahin, H., and Ciraci, S. Stable, Single-Layer MX_2 Transition-Metal Oxides and Dichalcogenides in a Honeycomb-like Structure. J. Phys. Chem. C, (2012); 116 (16), 8983–8999.
30. Svetin, D., Vaskivskyi, I., Sutar, P., et al. Transitions between Photoinduced Macroscopic Quantum States in 1T TaS_2 controlled by Substrate Strain. Appl. Phys. Express, (2014); 7 (10), 103201.
31. Shishidou, T., Freeman, A. J., and Asahi, R. Effect of GGA on the Half-Metallicity of the Itinerant ferromagnet CoS_2. Phys. Rev. B, (2001); 64 (18), 180401.
32. Xi, X., Wang, Z., Zhao, W., et al. Ising Pairing in Superconducting $NbSe_2$ Atomic Layers. Nat. Phys. (2016); 12 (2), 139–143.
33. Splendiani, A., Sun, L., Zhang, Y., et al. Emerging Photoluminescence in Monolayer MoS_2. Nano Lett., (2010);10 (4), 1271–1275.
34. Fei, F., Bo, X., Wang, R., et al. Nontrivial Berry Phase and Type-II Dirac Transport in the Layered Material $PdTe_2$. Phys. Rev. B, (2017); 96 (4), 041201.
35. Ye, L., Li, H., Chen, Z., et al. Near-Infrared Photodetector Based on MoS_2/Black Phosphorus Đ Heterojunction. Acs Photonics, (2016); 3 (4), 692–699.
36. Youngblood, N., Chen, C., Koester, S. J., et al. Waveguide-integrated Black Phosphorus Photodetector with High Responsivity and Low Dark Current. Nat. Phot., (2015); 9 (4), 247–252.
37. Zhang, G., Huang, S., Wang, F., et al. The Optical Conductivity of Few-Layer Black Phosphorus by Infrared Spectroscopy. Nat. Commun., (2020); 11 (1), 1847.
38. Qiao, J., Kong, X., Hu, Z. X., et al. High-mobility Transport Anisotropy and Linear Dichroism in Few-Layer Black Phosphorus. Nat. Commun. (2014); 5 (1), 4475–4477.
39. Liu, L., Sun, T., Ma, W. et al. Highly Responsive Broadband Black Phosphorus Photodetectors. China Opt. Express, (2018); 16 (2), 020002.
40. Ye, Y., Xiao, J., Wang, H., et al. Electrical Generation and Control of the Valley Carriers in a Monolayer Transition Metal Dichalcogenide. Nat. Nanotech, (2016); 11 (7), 598–602.
41. Shao, D. F., Lu, W. J., Lv, H. Y., et al. Electron-doped Phosphorene: a Potential Monolayer Superconductor. Europhysics Letters, (2014); 108, 67004.

42. Wang, X., and Lan, S. Optical Properties of Black Phosphorus. Adv. Opt. Phot. (2016); 8 (4), 618–655.
43. Britnell, L., Ribeiro, R. M., Eckmann, A., et al. Strong Light-Matter Interactions in Heterostructures of Atomically Thin Films. Science, (2013); 340 (6138), 1311–1314.
44. Zhang, S., Xie, M., Li, F., et al. Semiconducting Group 15 Monolayers: a Broad Range of Band Gaps and High Carrier Mobilities. Angew. Chem., (2016); 128 (5), 1698–1701.
45. Iqbal, M. A., Ashraf, N., Shahid, W., et al. Nanophotonics: Fundamentals, Challenges, Future Prospects and Applied Applications, (2021).
46. Ma, S., Zhou, P., Sun, L. Z., et al. Two-dimensional Tricycle Arsenene with a Direct Band Gap. Phys. Chem. Chem. Phys., (2016); 18 (12), 8723–8729.
47. Xie, M., Zhang, S., Cai, B., et al. A Promising Two-Dimensional Solar Cell Donor: Black Arsenic-Phosphorus Monolayer with 1.54 eV Direct Bandgap and Mobility Exceeding 14,000 $cm^2V^{-1}s^{-1}$. Nano Energy, (2016); 28, 433–439.
48. Vurgaftman, I., Meyer, J. R., and Ram-Mohan, L. R. Band Parameters for III-V Compound Semiconductors and Their Alloys. J. Appl. Phys., (2001); 89 (11), 5815–5875.
49. Chen, H., Galili, M., Verheyen, P., et al. 100-Gbps RZ Data Reception in 67-GHz Si-Contacted Germanium Waveguide Pin Photodetectors. J. Light. Technol., (2016); 35 (4), 722–726.
50. Staudinger, P. Crystal Phase Engineering in III-V Semiconductor Films: From Epitaxy to Devices. Lausanne: EPFL, (2020).
51. Li, N., Han, K., Spratt, W., et al. Ultra-low power Sub-photon-voltage High-Efficiency Light-Emitting Diodes. Nat. Photonics, (2019); 13 (9), 588–592.
52. Mueller, T., Xia, F., and Avouris, P. Graphene Photodetectors for High-Speed Optical Communications. Nat. Phot., (2010); 4 (5), 297–301.
53. Lou, Z., Liang, Z., and Shen, G. Photodetectors Based on Two Dimensional Materials. J. Semicond, (2016); 37 (9), 091001.
54. Fang, Z., Liu, Z., Wang, Y., et al. Graphene-antenna Sandwich Photodetector. Nano Lett., (2012);12 (7), 3808–3813.
55. Konstantatos, G., Badioli, M., Gaudreau, L., et al. Hybrid Graphene-Quantum Dot Phototransistors with Ultrahigh Gain. Nat. Nanotech, (2012); 7 (6), 363–368.
56. Sun, Z., Liu, Z., Li, J., et al. . Infrared Photodetectors Based on CVD-Grown Graphene and PbS Quantum Dots with Ultrahigh Responsivity. Adv. Mat., (2012); 24 (43), 5878–5883.
57. Gan, X., Shiue, R.-J., Gao, Y., et al. Chip integrated Ultrafast Graphene Photodetector with High Responsivity. Nat. Phot., (2013); 7 (11), 883–887.
58. Kim, K., Choi, J.-Y., Kim, T., et al. A Role for Graphene in Silicon-Based Semiconductor Devices. Nature, (2011); 479 (7373), 338–344.
59. Freitag, M., Low, T., Xia, F., et al. Photoconductivity of Biased Graphene. Nat. Phot. (2013); 7 (1), 53–59.
60. Yan, J., Kim, M.-H., Elle, J. A., et al. Dual-gated Bilayer Graphene Hot-Electron Bolometer. Nat. Nanotech, (2012); 7(7), 472–478.
61. Koppens, F. H. L., Mueller, T., Avouris, P., et al. Hybrid Graphene–Quantum Dot Phototransistors with Ultrahigh Gain. Nat. Nanotech., (2014); 7 (6), 363–368.
62. Liu, G., Ahsan, S., Khitun, A. G., et al. Graphene based Non-Boolean Logic Circuits. J. Appl. Phys., (2013); 114 (15), 154310.
63. Vora, H., Kumaravadivel, P., Nielsen, B., et al. Bolometric Response in Graphene Based Superconducting Tunnel Junctions. Appl. Phys. Lett., (2012); 100 (15), 153507.
64. Jeong, H., Song, J. H., Jeong, S., et al. Graphene/PbS Quantum Dot Hybrid Structure for Application in Near-Infrared Photodetectors. Sci. Rep., (2020); 10 (1), 12475–12477.
65. Splendiani, A., Sun, L., Zhang, Y., et al. Emerging Photoluminescence in Monolayer MoS_2. Nano Lett., (2010); 10 (4), 1271–1275.
66. George, A., Fistul, M. V., Gruenewald, M., et al. Giant Persistent Photoconductivity in Monolayer MoS_2 Field-Effect Transistors. npj 2D Mater. Appl., (2021); 5 (1), 1–8.
67. Ponomarev, E., Gutiérrez-Lezama, I., Ubrig, N., et al. Ambipolar Light-Emitting Transistors on Chemical Vapor Deposited Monolayer MoS_2. Nano Lett., (2015); 15 (12), 8289–8294.
68. Yin, Z., Li, H., Li, H., et al. Single-Layer MoS_2 Phototransistors. ACS Nano, (2012); 6 (1), 74–80.
69. Lopez-Sanchez, O., Lembke, D., Kayci, M., et al. Ultrasensitive Photodetectors Based on Monolayer MoS_2. Nat. Nanotech, (2013); 8 (7), 497–501.
70. Zhang, W., Chiu, M.-H., Chen, C.-H., et al. Role of Metal Contacts in High-Performance Phototransistors Based on WSe_2 Monolayers. ACS Nano, (2014); 8 (8), 8653–8661.
71. Abderrahmane, A., Ko, P. J., Thu, T. V., et al. High Photosensitivity Few-Layered $MoSe_2$ Back-Gated Field-Effect Phototransistors. Nanotechnology, (2014); 25 (36), 365202.
72. Lu, X., Utama, M. I. B., Lin, J., et al. Large-Area Synthesis of Monolayer and Few-Layer $MoSe_2$ Films on SiO_2 Substrates. Nano Lett., (2014); 14 (5), 2419–2425.
73. Wang, G., Zhang, Y., You, C., et al. Two Dimensional Materials Based Photodetectors. Infrared Phys. Technol. (2018); 88, 149–173.
74. Xia, F., Wang, H., and Jia, Y. Rediscovering Black Phosphorus as an Anisotropic Layered Material for Optoelectronics and Electronics. Nat. Commun., (2014); 5 (1), 4458–4466.
75. Zhang, W., Huang, J.-K., Chen, C.-H., et al. High-Gain Phototransistors Based on a CVD MoS_2 Monolayer. Adv. Mat., (2013); 25 (25), 3456–3461.
76. Jung, C., Kim, S.M., Moon, H., et al. Highly Crystalline CVD-Grown Multilayer $MoSe_2$ Thin Film Transistor for Fast Photodetector. Sci. Rep., (2015); 5 (1), 15313–15319.

77. Sik Hwang, W., Remskar, M., Yan, R., et al. Transistors with Chemically Synthesized Layered Semiconductor WS_2 Exhibiting 105 Room Temperature Modulation and Ambipolar Behavior. Appl. Phys. Lett., (2012); 101 (1), 013107.
78. Perea-López, N., Elías, A. L., Berkdemir, A., et al. Photosensor Device Based on Few-layered WS_2 Films. Adv. Funct. Mater., (2013); 23 (44), 5511–5517.
79. Zhang, Y., Chang, T.-R., Zhou, B., et al. Direct Observation of the Transition from Indirect to Direct Bandgap in Atomically Thin Epitaxial $MoSe_2$. Nat. Nanotech, (2014); 9 (2), 111–115.
80. Lin, Y.-F., Xu, Y., Wang, S.-T., et al. Ambipolar $MoTe_2$ Transistors and Their Applications in Logic Circuits. Adv. Mat., (2014); 26 (20), 3263–3269.
81. Wilson, J. A., and Yoffe, A. D. The Transition Metal Dichalcogenides Discussion and Interpretation of the Observed Optical, Electrical and Structural Properties. Adv. Phys., (1969); 18 (73), 193–335.
82. Yang, S., Tongay, S., Li, Y., et al. Layer dependent Electrical and Optoelectronic Responses of $ReSe_2$ Nanosheet Transistors. Nanoscale, (2014); 6 (13), 7226–7231.
83. Jo, S.-H., Park, H.-Y., Kang, D.-H., et al. Broad Detection Range Rhenium Diselenide Photodetector Enhanced by (3-Aminopropyl) Triethoxysilane and Triphenylphosphine Treatment. Adv. Mat., (2016); 28 (31), 6711–6718.
84. Ahn, J., Ko, K., Kyhm, J.-h., et al. Near-Infrared Self-Powered Linearly Polarized Photodetection and Digital Incoherent Holography Using $WSe_2/ReSe_2$ van der Waals Heterostructure. ACS Nano, (2021); 15 (11), 17917–17925.
85. Liu, F., Zheng, S., He, X., et al. Highly Sensitive Detection of Polarized Light Using Anisotropic 2D ReS_2. Adv. Funct. Mat., (2016); 26 (8), 1169–1177.
86. Li, J., Han, J., Li, H., et al. Large-area, Flexible Broadband Photodetector Based on WS_2 Nanosheets Films. Mater. Sci. Semicond. Process., (2020); 107, 104804.
87. Pham, P. V., Bodepudi, S. C., Shehzad, K., et al. 2D Heterostructures for Ubiquitous Electronics and Optoelectronics: Principles, Opportunities, and Challenges. Chem. Rev., (2022).
88. Chen, J. J., Wang, Q., Meng, J., et al. Photovoltaic Effect and Evidence of Carrier Multiplication in Graphene Vertical Homojunctions with Asymmetrical Metal Contacts. ACS Nano., (2015); 9 (9), 8851–8858.
89. Mukherjee, S., Maiti, R., Midya, A., et al. Tunable Direct Bandgap Optical Transitions in MoS_2 Nanocrystals for Photonic Devices. Acs Photonics, (2015); 2 (6), 760–768.
90. Zhang, K., Zhang, T., Cheng, G., et al. Interlayer Transition and Infrared Photodetection in Atomically Thin Type-II $MoTe_2$/ MoS_2 van der Waals Heterostructures, ACS Nano, (2016); 10 (3), 3852–3858.
91. Radisavljevic, B., Whitwick, M. B., and Kis, A. Integrated Circuits and Logic Operations Based on Single-Layer MoS_2. ACS Nano, (2011); 5 (12), 9934–9938.
92. Elahi, E., Nisar, S., Rabeel, M., et al. Gate-controlled rectification and broadband photodetection in a P–N diode based on TMDC heterostructures. Mater. Adv., (2024); 5(3), 1226–1233.
93. Janardhanam, V., Zummukhozol, M., Jyothi, I., et al. Self-powered MoS_2/n-type GaN heterojunction photodetector with broad spectral response in ultraviolet–visible–near-infrared range. Sensors & Actuators: A. Physical, (2023); 360, 114534.